Neutrino Interactions with Supernova Matter

Wechselwirkung von Neutrinos mit Supernova-Materie
Zur Erlangung des Grades eines Doktors der Naturwissenschaften (Dr. rer. nat.)
genehmigte Dissertation von M. Sc. Alexander Bartl, geb. in Offenbach am Main
Tag der Einreichung: 12. Juli 2016, Tag der Prüfung: 17. Oktober 2016
Darmstadt 2016 — D 17

1. Gutachten: Prof. Ph. D. Achim Schwenk
2. Gutachten: Prof. Dr. Almudena Arcones Segovia

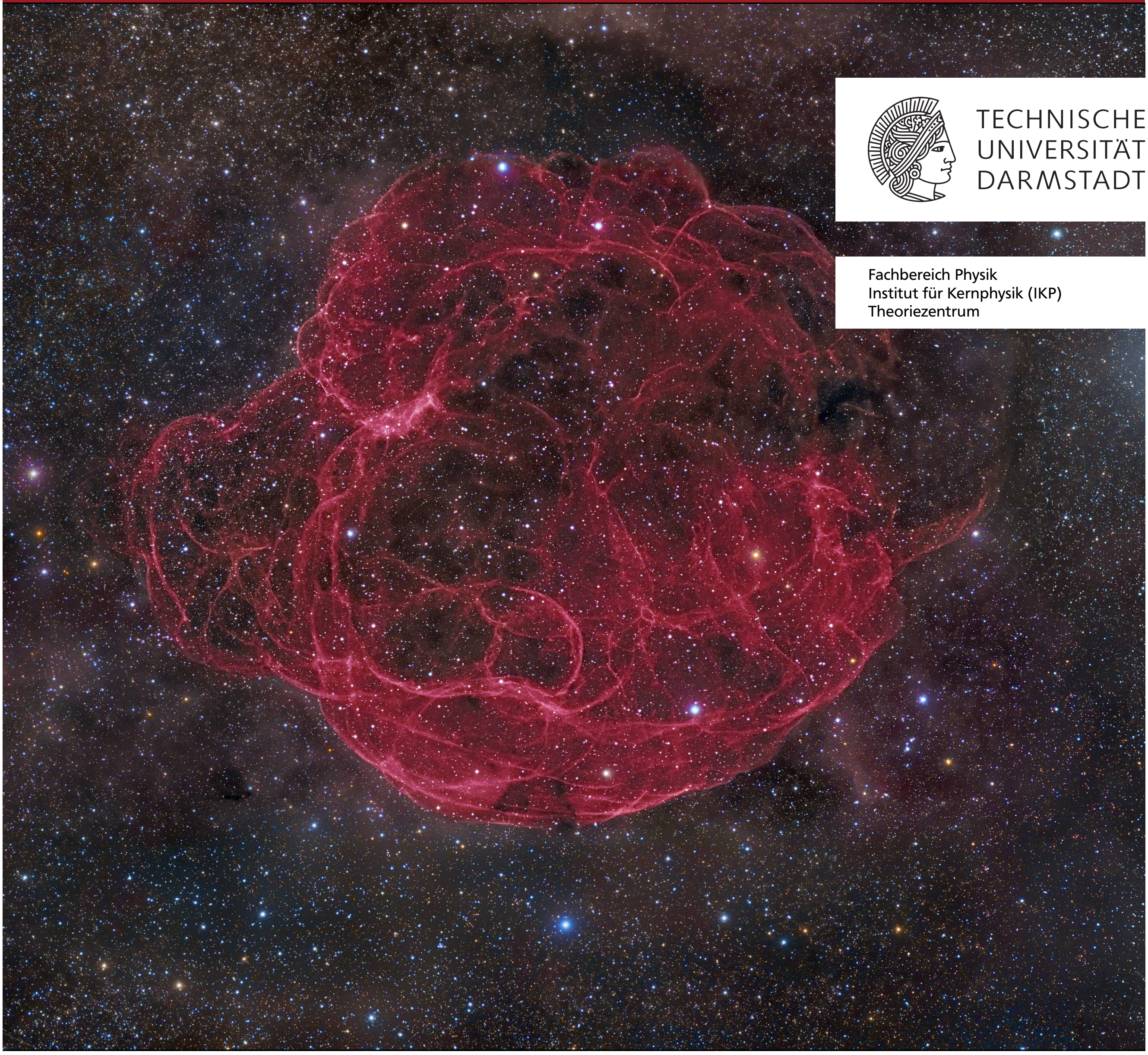

TECHNISCHE
UNIVERSITÄT
DARMSTADT

Fachbereich Physik
Institut für Kernphysik (IKP)
Theoriezentrum

Neutrino Interactions with Supernova Matter
Wechselwirkung von Neutrinos mit Supernova-Materie

Genehmigte Dissertation von M. Sc. Alexander Bartl, geb. in Offenbach am Main

1. Gutachten: Prof. Ph. D. Achim Schwenk
2. Gutachten: Prof. Dr. Almudena Arcones Segovia

Tag der Einreichung: 12. Juli 2016
Tag der Prüfung: 17. Oktober 2016

Darmstadt 2016 — D 17

Bitte zitieren Sie dieses Dokument als:
URN: urn:nbn:de:tuda-tuprints-57138
URL: http://tuprints.ulb.tu-darmstadt.de/5713

Abstract

Massive stars end their life in an energetic explosion called a core-collapse supernova. In such a supernova, neutrinos are produced in copious number and their interactions with matter play a major role for the supernova dynamics, the observable neutrino signal, and the conditions for nucleosynthesis. In supernova simulations, neutrino reactions involving interacting nucleons (like bremsstrahlung, inelastic scattering, and the modified Urca process) are typically described by simple models, including the one-pion-exchange (OPE) approximation for nucleon-nucleon interactions, or not implemented in the case of inelastic scattering.

In this thesis, we extend the formalism to go beyond these approximations. We derive expressions for the structure factor considering neutral-current reactions in non-degenerate mixtures of neutrons and protons, an expression that combines the effect of nucleon-nucleon interactions and nuclear recoil in non-degenerate pure neutron matter, and a structure factor for charged-current processes involving interacting nucleons. In mixtures of neutrons and protons, our calculations based on chiral effective field theory (EFT) interactions show a reduction of neutrino interaction rates by a factor of two compared to the OPE approximation at typical neutrinosphere densities (10^{12}–$10^{13}\,\mathrm{g\,cm^{-3}}$) and beyond. This agrees with earlier work in pure neutron matter. Calculations beyond the Born approximation based on phase shifts extracted from experiment show a similar reduction at these densities, but a large enhancement at lower densities, especially for small energy transfer. We trace this effect to the large scattering lengths in the two-nucleon sector and the fact that supernova matter at subnuclear densities behaves similar to a resonant Fermi gas. In collaboration with astrophysicists, we have investigated the impact of our improved rates on the neutrino signal and the supernova dynamics using two different approaches: detailed rates to post-process profiles obtained in simulations as well as a simple approximation of our results that is directly implemented in a simulation. We find minor changes in the neutrino emission with a shift of luminosities from heavy-lepton to electron neutrinos, harder neutrino spectra, and somewhat delayed cooling of the proto-neutron star.

Three-body forces occur naturally in the framework of chiral EFT and were shown to be important in nuclear structure calculations. We present first results for neutrino rates in non-degenerate matter that include three-body interactions. In pure neutron matter, we find a significant increase of the rates and opacities compared to the chiral results only including two-body forces, both at next-to–next-to–leading order and (to a lesser extent) at next-to–next-to–next-to–leading order. Our results show smaller effects in mixtures. In addition, we look at scattering reactions, where the long-wavelength limit of the structure factor is found to work well when calculating opacities, but not the energy transfer. Compared to nuclear recoil, interactions have a significant impact on the energy transfer especially for low-energy neutrinos in high-density, high-temperature environments. Our first results for the charged-current spin relaxation rate show trends similar to the neutral-current case. Finally, we outline open questions and remaining steps towards a consistent description of neutrino-nucleon interactions based on modern nuclear forces.

Cover picture: Supernova remnant Simeis 147, composite of LRGB data and narrowband hydrogen-alpha data (red). The remnant is estimated to be 3 000 light-years away and 150 light-years in diameter. Light from the corresponding supernova reached Earth around 40 000 years ago [1, 2].

Zusammenfassung

Kernkollaps-Supernovae sind energetische Explosionen, die das Ende massereicher Sterne markieren und in deren Verlauf eine Vielzahl von Neutrinos erzeugt wird. Die Wechselwirkung von Neutrinos mit der umgebenden Materie spielt eine wichtige Rolle für die Dynamik der Supernova, das messbare Neutrinosignal und die Nukleosynthese-Prozesse. Für einige Wechselwirkungsprozesse, beispielsweise Bremsstrahlung, inelastische Streuung und den modifizierten Urca-Prozess, sind miteinander wechselwirkende Nukleonen besonders wichtig. In Supernova-Simulationen werden diese Prozesse basierend auf vereinfachten Modellen wie der Ein-Pion-Austausch-Näherung für die Nukleon-Nukleon-Wechselwirkung beschrieben oder im Fall der inelastischen Streuung gar nicht berücksichtigt.

In dieser Arbeit erweitern wir den bestehenden Formalismus und gehen über diese Näherungen hinaus. Wir berechnen Ausdrücke für die Strukturfunktion für Neutrino-Wechselwirkungsprozesse mit neutralen Strömen, die im Fall nicht-entarteter Mischungen aus Protonen und Neutronen gültig sind bzw. in Neutronenmaterie die Effekte von Nukleon-Nukleon-Wechselwirkungen und Rückstoß kombinieren. Darüber hinaus leiten wir einen Ausdruck für die Strukturfunktion für Prozesse mit geladenen Strömen her, an denen miteinander wechselwirkende Nukleonen beteiligt sind. Unsere Rechnungen basierend auf Wechselwirkungen, die durch die chirale effektive Feldtheorie (EFT) beschrieben werden, zeigen in Mischungen aus Protonen und Neutronen eine Halbierung der Neutrino-Wechselwirkungsraten verglichen mit Rechnungen in der Ein-Pion-Austausch-Näherung für Dichten, die für die Neutrinosphären typisch sind ($10^{12} - 10^{13}\,\mathrm{g\,cm^{-3}}$), sowie bei höheren Dichten. Dies stimmt mit früheren Ergebnissen in Neutronenmaterie überein. Rechnungen basierend auf Streuphasen, die aus experimentellen Daten extrahiert wurden, gehen über die Born-Näherung hinaus und zeigen eine ähnliche Reduktion bei hohen Dichten, aber eine deutliche Steigerung bei niedrigen Dichten, insbesondere für kleine Energieüberträge. Wir führen diesen Effekt darauf zurück, dass die Streulängen im Zwei-Nukleon-Sektor groß sind und sich Supernova-Materie bei kleinen Dichten wie ein resonantes Fermi-Gas verhält. Der Einfluss unserer verbesserten Raten auf die Neutrino-Emission und die Dynamik von Supernovae werden in Zusammenarbeit mit Astrophysikern auf zwei Arten untersucht: Wir verwenden detaillierte Tabellen unserer Ergebnisse, um nachträglich die Neutrinoraten entlang von in Supernova-Simulationen generierten Profilen zu berechnen, sowie einen ungefähren Korrekturfaktor, der direkt in einer Simulation implementiert wird. Wir finden geringe Änderungen der Neutrino-Emission in Form einer Verschiebung der Luminosität von Myon- und Tau- zu Elektron-Neutrinos und härterer Neutrinospektren sowie eine leichte Verzögerung der Proto-Neutronenstern-Abkühlung.

Die chirale EFT sagt auch Dreiteilchenkräfte voraus, deren Bedeutung in Kernstruktur-Rechnungen gezeigt wurde. Wir präsentieren erstmals Ergebnisse für Neutrino-Wechselwirkungsraten mit Dreiteilchenkräften in nicht-entarteter Materie. In Neutronenmaterie finden wir sowohl in dritter als auch (in geringerem Maße) in vierter Ordnung der chiralen Entwicklung eine starke Zunahme der Wechselwirkungsraten und Opazitäten relativ zu Rechnungen, die nur chirale Zweiteilchenkräfte enthalten. Der Einfluss von Dreiteilchenkräften in Mischungen aus Protonen und Neutronen ist hingegen deutlich geringer. Zusätzlich betrachten wir inelastische Streuung und zeigen, dass der Grenzfall großer Wellenlängen für die Strukturfunktion zwar für die Berechnung von Opazitäten, aber nicht für die des Energieübertrags eine gute Näherung darstellt. Nukleon-Nukleon-Wechselwirkungen spielen verglichen zum Energieübertrag durch Rückstoß vor allem eine Rolle für Neutrinos mit niedriger Energie in dichten, heißen Umgebungen. Unsere ersten Ergebnisse für die Spin-Relaxationsrate in Prozessen mit geladenen Strömen zeigen Trends, die denen für Prozesse mit neutralen Strömen ähnlich sind. Abschließend skizzieren wir offene Fragen und verbleibende Schritte hin zu einer konsistenten Beschreibung von Neutrino-Nukleon-Wechselwirkungen basierend auf modernen Kernkräften.

Contents

1 Introduction and Motivation

Once a massive star runs out of fuel and reaches the end of its lifetime, it turns into an enormous explosion, a so-called core-collapse supernova. Over the course of a few minutes this explosion releases more energy than our sun emits over its whole lifetime of 10 billion years. After burning hydrogen for millions of years, collapse and explosion happen on a sub-second timescale. With temperatures reaching several hundred billion Kelvin and densities beyond nuclear saturation density, supernovae are truly extreme events. They therefore provide a unique "laboratory" for matter under extreme conditions as we cannot reproduce these conditions on Earth.

Being such energetic explosions, nearby supernovae are visible to the naked eye. There is evidence for Chinese sightings of supernovae as far back as 185 CE and there might be accounts of even earlier records in indigenous traditions [3]. The supernova recorded in 1006 in various countries was the brightest ever recorded, multiple times as bright as Venus [4]. In 1054, another supernova was visible on Earth. It was recorded by Chinese, Japanese and Arab astronomers and its remnant is now known as the Crab Nebula (Fig. 1.1 a). Both Tycho Brahe (in 1572) and Johannes Kepler (in 1604) observed and described supernovae. The closest observed supernova since then was SN 1987A (Fig. 1.1 b,c) in the nearby Large Magellanic Cloud.

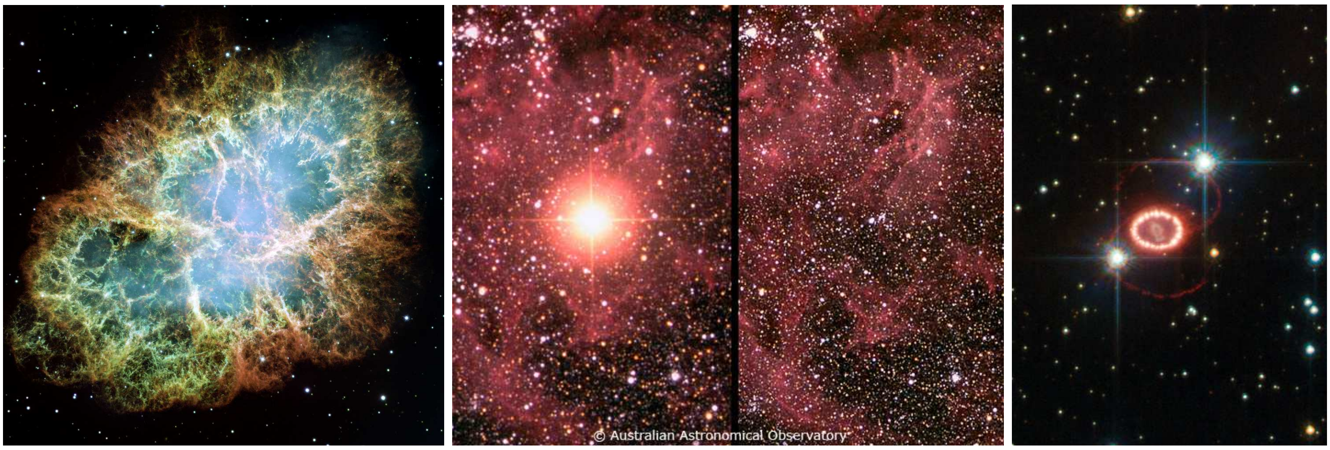

(a) Crab Nebula [5] (b) After (left) and before (right) SN1987A [6] (c) SN 1987A remnant [7]

Figure 1.1: The remnant of a supernova observed in 1054, also known as Crab Nebula, the nearby supernova SN 1987A in the Large Magellanic Cloud before and after the explosion and its remnant as seen by the Hubble Space Telescope in 2011.

Supernovae are also an important nucleosynthesis site: During the explosion, heavy elements are created and subsequently thrown into space. Over several generations of supernovae, the interstellar medium is enriched with these elements, forming the ingredients necessary for rock planets like our Earth and the building blocks of life. Hence, supernovae are one piece of the puzzle of "Where do we come from?".

Because of all of that, we would like to understand the supernova mechanism. Since experiments in the lab are unfeasible, we are limited to observations and simulations. Unfortunately, supernovae are rather rare. While we observe hundreds per year, almost all of them are too far away for detailed measurements. We could learn a lot more from a galactic supernova, but none was observed since the one seen by Kepler. In addition, these are complex systems that will not be understood from observation alone. As the laws of physics are universal, we can combine our best theoretical models (that have been tested against experiment where possible) into numerical simulations. Currently, these simulations do not match the observations. They are limited by computational resources and the quality of theory input.

Neutrinos are a different kind of extreme: They are elementary particles with less than a millionth of the mass of an electron that travel at nearly the speed of light. Here on Earth, about 100 billion neutrinos pass through

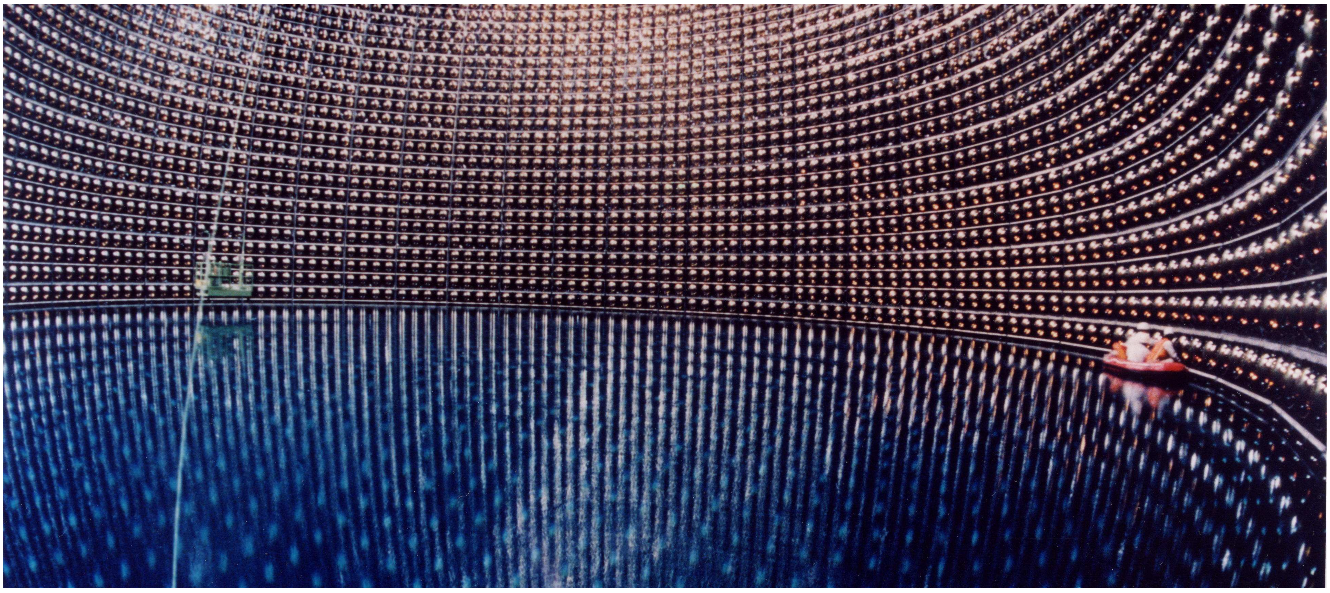

Figure 1.2: Super-Kamiokande neutrino detector in 1996, only partially filled with water. Note the rubber boat for scale [8].

an area the size of a fingernail – every second. Yet they interact so weakly, we do not notice them. About once in a person's lifetime, a neutrino will interact with an atom in their body [9]. Therefore, we have to build huge detectors: Super-Kamiokande (Fig. 1.2) holds 50 000 tons of ultrapure water, is equipped with more than 11 000 photo detectors and was built 1 000 meters below the surface to shield it from background radiation. It sees about one neutrino every hour [10].

In core-collapse supernovae, matter is much denser than in our bodies or detectors and the number of neutrinos emitted is comparable to the number of atoms in the sun. Hence, neutrino-matter interactions happen frequently. As neutrinos carry away 99 % of the energy, these interactions are crucial to the supernova dynamics (see Section 2.1) and therefore need to be taken into account in supernova simulations. Neutrino interactions

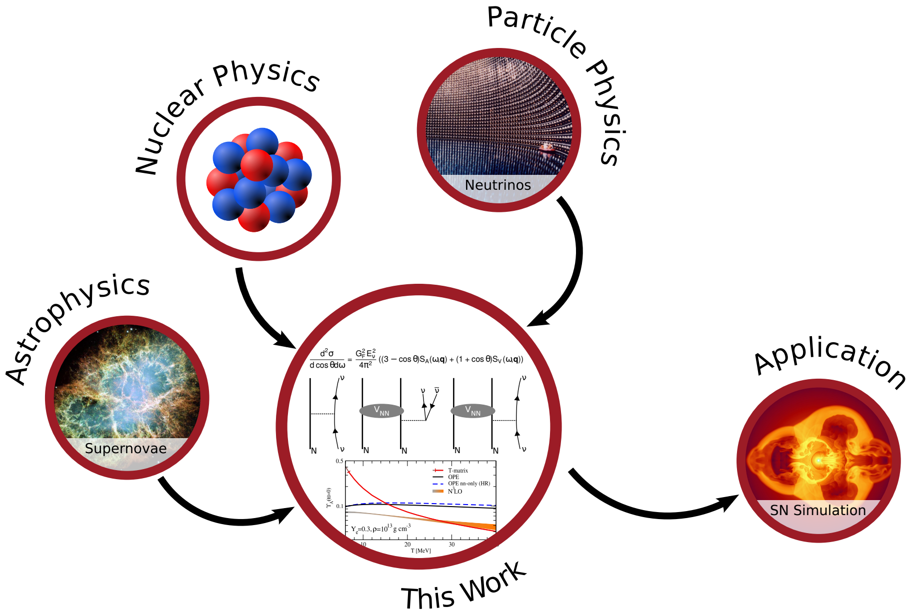

Figure 1.3: This work is located at the intersection of nuclear, particle and astrophysics. The results are applied in supernova simulations, with the goal to improve on older, more simplified descriptions of neutrino-nucleon interactions.

with interacting nucleons are currently only included based on a very simplistic nuclear interaction, one-pion exchange. In this thesis, we expand the formalism to go beyond this approximation, use modern nuclear forces to calculate updated interaction rates and evaluate their impact on supernova simulations.

Since this work is located at the intersection of nuclear physics, particle physics, and astrophysics (Fig. 1.3), the first chapters are meant as an introduction, providing an overview of the physics connected to or surrounding the subject of this thesis on a fairly introductory level. In Chapter 2, properties of supernovae and the role of neutrino interactions are discussed. Chapter 3 gives an introduction to quantum chromodynamics (QCD), chiral effective field theory, and the T-matrix formalism, which are the basis for nuclear interactions used in this work.

We derive a structure factor expression for neutral-current neutrino interactions in mixtures of protons and neutrons in Chapter 4 and present results for the interaction rates and absorption opacities, including first results with three-body forces. The impact of these calculations on supernovae are explored in Chapter 5. In Chapter 6, we focus on scattering reactions, derive a structure factor expression that combines recoil and nucleon-nucleon interactions, and show results for opacities and the energy transfer per collision. Charged-current reactions are discussed in Chapter 7. Finally, we summarize our results in Chapter 8 and give an overview of open questions. Implementation details are provided in Appendix A.

Throughout this thesis, natural units are used, i. e., $\hbar = c = k_B = 1$. For calculations of rates, we take the neutron and proton masses to be equal, and neglect effective mass effects for these first calculations.

2 Core-Collapse Supernovae and Neutrino Interactions

Supernovae are powerful and luminous astrophysical events marking the end of certain types of stars. Two main types have to be distinguished: Thermonuclear supernovae (called "Type Ia" for historical reasons) happen when white dwarfs gain mass and reach an upper limit, the so-called Chandrasekhar mass.

In this thesis, we concentrate on the other type, core-collapse supernovae (CCSN). They are about three times as frequent as thermonuclear supernovae [11] and powered by the release of gravitational energy rather than nuclear fusion. In our galaxy, two to three supernovae are expected every century. In the whole universe, the supernova rate is estimated to be about five per second [11]. From observations it is estimated that the explosion energy, i. e., kinetic and electromagnetic energy, is in the order of $10^{51}\,\mathrm{erg}\big(=10^{44}\,\mathrm{J}=1\,\mathrm{B}$ (Bethe) $=1\,\mathrm{foe}$ (ten to the fifty-one erg)$\big)$, with hundred times that energy carried away in neutrinos. Observations also show asymmetric remnants and neutron stars with large velocities, implying that explosions tend to be asymmetrical.

2.1 Explosion Mechanism and the Role of Neutrinos

In massive stars, nuclear fusion creates an onion-like structure of burning layers with an iron core that is initially stabilized against gravity mostly by electron degeneracy pressure. However, electrons are captured either on protons or ions, converting protons to neutrons while producing neutrinos that escape the system, carrying away energy and inhibiting the reverse reaction. In addition to this deleptonization, in the shell around the iron core, silicon is still converted to iron, increasing the mass of the core and bringing it closer to the so-called Chandrasekhar limit. Neglecting rotation and temperature effects, a core with equal number of protons and neutrons is stable up to a mass of $M_{Ch}=1.457\,M_\odot$, where $M_\odot$ is the mass of our sun.

The effective Chandrasekhar mass depends on the electron fraction and entropy profiles [12] and is proportional to Y_e^2, where Y_e is the ratio of electrons to baryons. In a medium of protons, neutrons, and electrons, the electron fraction is given by $Y_e=n_p/(n_n+n_p)$ due to charge neutrality, with neutron and proton densities $n_{n,p}$. Electron captures reduce Y_e. Eventually the core will be too massive to support its own weight against gravitational collapse. Within less than a second, the 1000 km-radius core collapses to an object with a radius of a few ten kilometers. At that point, the density is higher than inside a nucleus. The repulsive short-distance interaction between nucleons dominates and prevents the core from further collapse.

Infalling material bounces off the now-stiff core and launches a shock wave that propagates outwards, while more and more material falls in (Figure 2.1). Initially, it was thought that this shock wave would disrupt the star and lead to the explosion. Further analysis, however, showed that while the shock travels through the outer core, it dissociates the iron and nickel, losing its energy. In addition, electron capture on protons produces neutrinos that are trapped but escape once the shock reaches lower-density regions, carrying away energy. Eventually, a standing shock at about $100-200\,\mathrm{km}$ radius is formed [12].

Colgate and White [14] were the first to suggest that most of the released binding energy is carried away in the form of neutrinos and this provides an energy source for the explosion if some of the about 10^{58} neutrinos [15] are absorbed on their way out. In 1985, Bethe and Wilson [16] formulated the so-called delayed neutrino-heating mechanism: Behind the shock, a region develops where neutrino absorption dominates over emission. This net neutrino heating in the so-called gain region increases the entropy behind the shock and thus revives it. The gain radius, i. e., the border between the cooling and heating region, can be estimated from the dominant charged-current neutrino reactions, $p+e^-\longleftrightarrow n+\nu_e$ and $n+e^+\longleftrightarrow p+\overline{\nu}_e$ (cf. Section 2.2). The neutrino absorption scales with the neutrino energy E_ν like E_ν^2 while the emission rate is proportional to T^6, where T is the temperature, producing an interface where both rates are equal [17].

The amount of heating depends on the time material spends in the gain region. If the material further in is heated more, it expands and becomes lighter than the material on top of it, leading to a Rayleigh-Taylor instability

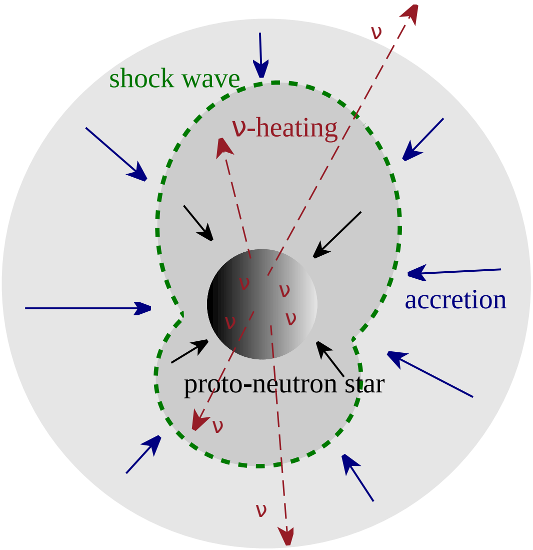

Figure 2.1: The situation after core-bounce: The collapsed core (black) formed a proto-neutron star, the shock wave (green) has encountered incoming material (blue), lost its energy through dissociation and has stalled. Material keeps falling in. Inside the proto-neutron star, neutrinos (red) are produced that can escape from the outer parts. While most neutrinos escape the system, some are absorbed in the gain region, depositing energy behind the shock and thus reviving the explosion. Not shown is the gain radius somewhere inside the shock wave. From [13], colored.

and thus turbulence. This neutrino-driven convection, visible as high-entropy plumes and low-entropy downflows (cf. Fig. 2.6), increases the gain region and leads to longer heating timescales and hence enhanced heating efficiency [11, 17]. Turbulences can also provide additional outward radial pressure on the shock [18]. One particular source of turbulence is the standing accretion shock instability (SASI) [19, 20], an instability of the shock wave itself.

Most one-dimensional (i. e., spherically symmetric) simulations with state-of-the-art neutrino treatment fail to explode [21]. In spherically symmetric models, the inflow of matter cannot continue once the explosion sets off. In addition, multi-dimensional effects such as turbulence and buoyancy are neglected. In two- and three-dimensional simulations which include these effects, the delayed neutrino-heating mechanism is able to explode massive stars and is currently the most likely mechanism for normal core-collapse supernovae [17, 18, 22]. Nevertheless, as state-of-the-art simulations tend to underpredict the explosion energy (see Section 2.5), alternative mechanisms are called for by members of the community, e. g., in Ref. [23]. Candidates include mechanisms based on rapid rotation and strong magnetic fields, phase transitions, jets, and acoustic oscillations [17].

The collapsed core forms a so-called proto-neutron star, a very hot and dense object that stays gravitationally bound. For the first few seconds, this object will cool via neutrino emission. Afterwards, it will continue to cool down by emitting electromagnetic radiation, forming a neutron star. The formation of a black hole is also possible, either directly or delayed [24]. If the shock cannot be revived by neutrinos, no explosion happens and a black hole is formed instead (failed supernova). Alternatively, after the proto-neutron star forms, some of the material that was accelerated away by the blast might still be gravitationally bound. It will eventually fall back on the neutron star which might in turn exceed its maximum mass and collapse to a black hole.

2.2 Neutrino Reactions

As discussed in the previous section, neutrino reactions play a key role in supernovae. In this section, we provide an overview of relevant reactions.

The most frequent reactions are scattering reactions which can happen on all weakly interacting particles: nucleons (N), electrons and positrons ($e^{\mp}$), ions ((A,Z)), and other neutrinos (ν):

$$N + \nu \longleftrightarrow N + \nu\,, \tag{2.1}$$

$$e^{\pm} + \nu \longleftrightarrow e^{\pm} + \nu \,, \tag{2.2}$$
$$(A,Z) + \nu \longleftrightarrow (A,Z) + \nu \,, \text{ and} \tag{2.3}$$
$$\nu + \nu \longleftrightarrow \nu + \nu \,. \tag{2.4}$$

These processes are therefore the main contribution to the neutrino opacity, i. e., the energy-averaged inverse mean-free path, preventing neutrinos from free-streaming above certain matter densities. All these reactions also happen with antineutrinos. While they do not change the number of neutrinos, they can affect their energies, especially when the scattering partner is light ($e^{\pm}$, ν). When scattering on nucleons or ions, some momentum can be transferred via recoil, but this effect is small at low neutrino energies, see Section 6.4.

Electron (anti)neutrinos are created when protons (neutrons) are converted to neutrons (protons):

$$p + e^{-} \longleftrightarrow n + \nu_e \,, \tag{2.5}$$
$$n + e^{+} \longleftrightarrow p + \overline{\nu}_e \,. \tag{2.6}$$

This reaction is not limited to free neutrons and protons, it can also happen inside a nucleus. In the forward direction, it is known as electron (positron) capture. The reverse reaction is an important source for neutrino absorption. Note that only electron (anti)neutrinos are typically considered in this process. To capture a muon or tau neutrino according to the backwards reaction of (2.5), a muon (or tau) would have to be created. The muon is more than 200 times as heavy as the electron. Hence, the threshold neutrino energy for this process is much higher than for the electron neutrino. The tau is even heavier. Nevertheless, muonic charged-current reactions might play an interesting role [25].

A more common way to create or absorb muon or tau (anti)neutrinos are pair processes. Electron-positron pairs can be converted to neutrino pairs of all flavors:

$$e^{-} + e^{+} \longleftrightarrow \nu + \overline{\nu} \,. \tag{2.7}$$

Neutrinos can also change flavor that way by annihilating one pair and creating another,

$$\nu_e + \overline{\nu}_e \longleftrightarrow \nu_x + \overline{\nu}_x \,. \tag{2.8}$$

Furthermore, neutrino pairs are created in hadronic bremsstrahlung processes:

$$N + N \longleftrightarrow N + N + \nu + \overline{\nu} \,, \tag{2.9}$$
$$n + \alpha \longleftrightarrow n + \alpha + \nu + \overline{\nu} \,. \tag{2.10}$$

The reverse reactions are called pair absorption. The first process will be discussed in details in the following subsection and in Chapter 4. The second process is discussed in Ref. [26].

For the hadronic processes, it is obvious that the strong interaction between the nucleons plays a role. The strong interaction is also important for the processes (2.3), (2.5), and (2.6). Especially for the charged-current processes in (2.5) and (2.6), the effect of surrounding nuclei can be included in a mean-field formalism [27–31].

There are, however, modified processes that directly involve multiple nucleons, namely inelastic scattering on interacting nucleons,

$$N + N + \nu \longleftrightarrow N + N + \nu \,, \tag{2.11}$$

which will be discussed in the next subsection and Chapter 6, as well as

$$N + p + e^{-} \longleftrightarrow N + n + \nu_e \quad \text{and} \tag{2.12}$$
$$N + n + e^{+} \longleftrightarrow N + p + \overline{\nu}_e \,. \tag{2.13}$$

These will be the subject of Chapter 7. A different process, not discussed in this thesis, is nuclear deexcitation by neutrino pair emission,

$$(A,Z)^{*} \rightarrow (A,Z) + \nu + \overline{\nu} \,, \tag{2.14}$$

which is a major contribution for electron antineutrinos and heavy-flavor neutrinos and antineutrinos during the collapse phase [32–34].

Reactions closely related to Eqs. (2.5), (2.6), (2.12) and (2.13) are central for neutron star cooling via the direct (modified) Urca process:

$$(N+)\,n \rightarrow (N+)\,p + e^- + \overline{\nu}_e \;, \tag{2.15}$$

$$(N+)\,p + e^- \rightarrow (N+)\,n + \nu_e \;. \tag{2.16}$$

When both interactions happen in sequence, the net result is the emission of a neutrino pair which, at sufficiently low densities, can leave the system and carry away energy. The direct process has a much higher rate while the additional nucleons in the modified Urca reactions allow this process to work under conditions where the direct Urca process is kinematically forbidden.

In addition to flavor changes via the MSW effect [35,36] and reaction (2.8), collective oscillations were found that completely swap neutrino flavors above a certain split energy [37,38]. Neutrino flavor evolution can become even more involved by effects caused by the few neutrinos scattering beyond the neutrinosphere [39,40]. Depending on when and where these oscillations happen, they can impact the observed neutrino signal, supernova dynamics and the nucleosynthesis. In recent studies, however, collective effects appear suppressed during the accretion phase [41].

A complete set of weak interactions based on realistic descriptions was found to be important for supernova dynamics [42]. State-of-the-art simulations (e. g., those in Refs. [43–45]) typically include reactions up to Eq. (2.9), some excluding reaction (2.8). All reactions mentioned below that are not included yet.

It is useful to talk about neutrino reactions in terms of a structure factor. We introduce this quantity for the neutral-current reactions involving nucleons, namely (2.1), (2.9), and (2.11), shown diagrammatically in Figure 2.2.

2.2.1 Neutral-Current Structure Factor

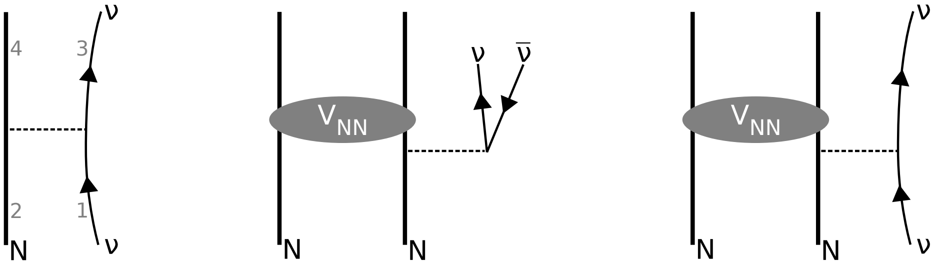

Figure 2.2: Elastic scattering on nucleons, neutrino bremsstrahlung and inelastic scattering (based on Ref. [46]).

The neutral-current weak-interaction Lagrangian for low-energy probes is given by (see, e. g., Ref. [47])

$$\mathcal{L}_{nc} = \frac{G_\mathrm{F}}{\sqrt{2}} l_\mu j^\mu = \frac{G_\mathrm{F}}{\sqrt{2}} \overline{\psi}_\nu \gamma_\mu (1-\gamma_5)\, \psi_\nu \overline{\psi}_N \gamma_\mu (C_V - C_A \gamma_5)\, \psi_N \;, \tag{2.17}$$

where G_F is the Fermi coupling constant, l_μ is the leptonic and j_μ the hadronic weak neutral current, γ_μ are Dirac matrices, ψ_ν neutrino fields, ψ_N nucleon Dirac fields, and C_A and C_V the axial and vector weak charges. For neutrons, $C_A^n = -g_A/2$ and $C_V^n = -1/2$, while for protons, $C_A^p = g_A/2$ and $C_V^p = 1/2 - 2\sin^2\theta_W \approx 0$ with Weinberg angle θ_W.

From Fermi's golden rule, the cross section for neutrino-nucleon scattering per unit volume is given by [48]

$$\frac{\sigma}{V} = 2 \int \frac{\mathrm{d}^3 p_2}{(2\pi)^3} \int \frac{\mathrm{d}^3 p_3}{(2\pi)^3} \int \frac{\mathrm{d}^3 p_4}{(2\pi)^3} (2\pi)^4\, \delta^{(4)}(P_1 + P_2 - P_3 - P_4)\, W_{fi}\, n_2 (1-n_3)(1-n_4) \;, \tag{2.18}$$

with particle labels as in the left panel of Figure 2.2, four-momenta P_i, (Fermi-Dirac) distribution functions n_i, and the transition rate W_{fi} given in terms of the spin-summed squared matrix element $\sum_\mathrm{spins} |M|^2$ as

$$W_{fi} = \frac{\sum_\mathrm{spins} |M|^2}{2^4\, 4\, E_1 E_2 E_3 E_4} \;. \tag{2.19}$$

Here, the factor 4 stems from averaging over initial-state spins. The same cross-section expression also holds for charged-current neutrino absorption with the corresponding Lagrangian/matrix element. The transition rate for neutral-current processes can be written as [48]

$$W_{fi} = G_{\mathrm{F}}^2 \left[(C_V + C_A)^2 (1 - v_2 \eta_{12})(1 - v_4 \eta_{34}) + (C_V - C_A)^2 (1 - v_2 \eta_{23})(1 - v_4 \eta_{14}) - (C_V^2 - C_A^2) \frac{m_N^2}{E_2 E_4} (1 - \eta_{13}) \right] , \tag{2.20}$$

where $v_i = p_i / E_i$ are the particle velocities, m_N is the nucleon mass, and η_{ij} is the cosine of the angle between $\boldsymbol{p}_i$ and $\boldsymbol{p}_j$. For conditions relevant in supernovae, we can consider nucleons to be non-relativistic. Hence, $v_i \ll 1$ and $E_2 E_4 \approx m_N^2$, thus the only surviving angle is $\eta_{13} \equiv \cos\theta$ and

$$W_{fi} \approx G_{\mathrm{F}}^2 \left(C_A^2 (3 - \cos\theta) + C_V^2 (1 + \cos\theta) \right) . \tag{2.21}$$

For neutrino-nucleon elastic scattering on a free nucleon of a single species, the $\delta^{(4)}$ function in Eq. (2.18) can be written as $\delta^{(3)}(\boldsymbol{p}_2 - \boldsymbol{p}_4)\delta(E_1 + E_2 - E_3 - E_4)$ and $E_2 = E_4$ from the first delta function, where we neglect neutrino momenta. Furthermore, for free particles the Pauli blocking factors vanish. We can then write Eq. (2.18) as

$$\frac{\sigma_0}{V} = 2 \int \frac{\mathrm{d}^3 p_2}{(2\pi)^3} n_2 \frac{1}{(2\pi)^2} \int \mathrm{d}E_3 \, E_3^2 \, \delta(E_1 - E_3) \int \mathrm{d}\cos\theta \, \frac{1}{(2\pi)^3} (2\pi)^4 \, W_{fi} \tag{2.22}$$

$$= n \frac{E_1^2}{2\pi} \int \mathrm{d}\cos\theta \, W_{fi} , \tag{2.23}$$

with nucleon density n. Hence, the differential cross-section is given by $(nV = N = 1)$ [49]

$$\frac{\mathrm{d}\sigma_0}{\mathrm{d}\cos\theta} = \frac{G_{\mathrm{F}}^2 E_\nu^2}{2\pi} \left(C_A^2 (3 - \cos\theta) + C_V^2 (1 + \cos\theta) \right) , \tag{2.24}$$

where $E_\nu = E_1 = E_3$ is the energy of the neutrino. This equation neglects effects of order $\mathcal{O}(E_\nu / m_N)$ stemming from phase-space corrections, recoil and weak magnetism [49].

Medium effects caused by surrounding nucleons modify the cross section. This is captured by replacing the square of the charge with a static structure factor,

$$\frac{\mathrm{d}\sigma}{\mathrm{d}\cos\theta} = \frac{G_{\mathrm{F}}^2 E_\nu^2}{2\pi} \left((3 - \cos\theta) S_A + (1 + \cos\theta) S_V \right) . \tag{2.25}$$

Here, S_A is called the static structure factor for axial response and S_V is the corresponding structure factor for vector response. They describe the response of the system to spin and density fluctuations, respectively. The structure factors contain all the information on strong interactions in the system.

To capture the dependence of the rate on the energy ω transferred to the medium, we use the more general expression

$$\frac{\mathrm{d}^2 \sigma}{\mathrm{d}\cos\theta \, \mathrm{d}E'_\nu} = \frac{G_{\mathrm{F}}^2 E'^2_\nu}{2\pi} \left((3 - \cos\theta) S_A(\omega, \boldsymbol{q}) + (1 + \cos\theta) S_V(\omega, \boldsymbol{q}) \right) , \tag{2.26}$$

where E'_ν is the energy of the outgoing neutrino that in inelastic reactions can be different from the energy of the incoming neutrino E_ν, $S_A(\omega, \boldsymbol{q})$ $\left(S_V(\omega, \boldsymbol{q})\right)$ is the dynamical (i. e., frequency dependent) structure factor for axial (vector) response and $\boldsymbol{q}$ is the momentum transferred to the medium. The static structure factor is connected to the dynamic structure factor via

$$S_A(\boldsymbol{q}) = \int_{-\infty}^{\infty} \mathrm{d}\omega \, S_A(\omega, \boldsymbol{q}) . \tag{2.27}$$

Equation (2.26) states that once the scattering angle is fixed, the only unknowns in a scattering process of a neutrino with given energy E_ν are the dynamical structure factors. Therefore, the calculation of these structure factors is a key aspect of this thesis. Quantities of astrophysical interest like energy transfers and mean-free paths

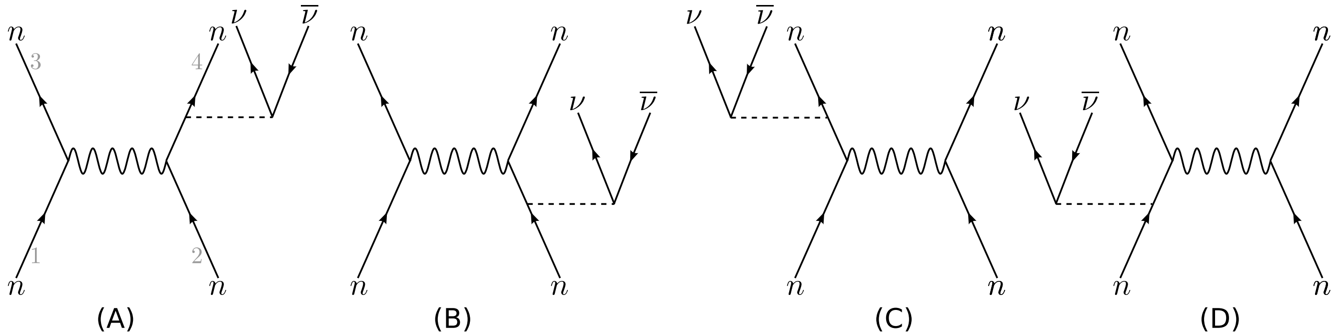

Figure 2.3: Feynman diagrams for the nn bremsstrahlung process, following Ref. [50].

(i. e., the typical distance a neutrino travels between two successive interactions) can be derived from the structure factor, see Sections 4.3 and 6.1.

Both ω and $\boldsymbol{q}^2$ can be expressed in terms of the neutrino energies,

$$\boldsymbol{q}^2 = E_\nu^2 + E_\nu'^2 - 2E_\nu E_\nu' \cos\theta \ , \tag{2.28}$$

and

$$\omega = -\left(E_\nu + E_\nu'\right) \qquad \omega \leq 0 \qquad \text{for bremsstrahlung,} \tag{2.29}$$

$$\omega = E_\nu + E_\nu' \qquad \omega \geq 0 \qquad \text{for pair absorption, and} \tag{2.30}$$

$$\omega = E_\nu - E_\nu' \qquad \omega \leq E_\nu \qquad \text{for scattering.} \tag{2.31}$$

A relation between the structure factor and the spin-summed weak interaction matrix elements for interacting nucleons can be obtained combining Refs. [50, 51], see Eq. (7.1). For nn bremsstrahlung, the symmetry factor is $s = 4$. Evaluating the Feynman diagrams in Fig. 2.3 based on the non-relativistic limit of the Lagrangian in Eq. (2.17),

$$\mathcal{L}_{nc}^{\text{non-rel}} = \frac{G_\text{F}}{\sqrt{2}} \overline{\psi}_\nu \gamma_\mu (1-\gamma_5)\psi_\nu \phi_N^\dagger (C_V \delta_{\mu 0} - C_A \delta_{\mu i} \sigma^i)\, \phi_N \ , \tag{2.32}$$

with non-relativistic nucleon spinors ϕ_N and Pauli spin matrices σ_i, one obtains for the individual diagrams [50]

$$M^{(A)} = \frac{G_\text{F}}{\sqrt{2}} \left(C_V \delta_{\mu 0} - C_A \delta_{\mu i} \sigma_2^i\right) l_\mu \frac{1}{\omega} \langle nn | \mathcal{T} | nn \rangle \ , \tag{2.33}$$

$$M^{(B)} = \frac{G_\text{F}}{\sqrt{2}} \langle nn | \mathcal{T} | nn \rangle \frac{-1}{\omega} \left(C_V \delta_{\mu 0} - C_A \delta_{\mu i} \sigma_2^i\right) l_\mu \ , \tag{2.34}$$

$$M^{(C)} = \frac{G_\text{F}}{\sqrt{2}} \left(C_V \delta_{\mu 0} - C_A \delta_{\mu i} \sigma_1^i\right) l_\mu \frac{1}{\omega} \langle nn | \mathcal{T} | nn \rangle \ , \text{ and} \tag{2.35}$$

$$M^{(D)} = \frac{G_\text{F}}{\sqrt{2}} \langle nn | \mathcal{T} | nn \rangle \frac{-1}{\omega} \left(C_V \delta_{\mu 0} - C_A \delta_{\mu i} \sigma_1^i\right) l_\mu \ . \tag{2.36}$$

The vector part cancels pairwise by adding diagrams A and B and diagrams C and D, thus

$$M = -\frac{G_\text{F}}{\sqrt{2}} \frac{C_A}{\omega} l_i \left[\sigma_1^i + \sigma_2^i, \langle nn | \mathcal{T} | nn \rangle\right] \ . \tag{2.37}$$

The lepton trace is given by [50]

$$\text{Tr}\,(l_j^\dagger l_i) = 8\left(q_{1j} q_{2i} + q_{1i} q_{2j} + \omega_1 \omega_2\, g_{ij} + i\varepsilon_{i\alpha j\beta} q_1^\alpha q_2^\beta\right) \ , \tag{2.38}$$

with lepton four-momenta $q^{\alpha}_{1,2}$, lepton energies $\omega_{1,2}$, metric tensor g_{ij}, and antisymmetric tensor of rank four $\varepsilon_{i\alpha j\beta}$.

Performing the spin sum over the squared matrix element, we obtain

$$\begin{aligned}
\sum_{\text{spins}} |M|^2 &= \mathrm{Tr}_{\sigma_1\sigma_2} |M|^2 \qquad (2.39)\\
&= 8\frac{G_{\mathrm{F}}^2}{2} C_A^2 \frac{\omega_1\omega_2}{\omega^2} \sum_{m_{s_1} m_{s_2}} \left\langle m_{s_1} m_{s_2} \right| \left[\sigma_1^i + \sigma_2^i, \langle nn|\mathcal{T}|nn\rangle^*\right] \left(\sum_{m_{s_3} m_{s_4}} \left| m_{s_3} m_{s_4} \right\rangle \left\langle m_{s_3} m_{s_4} \right| \right)\\
&\quad \times \left[\sigma_1^i + \sigma_2^i, \langle nn|\mathcal{T}|nn\rangle\right] \left| m_{s_1} m_{s_2} \right\rangle \qquad (2.40)\\
&= 8\frac{G_{\mathrm{F}}^2}{2} C_A^2 \frac{\omega_1\omega_2}{\omega^2}\, 3\cdot 4 \sum_{\{m_{s_i}\}} |\langle nn|\mathcal{T}|nn\rangle|^2 \left(m_{s_1} + m_{s_2} - m_{s_3} - m_{s_4}\right)^2 . \qquad (2.41)
\end{aligned}$$

In Eq. (2.40), we utilize the fact that only the g_{ij} part in the lepton trace survives [50]. Going to Eq. (2.41), we then assume rotational symmetry, $\sigma^x = \sigma^y = \sigma^z$.

2.3 Neutrino Signal

The neutrinos are not only key to the explosion mechanism, they can also be detected on Earth. Since neutrinos can free-stream much earlier than photons, they provide us with information from the central part of the supernova explosion that is inaccessible by electromagnetic observations. So far, neutrinos linked to only one supernova were seen, namely SN 1987A (Figure 1.1 b,c). SN 1987A is located in the Large Magellanic Cloud, about 170 000 light-years away. Hence, in the order of 10^{28} neutrinos reached Earth, 24 of which were detected in the Kamiokande II, IMB, and Baksan neutrino experiments, the first direct connection between supernovae and neutrinos and the first measurement of neutrinos from a source more distant than the sun.

The measured energies, averaging 15 MeV, are in agreement with conditions expected in supernovae (Section 2.4) and neutrino signals predicted by simulations (Figure 2.4). The burst lasted about twelve seconds which is also

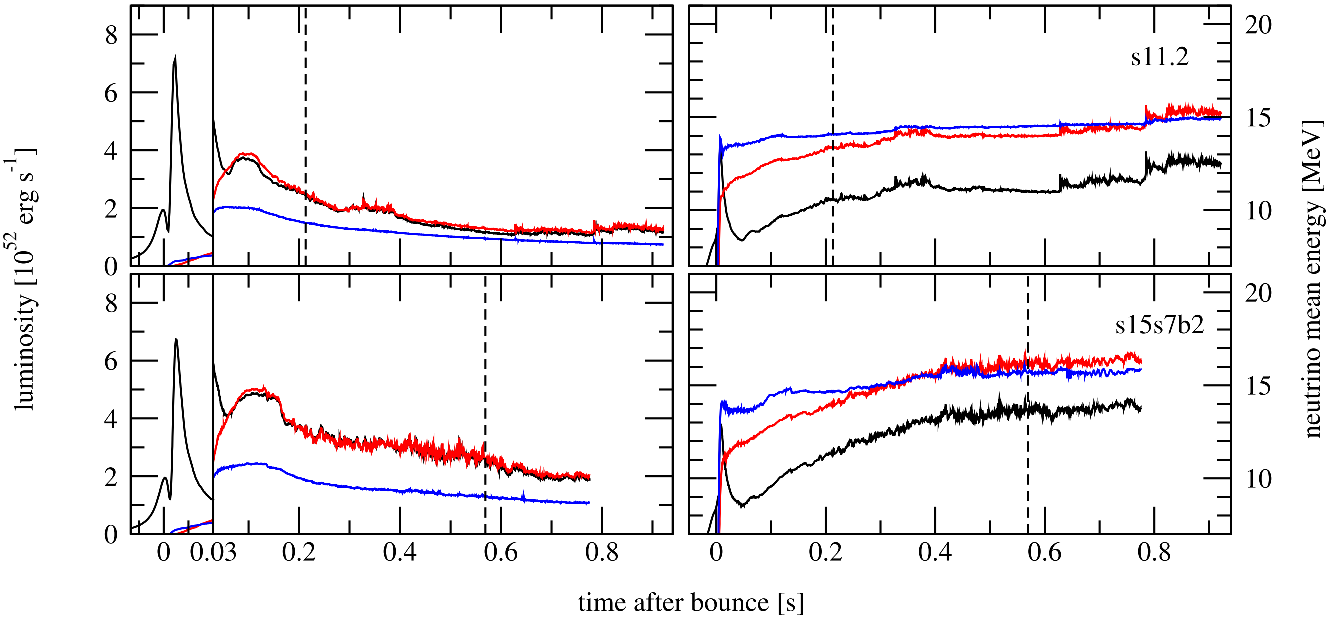

Figure 2.4: Neutrino spectrum predicted by axially-symmetric simulations of $11.2\,M_\odot$ (top) and $15\,M_\odot$ (bottom) progenitor stars. Shown is the total luminosity (left) and mean neutrino energy (right) for electron neutrinos (black), electron antineutrinos (red), and μ/τ neutrinos (blue). Note the different scale for the initial neutrino burst: For the first 30 ms after bounce, the luminosity has been scaled down by a factor of 5. The dashed line indicates the onset of explosion. From [52].

in agreement with predictions. The small number and mediocre energy resolution do not allow for a detailed discussion of the spectrum. More advanced detectors have been built since 1987 that promise a much cleaner spectrum measurement from the next galactic supernova based on thousands of detected neutrinos [53].

A neutrino spectrum prediction is shown in Figure 2.4. During collapse, a large amount of protons is converted to neutrons (via $p+e^- \rightarrow n+\nu_e$), producing a huge number of electron neutrinos. At densities above $\rho = 10^{12}\,\mathrm{g\,cm^{-3}}$, matter is opaque enough to neutrinos such that the diffusion time scale is longer than the collapse time scale [54]. Neutrinos are effectively trapped in the collapsing core. This effect is visible as the dip in the ν_e luminosity around bounce. As the shock reaches less dense regions of the core a few milliseconds after bounce, these neutrinos become free-streaming at more or less the same time, creating the burst of electron neutrinos seen in the luminosity spectra in Fig. 2.4. Electron neutrinos are already emitted before bounce while other species only appear after bounce.

More neutrinos continue to be produced mostly through thermal processes discussed in Section 2.2. In the center of the explosion, reactions are frequent and neutrinos are essentially in thermal equilibrium as the medium is opaque to them. They diffuse out to less dense regions where the medium eventually becomes transparent and they become free-streaming. The average surface of last interaction is called the neutrinosphere. One can distinguish between a sphere of last energy-exchange (the energy sphere) and a sphere of last interaction (the scattering sphere). The neutrinosphere is an idealized concept. Beyond the neutrinosphere, the neutrino energy spectrum is assumed to stay fixed. As interactions are energy dependent, the neutrinosphere positions are a function not only of the medium, but also of neutrino energy. Often, an energy-averaged neutrinosphere is discussed.

Since muon and tau (anti)neutrinos (collectively denoted ν_x) do not participate in charged-current processes (see Section 2.2), their total opacity is lower than for ν_e and $\overline{\nu}_e$ and they therefore decouple first, i. e., their average radius of last interaction / their neutrinosphere is furthest inside the explosion. As supernova matter is neutron rich, the opacity for electron-neutrino capture on neutrons (2.5) is higher than for electron-antineutrino capture on protons (2.6), hence electron antineutrinos decouple at higher densities than electron neutrinos. Due to the thermal equilibrium, the typical energies of the neutrinos beyond the neutrinosphere depend on the temperature at the moment of decoupling. In supernovae, temperature decreases with radius (see, e. g., Figure 5.2), so we expect the following hierarchies for the neutrinosphere positions R_ν and mean neutrino energies $\langle E_\nu \rangle$:

$$R_{\nu_x} < R_{\overline{\nu}_e} < R_{\nu_e} \qquad \text{and} \tag{2.42}$$

$$\left\langle E_{\nu_x} \right\rangle > \left\langle E_{\overline{\nu}_e} \right\rangle > \left\langle E_{\nu_e} \right\rangle \,. \tag{2.43}$$

This mean-energy hierarchy can be seen in Fig. 2.4. At later times in the accretion phase, a local temperature maximum causes the change in hierarchy also seen in Fig. 2.4 [53].

Details of the spectrum will depend both on the thermodynamic conditions predicted by the simulation and on the neutrino interactions. Some neutrino flavors are only produced in certain reactions. Interactions can also convert neutrinos from one flavor to another and/or change the energy of the neutrinos (Section 2.2). Detailed theoretical understanding is thus key to the interpretation of any neutrino spectra observed in the future.

2.4 Supernova Conditions and Nucleosynthesis

Figure 2.5 shows some of the extreme conditions encountered in supernova simulations: Already in the initial collapse, densities reach beyond nuclear saturation density ($2.7 \times 10^{14}\,\mathrm{g\,cm^{-3}}$ or $0.16\,\mathrm{fm^{-3}}$). The temperatures reach 50 MeV, roughly 580 billion Kelvin. The typical electron fraction is between 0.05 and 0.33.

The redder the color in Figure 2.5, the more material encounters the corresponding thermodynamic conditions. A large fraction of the material lies close to the dashed line represented by the following relation between temperature T and density ρ [57]:

$$T_{\mathrm{SN}}(\rho) = 3 \left(\frac{\rho}{10^{11}\,\mathrm{g\,cm^{-3}}} \right)^{1/3} \mathrm{MeV}\,. \tag{2.44}$$

Throughout this thesis, we will often rely on this relation to parametrize temperature in terms of density. The entropy of an (ultra)relativistic Fermi gas scales like $S \sim T^3/\rho$ and if we neglect neutrino heating, the shocked matter expands approximately adiabatically, yielding $\rho \sim T^{1/3}$. This further motivates our parametrization [57].

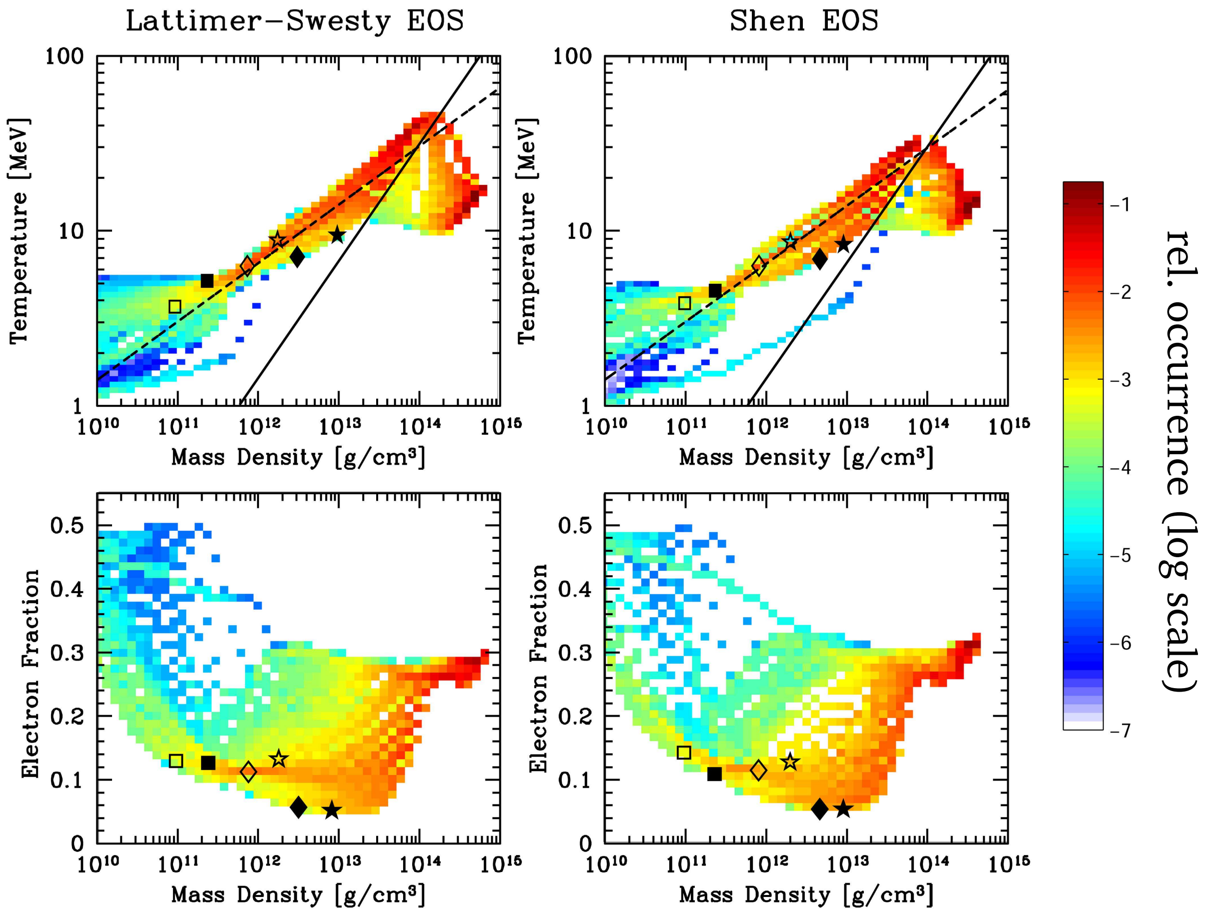

Figure 2.5: Thermodynamical conditions found in supernova simulations of a 15 $M_\odot$ star. Shown are results with the Lattimer-Swesty (left) and Shen (right) equations of state [55, 56]. Plotted is the temperature (top) and electron fraction (bottom) versus density. The color codifies how much matter is subject to a specific set of conditions, with red being abundant and blue rare conditions. Note that the scale is logarithmic. The solid line indicates the Fermi temperature, the dashed line the parametrization in Eq. (2.44). The symbols indicate neutrino decoupling conditions, see original source for details. From [57].

The solid line indicates the region where the temperature is equal to the Fermi temperature, i. e., where matter starts to become degenerate. The two lines cross at about $10^{14}\,\mathrm{g\,cm^{-3}}$. Since the most interesting region is around the neutrinosphere, which is typically in the $10^{11}-10^{13}\,\mathrm{g\,cm^{-3}}$ density range, we will assume non-degenerate conditions.

In addition to the region around the dashed line, matter in Fig. 2.5 also accumulates in the high-density, intermediate temperature region that is well beyond the solid line and therefore strongly degenerate. This is the region of the proto-neutron star. For neutrino reactions this region is of less interest as the densities are so high that neutrinos are trapped and in chemical equilibrium, hence modifications of their reaction rates do not have a significant impact.

Supernovae are also an important site for nucleosynthesis. The key site is the so-called neutrino-driven wind (NDW): After the explosion is under way, the hot proto-neutron star cools off by emitting neutrinos through thermal processes. Some of these neutrinos are absorbed in the outer layers of the proto-neutron star, heating the material and creating a low-mass supersonic outflow of protons and neutrons that lasts tens of seconds. As the material reaches cooler regions, nucleosynthesis starts.

The nucleosynthesis processes in the NDW are governed mostly by entropy, electron fraction, and expansion time scale. Neutrinos play a crucial role setting the electron fraction through the charged-current processes discussed in Section 2.2. In weak equilibrium, Y_e is given by [58]

$$Y_e \approx \left[1+\frac{L_{\bar{\nu}_e}(\epsilon_{\bar{\nu}_e}-2\Delta+1.2\Delta^2/\epsilon_{\bar{\nu}_e})}{L_{\nu_e}(\epsilon_{\nu_e}+2\Delta+1.2\Delta^2/\epsilon_{\nu_e})}\right]^{-1}, \qquad (2.45)$$

with electron neutrino and antineutrino mean energies $\epsilon_{\nu_e}, \epsilon_{\overline{\nu}_e}$ and luminosities (i. e., energy radiated per time) $L_{\nu_e}, L_{\overline{\nu}_e}$ and neutron-proton mass difference $\Delta = m_n - m_p \approx 1.29\,\mathrm{MeV}$. Conditions are found to be neutron rich (i. e., $Y_e < 0.5$) if the energy difference fulfills

$$\epsilon_{\overline{\nu}_e} - \epsilon_{\nu_e} \gtrsim 4\Delta \approx 5\,\mathrm{MeV}\,. \tag{2.46}$$

As the mean neutrino energy is set by the opacities (see Section 2.3), a detailed understanding of neutrino reaction rates is key for predicting the nucleosynthesis conditions in the NDW.

The r-process (short for rapid neutron capture process) is thought to synthesize about half of the elements heavier than iron. In a hot and neutron-rich environment, neutrons are captured on seed nuclei faster than typical β-decay timescales. The r-process requires a high neutron-to-seed ratio which in turn requires high entropy and neutron-rich conditions. Neutrino-driven winds were thought to be a good candidate, but recent simulations show unfavorable conditions for a robust r-process [59, 60]. In proton-rich conditions, the νp-process [61] can create heavy elements on the proton-rich side of the nuclear chart. Proton captures create isotopes with long β-decay half-lifes that inhibit the flow to heavier isotopes. The νp-process circumvents this using electron-antineutrino capture on protons to create free neutrons (reverse reaction of (2.6)) that are quickly captured on these isotopes, thus bypassing the β-decay time scales. Reviews of the nucleosynthesis processes in the context of supernovae can be found in Refs. [54, 59, 60].

2.5 Simulating Supernovae

Core-collapse supernovae combine physics from various areas such as thermodynamics, quantum mechanics, theory of gravity, radiation transport, (magneto)hydrodynamics, particle and nuclear physics. All four fundamental forces of nature play a key role. To simulate supernovae numerically, the problem has to be discretized and solved on a grid. The grid resolution has to be fine enough to capture all relevant physics, especially small-scale turbulences

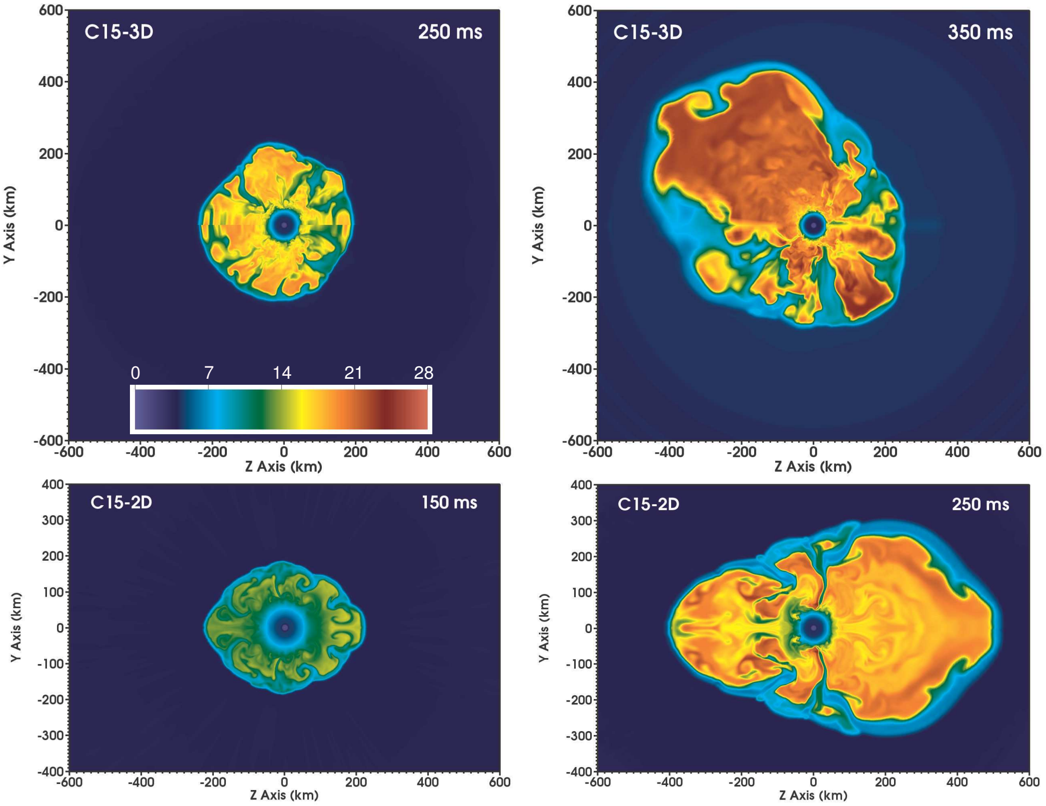

Figure 2.6: Fully three-dimensional (top) and axially-symmetric (bottom) supernova simulations of a 15 $M_\odot$ progenitor star at comparable times of the explosion. Color-coded is the entropy. From [18].

and the shock. Supernova simulations are currently mostly limited by the available computer resources. Only in the last few years have three-dimensional simulations with detailed neutrino treatment become feasible. They tend to underestimate the explosion energy compared to observations [23, 62–64].

The simplest approximation to speed up the simulation is to impose symmetries. If one assumes spherical symmetry, the angular dependence vanishes and the problem has been reduced to a one-dimensional ($1D$) calculation. As mentioned earlier in this chapter, supernovae are non-spherical and multi-dimensional effects such as turbulence are crucial for a successful explosion. Nevertheless, $1D$ simulations are still widely used as parameter studies in $3D$ are unfeasible with today's resources. Since $1D$ simulations do not explode on their own, the explosion has to be triggered artificially. In $2D$ simulations, axial symmetry is imposed. This allows for turbulence and the SASI mode as well as continued accretion, allowing for successful explosions without artificial triggers. It does however create an artificial preferred axis along which most models explode (see Figure 2.6).

To complicate things further, various levels of sophistication on the theory input (i. e., Newtonian vs. general relativistic gravity [42, 65], different approximations of neutrino transport [66], and so on) have been shown to have a great impact on the supernova, even deciding whether the star will explode or not. Neutrino rates (a better calculation of which is the subject of this thesis) are also important: It was shown that a 15 % change in a coupling parameter that is included in the calculation of some of the rates can make the difference between a successful and a (marginally) failed explosion [45].

More work is necessary on various fronts to consistently reproduce real-world supernovae with the observed explosion energies of 10^{51} erg with realistic theoretical input.

3 Strong Interactions and Chiral Effective Field Theory

Neutrino reactions with interacting nucleons are the central topic of this thesis. In this chapter, we introduce the descriptions of nuclear interactions employed in our work, which are necessary to calculate the structure factor for these reactions. We begin with a short introduction to effective theories (which was already used in Ref. [67]) and the fundamental theory of nuclear forces, quantum chromodynamics. After that, we introduce chiral effective field theory and the T-matrix formalism as well as methods to make the potential more soft and to include three-nucleon interactions.

3.1 What is an Effective Theory?

In order to solve a physical problem exactly, one would need to start from the most fundamental theory and consider every degree of freedom. While there might be a few textbook problems that can be approached that way, most problems require a description that takes into account only the relevant degrees of freedom and only the relevant scales for the given problem. For example, when calculating the potential energy liberated when an object falls from a table, rather than using general relativity, it is much more feasible to use Newtonian gravity or even simply the equation most people have seen in school,

$$V = -mgh\,, \tag{3.1}$$

where the potential V is described in terms of the mass m and initial height h of the object times the (local) gravitational acceleration of the Earth g. This is an effective theory valid only near the surface of the Earth, i. e., where h is much smaller than the radius of the Earth $r_\oplus$ (and even on the surface, g varies slightly). The easier computability comes at the cost of a smaller range of validity compared to the more general Newtonian gravity, which in turn is an effective theory of both general relativity and quantum mechanics.

Effective theories typically work because of a separation of scales. In the example above, we required $h \ll r_\oplus$. The better this condition is fulfilled, the more exact are the results. Often, effective theories provide an expansion in terms of the small scale. The better the separation of scales, the smaller the number of terms required to achieve a given accuracy.

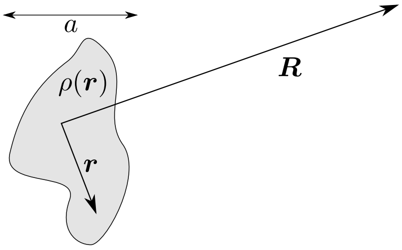

Figure 3.1: Calculating the potential $V(\boldsymbol{R})$ of a localized charge distribution $\rho(\boldsymbol{r})$

Let us consider another example from classical physics, the multipole expansion of electric potentials. Consider a localized charge distribution $\rho(\boldsymbol{r})$ with a typical size a (Figure 3.1). The potential at position $\boldsymbol{R}$ is in general given by

$$V(\boldsymbol{R}) \sim \int \mathrm{d}^3 r \, \frac{\rho(\boldsymbol{r})}{|\boldsymbol{R}-\boldsymbol{r}|}\,. \tag{3.2}$$

If the distance R is large compared to the size of the charge distribution $r \lesssim a \ll R$, we can expand the denominator in a Taylor series,

$$\frac{1}{|\boldsymbol{R}-\boldsymbol{r}|} = \frac{1}{R} + \frac{\boldsymbol{r}\cdot\boldsymbol{R}}{R^3} + \mathcal{O}\left(\frac{1}{R^3}\right)\,. \tag{3.3}$$

The potential can then be written as

$$V(\boldsymbol{R}) = \frac{q}{R} + \frac{\boldsymbol{P}\cdot\boldsymbol{R}}{R^3} + \mathcal{O}\left(\frac{1}{R^3}\right) , \tag{3.4}$$

with charge $q = \int \mathrm{d}^3 r \rho(\boldsymbol{r})$ and dipole moment $\boldsymbol{P} = \int \mathrm{d}^3 r \rho(\boldsymbol{r})\boldsymbol{r}$. It can easily be seen that these low-order moments have to be calculated only once (as they are independent of $\boldsymbol{R}$) and describe the system well at each point $\boldsymbol{R}$ that is sufficiently far away from the charge distribution. For probes at large distances it is therefore sufficient to compute these moments instead of solving Eq. (3.2) exactly. At smaller distances, more and more terms need to be taken into account until at some point, the effective theory breaks down.

A similar concept will be used for nuclear forces in Section 3.3.

3.2 QCD and Chiral Symmetry Breaking

Quantum chromodynamics (QCD) is the fundamental theory of nuclear forces. The elementary particles of QCD are six spin-1/2 fermions named quarks listed in Table 3.1. Each quark carries a color charge (red, green, or blue), while antiquarks carry anti-red, anti-green, or anti-blue. The gauge bosons of QCD are gluons, carrying color charges themselves. The concept of confinement requires color-neutral combinations of (anti)quarks. Possible color-neutral objects are made of three (anti)quarks, forming a so-called (anti)baryon (like the neutron: one up and two down quarks) or a quark and an antiquark forming a meson (like the pion). Recently, the existence of a pentaquark state consisting of four quarks and one antiquark was confirmed at the LHC [68] and there are indications of tetraquark states [69]. At high temperatures or densities, this confinement is broken and a quark-gluon plasma is formed.

	Flavor	Mass	Electric charge	Isospin
u	up	$2.3^{+0.7}_{-0.5}$ MeV	$2/3\,e$	$+1/2$
d	down	$4.8^{+0.5}_{-0.3}$ MeV	$-1/3\,e$	$-1/2$
s	strange	95 ± 5 MeV	$-1/3\,e$	0
c	charm	$1\,275 \pm 25$ MeV	$2/3\,e$	0
b	bottom	$4\,660 \pm 30$ MeV	$-1/3\,e$	0
t	top	$173\,210 \pm 510 \pm 710$ MeV	$2/3\,e$	0

Table 3.1: Mass, electric charge and isospin of the six quarks. Data taken from Ref. [70].

The QCD Lagrangian is given by

$$\mathcal{L} = \sum_f \left(\bar{q}_f i\not{D} q_f - m_f \bar{q}_f q_f\right) - \frac{1}{2}\mathrm{Tr}\, G_{\mu\nu}G^{\mu\nu} , \tag{3.5}$$

with quark fields q_f and masses m_f. The flavor index f runs over the quarks in Table 3.1. Furthermore, $\not{D} \equiv \gamma^\mu D_\mu$ is the Feynman slash notation, $D_\mu = \partial_\mu + igA_\mu$ the covariant derivative, g a dimensionless coupling strength, A_μ the gluon fields and $G_{\mu\nu}$ the gluon field strength with components given by

$$G^a_{\mu\nu} = \partial_\mu A^a_\nu - \partial_\nu A^a_\mu + g f^{abc} A^b_\mu A^c_\nu . \tag{3.6}$$

Here, $a, b, c = 1, \ldots, 8$ and f^{abc} are the $SU(3)$ structure constants.

The coupling is typically described in terms of the strong coupling strength α_s, given at 1-loop order by

$$\frac{g^2}{4\pi} \equiv \alpha_s = \frac{6\pi}{33 - 2N_F} \log^{-1} \frac{Q}{\Lambda_{\mathrm{QCD}}} , \tag{3.7}$$

assuming an energy range where the number of flavors is constant. Here, N_F is the number of flavors, Q the momentum scale and $\Lambda_{\mathrm{QCD}} \approx 200 - 400$ MeV the characteristic scale of QCD. Note that the coupling is the same, independent of quark flavor. Because of its significant momentum dependence (see Figure 3.2), α_s is called a

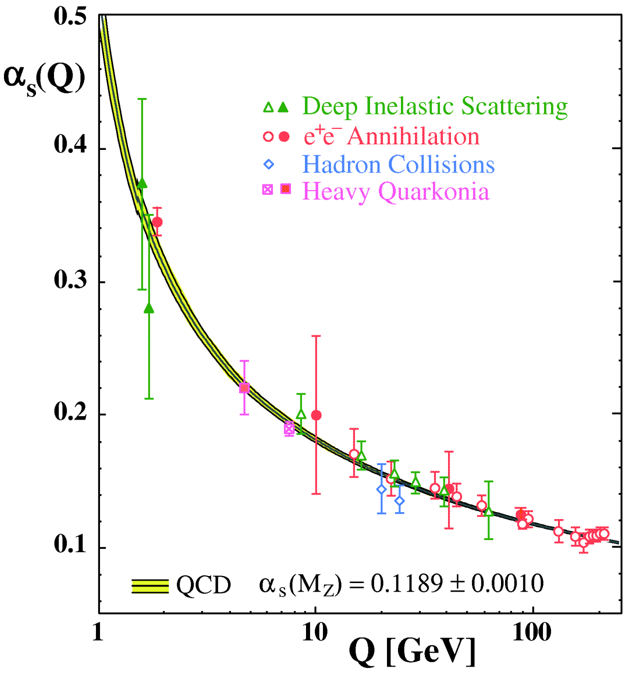

Figure 3.2: Running coupling α_s as a function of momentum Q, summarizing data from different experimental methods and globally averaged QCD results. From Ref. [71].

running coupling. This was derived by Gross, Politzer, and Wilczek, who were awarded the 2004 Nobel Prize in Physics. At high momentum scales, the coupling becomes small and QCD becomes perturbative, an effect known as asymptotic freedom. At the low momentum scales of nuclear physics, however, the coupling is very strong and QCD is non-perturbative.

For nuclear physics it is sufficient to only consider the three light quarks (light compared to typical nucleonic mass scales $\sim 1\,\text{GeV}$). The QCD Lagrangian has a very compact form. In principle, nuclear physics is determined by only five parameters: The masses of the light quarks, Λ_{QCD}, and – since protons also interact via the Coulomb force – the electromagnetic fine structure constant $\alpha \approx \frac{1}{137}$.

However, the non-perturbativeness at low energies and the fact that gluons carry color charge and hence interact with other gluons (unlike the uncharged photons of quantum electrodynamics) make a direct calculation of nuclear physics in terms of quarks and gluons infeasible.

One approach to circumvent this is lattice QCD, using a four-dimensional Euclidean lattice as a discretized space-time grid with quarks on the sites and gluons on the links. Path integrals can then be evaluated numerically and the results have to be extrapolated to infinite volume and vanishing lattice spacing. This approach is currently limited to very small systems or unphysical quark/pion masses (see for example Refs. [72–74]).

A different, older approach are phenomenological nuclear potentials like Argonne v_{18} [75] and CD-Bonn [76]. They were constructed to reproduce nucleon-nucleon scattering very accurately and describe nuclear structure reasonably well. However, they do not have a clear connection to the underlying fundamental theory of QCD. Another approach are density functionals that have a lot of free parameters that need to be fit to data in the mass region of interest. This is a problem when one tries to calculate properties of nuclei far away from the valley of stability where no experimental data is available. One important example are nuclei close to the neutron dripline relevant for r-process nucleosynthesis [77, 78].

A fourth approach is chiral effective field theory, which is constructed to be consistent with the symmetries of QCD. Before we get to this approach in the next section, let us take a look at these symmetries, following the discussion in Ref. [79] and again considering only the light quarks.

The kinetic term of Eq. (3.5) can be written in terms of left- and right-handed quarks by using the projection operators $(1 \mp \gamma_5)/2$, respectively, yielding

$$\sum_f \bar{q}_f i\not{D} q_f = \sum_f \left(\bar{q}_{Lf} i\not{D} q_{Lf} + \bar{q}_{Rf} i\not{D} q_{Rf} \right) . \tag{3.8}$$

This expression is symmetric under rotations of the left- and right-handed quarks by independent unitary matrices. However, the $U(3)_L \times U(3)_R$ symmetry is not realized in a quantum theory due to anomalies in the $U(1)_A$ transformation [79]. Hence, the expression exhibits a $U(1)_V \times SU(3)_L \times SU(3)_R$ symmetry. The $U(1)_V$ symmetry corresponds to the baryon number, while the remaining $SU(3)_L \times SU(3)_R$ symmetry is called chiral symmetry. Since the masses of the light quarks are small, but not zero, this symmetry is only approximate. It is explicitly broken by the quark mass term coupling left- and right-handed quarks:

$$\sum_f m_f \bar{q}_f q_f = \sum_{ff'} \left(\bar{q}_{Rf} M_{ff'} q_{Lf'} + \bar{q}_{Lf} M_{ff'} q_{Rf'} \right) , \quad \text{with} \quad M = \begin{pmatrix} m_u & & \\ & m_d & \\ & & m_s \end{pmatrix} . \tag{3.9}$$

In addition, the symmetry is spontaneously broken by the QCD vacuum, resulting in isospin symmetry (generalized to three quarks) $SU(3)_V \subset SU(3)_L \times SU(3)_R$, i. e., it is symmetric under a simultaneous rotation of left- and right-handed quarks by the same matrix. According to Goldstone's theorem [80], a massless Goldstone boson exists if a continuous symmetry is spontaneously broken. One would thus expect eight Goldstone bosons, one for each of the eight broken generators of $SU(3)_L \times SU(3)_R$.

Since chiral symmetry is not an exact symmetry of QCD for nonvanishing quark masses, these bosons are not massless, but have a small mass and are called pseudo-Goldstone bosons. They can be identified as the pions, kaons, and the eta meson. This is the reason why pions (which have no strange quark) are significantly lighter than other hadrons.

3.3 Chiral Effective Field Theory

The concept of chiral EFT was developed by Steven Weinberg [81, 82]. The first step is to pick the right degrees of freedom. As Weinberg [83] pointed out: "You can use any degrees of freedom you want, but if you use the wrong ones, you'll be sorry." At densities below or in the order of the nuclear saturation density, the relevant degrees of freedom are nucleons and pions. Then, write down the most general Lagrangian in terms of pions and nucleons that is consistent with the symmetries of QCD, in particular chiral symmetry and its spontaneous and explicit breaking. This produces an infinite number of terms with infinite order in derivatives.

Obviously, it is not possible to evaluate an infinite number of terms. Therefore, a power-counting scheme is required which allows to order terms by their importance and then truncate the series at a given order. Weinberg power counting states that the order $(Q/\Lambda_b)^\nu$ a connected diagram belongs to is given by

$$\nu = -4 + 2N + 2L + \sum_{\text{vertices}} \Delta_i , \tag{3.10}$$

where N is the number of nucleon lines, L the number of loops, and $\Delta_i = d_i + n_i/2 - 2$ with d_i the number of derivatives or m_π insertions and n_i the number of nucleon lines at that vertex. Here, Q is the momentum scale of the problem, which in case of nuclear physics is comparable to the pion mass, $m_\pi \approx 140\,\text{MeV}$, and Λ_b is the breakdown scale of the theory, i. e., the scale at which additional physics has to be taken into account. It is typically taken to be of order 500 MeV, below the mass of the rho meson. Therefore, each subsequent order is (naively) expected to be a factor of 1/3 smaller in size. In reality, it is not as straight-forward and the convergence behavior of chiral EFT for nucleons is still under investigation.

The leading- and next-to–leading-order chiral Lagrangians are given by [84]

$$\begin{aligned} \mathcal{L}^{(0)} = {} & \frac{1}{2} \partial_\mu \boldsymbol{\pi} \cdot \partial^\mu \boldsymbol{\pi} - \frac{1}{2} m_\pi^2 \boldsymbol{\pi}^2 + N^\dagger \left[i\partial_0 + \frac{g_A}{2F_\pi} \boldsymbol{\tau} \boldsymbol{\sigma} \cdot \boldsymbol{\nabla} \boldsymbol{\pi} - \frac{1}{4F_\pi^2} \boldsymbol{\tau} \cdot (\boldsymbol{\pi} \times \dot{\boldsymbol{\pi}}) \right] N \\ & - \frac{1}{2} C_S (N^\dagger N)(N^\dagger N) - \frac{1}{2} C_T (N^\dagger \boldsymbol{\sigma} N)(N^\dagger \boldsymbol{\sigma} N) + \ldots \qquad \text{and} \end{aligned} \tag{3.11}$$

$$\begin{aligned} \mathcal{L}^{(1)} = {} & N^\dagger \left[4c_1 m_\pi^2 - \frac{2c_1}{F_\pi^2} m_\pi^2 \boldsymbol{\pi}^2 + \frac{c_2}{F_\pi^2} \dot{\boldsymbol{\pi}}^2 + \frac{c_3}{F_\pi^2} (\partial_\mu \boldsymbol{\pi} \cdot \partial^\mu \boldsymbol{\pi}) - \frac{c_4}{2F_\pi^2} \varepsilon_{ijk}\, \varepsilon_{abc}\, \sigma_i \tau_a (\nabla_j\, \pi_b)(\nabla_k\, \pi_c) \right] N \\ & - \frac{D}{4F_\pi} (N^\dagger N)(N^\dagger \boldsymbol{\sigma} \boldsymbol{\tau} N) \cdot \boldsymbol{\nabla} \boldsymbol{\pi} - \frac{1}{2} E\, (N^\dagger N)(N^\dagger \boldsymbol{\tau} N) \cdot (N^\dagger \boldsymbol{\tau} N) + \ldots , \end{aligned} \tag{3.12}$$

with pion fields $\boldsymbol{\pi}$, nucleon fields N, spin and isospin Pauli matrices $\boldsymbol{\sigma}$ and $\boldsymbol{\tau}$, weak coupling constant g_A, and pion decay constant F_π. Furthermore, C_S, C_T, c_i, D, and E are coupling constants and the ellipses indicate terms involving more pion fields. These Lagrangians describe the vertices corresponding to the order in the chiral Lagrangian (with $\Delta_i = 0, 1$ for Eq. (3.11) and (3.12), respectively).

The leading-order (LO, $\nu = 0$) potential is given by two-body diagrams without loops and higher-order vertices. The only possibilities are one-pion exchange (OPE) and central contact-interaction terms (top left panel in Figure 3.3),

$$V_{\mathrm{LO}} = V_{\mathrm{OPE}} + V_{\mathrm{central}} = -\left(\frac{g_A}{2F_\pi}\right)^2 \frac{\boldsymbol{\sigma}_1 \cdot \boldsymbol{k} \boldsymbol{\sigma}_2 \cdot \boldsymbol{k}}{k^2 + m_\pi^2} \boldsymbol{\tau}_1 \cdot \boldsymbol{\tau}_2 + C_S + C_T \boldsymbol{\sigma}_1 \cdot \boldsymbol{\sigma}_2 \,. \tag{3.13}$$

At small momentum transfer $\boldsymbol{k}$, the central terms dominate.

Due to parity conservation, no NN contact vertex with $\Delta_i = 1$ is allowed, hence the next-to-leading order (NLO) has $\nu = 2$. Two-nucleon diagrams contributing at this order either have a loop created by two pion exchanges or a contact interaction with two derivatives. At next-to–next-to–leading order (N^{2}LO), two-pion exchanges having one πN vertex from $\mathcal{L}^{(1)}$ instead of $\mathcal{L}^{(0)}$ (i. e., with $\Delta_i = 1$) appear. There are no contact interactions at this order.

One would expect three-body forces to appear at $\nu = -4 + 2 \cdot 3 + 2 \cdot 0 + 0 = 2$. However, they were shown to cancel in the calculations [86] and only appear at N^{2}LO. Four-body forces appear as expected at next-to–next-to–next-to–leading order (N^{3}LO). The complete hierarchy of chiral interactions up to N^{3}LO can be seen in Figure 3.3.

One- and two-pion exchanges describe the long-range parts of the nuclear interaction. Shorter-range interactions can be understood as the exchange of heavier particles. As these particles are not degrees of freedom in chiral EFT, their impact is subsumed in contact terms and vertices associated with low-energy constants (LECs), as illustrated in Figure 3.4. Experimental data contains the full strong interaction, so by fitting the LECs to experimental data, this short-range/high-momentum physics is included in the theory. Single-nucleon LECs are typically fit to πN scattering data and contact LECs to NN scattering data. The LECs play the same role as the multipole moments in Section 3.1.

The LECs in the two-pion exchange diagram of the N^{2}LO three-body force are the same that appear in the two-body diagrams. The only LECs that appear when including three-body forces are c_D and c_E, connected to the one-pion-exchange–contact and the three-body-contact diagrams, respectively. As they only appear in the three-body sector,

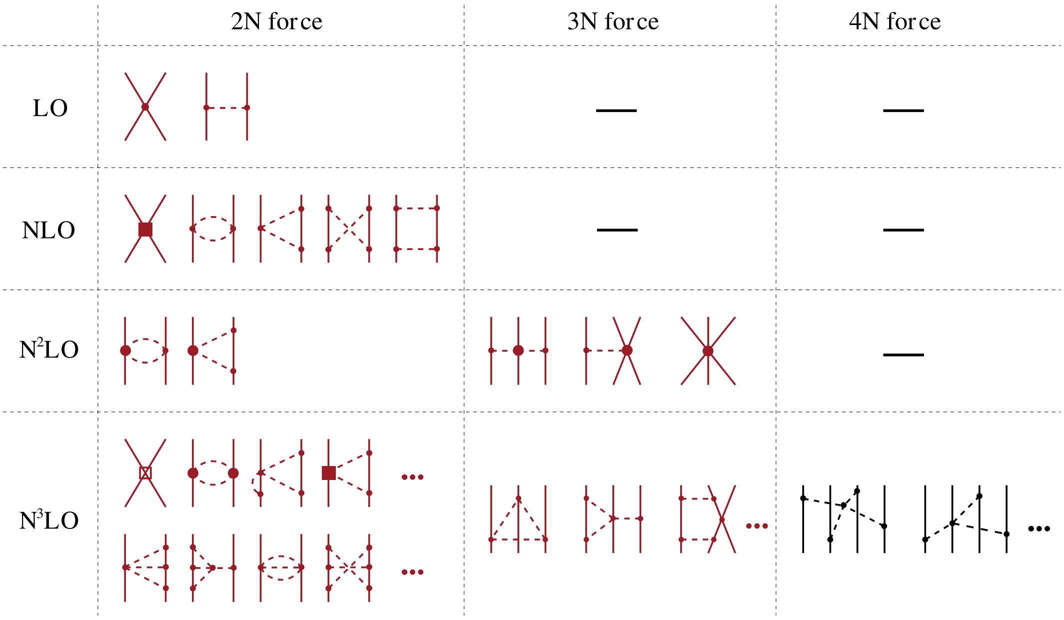

Figure 3.3: Hierarchy of chiral two-, three- and four-nucleon interactions up to N^{3}LO. Solid lines symbolize nucleons, while pions are represented by dashed lines. Diagrams shown in red are included in the potentials used in this thesis. The right diagram in the leading-order 2N force is the one-pion-exchange diagram used as a baseline throughout this thesis. From Ref. [85], colored.

Figure 3.4: Illustration of LECs/higher-order vertices containing unresolved physics. Left: The rho meson is treated as heavy and absorbed into a contact interaction. Right: The Δ excitation is not resolved in Δ-less chiral EFT and instead treated as a higher-order vertex.

these LECs have to be fit to few-body data, like the triton binding energy or the alpha particle charge radius. There are no new LECs in the three- and four-body forces at N^{3}LO.

With this construction, chiral effective field theory provides nuclear potentials that are closely connected to QCD (by respecting the same symmetries) and can be systematically expanded. Calculations can be improved by taking higher orders into account. It also allows to estimate the uncertainty stemming from the truncation at a given order. This way, chiral EFT is not a model (in the sense of the phenomenological models), the individual terms are not arbitrary, and the same constants appear in two- and many-body forces (and two-body currents), providing consistency.

Nucleons can be excited to Δ baryons with a mass of 1232 MeV. Hence, the relevant energy scale for Δ baryons is $m_\Delta - m_N \approx 300\,\text{MeV} < \Lambda_b$. By explicitly including Δ baryons in chiral EFT, new diagrams appear and the hierarchy changes. A better convergence pattern is expected. In this thesis, we will use the standard, delta-less chiral EFT.

Most calculations use an inconsistent order of chiral EFT, which incorporates two-body interactions up to N^{3}LO and the leading three-body interactions at N^{2}LO. Three-body forces were shown to be necessary in order to obtain, e. g., the neutron drip-line location in oxygen [87] or saturation properties in infinite symmetric nuclear matter [88].

Including three-body forces and with parameters fit only to systems with up to four nucleons, chiral EFT provides remarkably good results when applied to medium-mass nuclei [89–95] and beyond [96]. In addition, chiral EFT can be applied to other quantities of interest, for example, to give constraints on neutron star equations of state [97–99], as well as to calculate infinite-matter properties [88, 100–102], interactions in dark-matter detectors [103–105], weak-charge observables [106], and two neutrons in a box [107].

A lot of current results are based on chiral interactions which are more than ten years old, for example those of Entem and Machleidt [108]. At the same time, there are many recent developments in chiral EFT: Three-body potentials at N^{3}LO are becoming available [100, 102, 109, 110] and in the two-body sector, N^{4}LO and even N^{5}LO diagrams are calculated [111–115]. New regularization techniques reduce cutoff artefacts [116] while local chiral interactions [117–119] can be used in Quantum Monte-Carlo (QMC) calculations [120]. New fits of the chiral interactions based on systematic approaches are available [121, 122]. Systematic understanding and quantification of the uncertainty of chiral results is underway, allowing theoretical calculations with informed systematic uncertainty estimates [123–126].

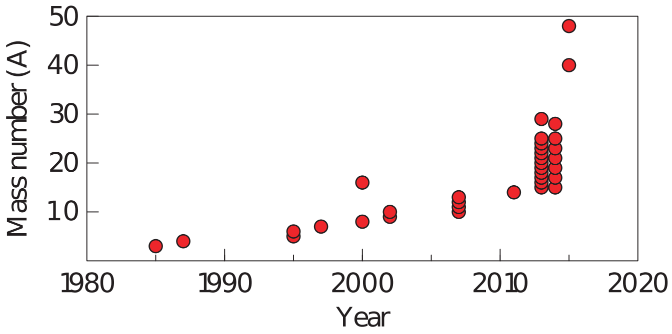

Figure 3.5: Historical reach of realistic ab-initio calculations in terms of the mass number A. From [106].

The reach of ab-initio calculations like those based on chiral EFT has grown rapidly in the last few years (Figure 3.5) thanks to new and improved many-body methods. With traditional methods the computational cost scales exponentially with increasing mass number, and so did the available computing power according to Moore's law. Recent methods exhibit polynomial scaling and thus strongly increase the reach.

Chiral nucleon-nucleon potentials up to $\mathrm{N^3LO}$ are used throughout this thesis to calculate neutrino-matter interaction rates. In Section 4.5, we include three-nucleon interactions at $\mathrm{N^2LO}$ and $\mathrm{N^3LO}$ using the normal-ordering formalism (cf. Section 3.6).

Extensive introductions to chiral EFT can be found for example in Refs. [85, 127–130].

3.4 T-Matrix Based on Phase Shifts

In addition to the potentials from chiral EFT, we use a potential that directly takes NN phase shifts into account. These can be extracted from experiment, see Ref. [131] for an example.

It is common to use the spectroscopic notation ${}^{2S+1}\text{“}l\text{”}_J$, where “$l$” is a letter encoding the angular momentum, see Table 3.2. The partial wave with spin $S=1$, orbital angular momentum $l=0$ and total orbital momentum $J=1$ is hence called ${}^3\mathrm{S}_1$, the partial wave with $S=0, l=2$, and $J=2$ is called ${}^1\mathrm{D}_2$, and so on.

l	0	1	2	3	4	5	6	…
“l”	S	P	D	F	G	H	I	…

Table 3.2: Letters encoding the angular momentum in spectroscopic notation.

The T-matrix is the sum of all ladder diagrams. One can calculate the T-matrix iteratively by solving the Lippmann-Schwinger equation,

$$T^+(\boldsymbol{k}',\boldsymbol{k};E) = V(\boldsymbol{k}',\boldsymbol{k}) + \int \frac{\mathrm{d}^3p}{(2\pi)^3} \frac{V(\boldsymbol{k}',\boldsymbol{p})\,T^+(\boldsymbol{p},\boldsymbol{k};E)}{E-\frac{p^2}{\mu}+i\varepsilon}\,, \tag{3.14}$$

with reduced mass μ and momenta $\boldsymbol{k}, \boldsymbol{k}'$, and $\boldsymbol{p}$. The first iteration gives $T=V$, which is called the Born approximation.

The partial-wave on-shell expression (which we will use in this thesis) is given in terms of the phase shifts δ_{lSJ} as

$$T_{lSJ}(\boldsymbol{k},\boldsymbol{k};E=k^2/\mu) = -\frac{2\pi}{\mu}\frac{\exp(2i\delta_{lSJ})-1}{2ik}\,. \tag{3.15}$$

This, however, is only true in so-called uncoupled channels. Since the nuclear interaction conserves spin, total angular momentum, and parity (which goes like $(-1)^l$) but not orbital angular momentum l, it can couple partial waves with the same spin and total angular momentum but a difference of 2 in the orbital angular momentum: ${}^3\mathrm{S}$–D_1, ${}^3\mathrm{P}$–F_2, … In these coupled channels,

$$T_{ll'SJ}(\boldsymbol{k},\boldsymbol{k};E=k^2/\mu) = -\frac{2\pi}{\mu}\frac{1}{2ik}\times\begin{cases}[\exp(2i\delta_{lSJ})\cos 2\epsilon_J - 1] & \text{for } l=l'\,,\\ [i\exp(i(\delta_{lSJ}+\delta_{l'SJ}))\sin 2\epsilon_J - 1] & \text{for } l\neq l'\,.\end{cases} \tag{3.16}$$

Here, ϵ_J is the mixing angle for given total angular momentum J and the bar-phase-shift parametrization is used. In this work, we use the phase shifts and mixing angles extracted from experiment by the Nijmegen group [131].

The use of a T-matrix as an alternative to nuclear potentials in our calculations of neutrino rates can be motivated by the relatively low-density, high-temperature conditions compared to nuclear structure calculations, under which nuclear interactions can effectively be described as two-body scattering.

As first shown by Schwinger, the cotangent of the S-wave phase shift δ_0 can be expanded in terms of the momentum k, with the leading-order term given by the scattering length a:

$$k\cot\delta_0(k) = -\frac{1}{a} + \frac{1}{2}r_e k^2 + \mathcal{O}(k^4)\,. \tag{3.17}$$

Here, r_e is the effective range. The natural case is a small scattering length $|ak| \ll 1$. A large scattering length hints at a nearly bound state (if $a<0$) or a weakly bound state (if $a>0$). In nuclear physics, S-wave scattering lengths are large. The ${}^1\mathrm{S}_0$ neutron-proton scattering length is $-23.7\,\mathrm{fm}$ and the ${}^3\mathrm{S}_1$ scattering length is $+5.4\,\mathrm{fm}$ with the deuteron being the weakly bound state.

Most nuclear structure calculations are limited by the size of the model space that can be used. Fast convergence is therefore desired. To achieve this goal, it is helpful if high-energy states do not have to be included in the calculation. The idea behind renormalization is similar to that of effective theories: If a system is probed at sufficiently low energies, the high-energy/short-distance structure of the theory can be simplified while low-energy observables stay the same.

The left panels of Figure 3.6 show (almost) unevolved chiral potentials in momentum representation. Green means no coupling between momenta k and k'. The most straight-forward approach would be to just set all matrix elements with k, k' larger than a certain cutoff to 0. One would naively expect this to fail at energies close to the cutoff, but it fails even at much lower energies, see Figure 3.7. The reason for this are intermediate states of the form

$$\sum_{k'} \frac{\langle k|V|k'\rangle \langle k'|V|k\rangle}{(k^2 - k'^2)} \tag{3.18}$$

that couple low- and high-energy states even for low-energy observables.

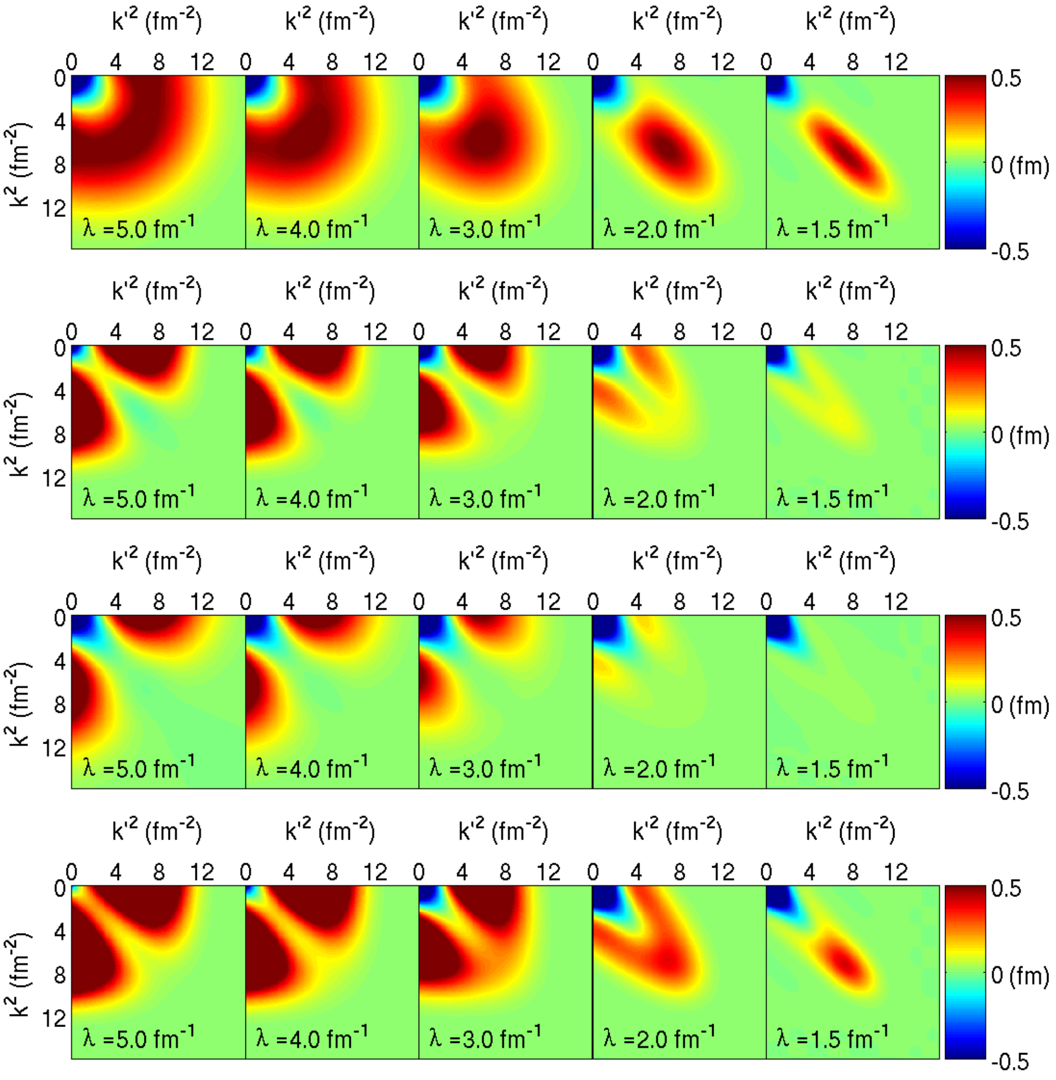

Figure 3.6: SRG evolution of two chiral EFT potentials in the $^1S_0$ (top two panels) and $^3S_1$ (bottom two panels) partial wave. From [132] based on [133].

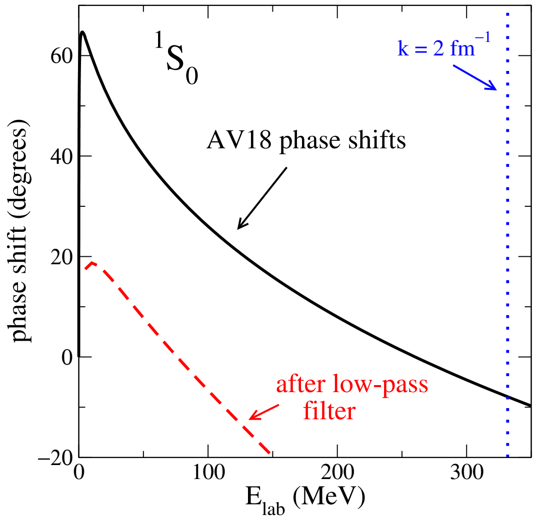

Figure 3.7: Applying a low-pass filter (i.e., setting all matrix elements with $k, k' > 2\,\mathrm{fm}^{-1}$ to 0) to the phenomenological Argonne v_{18} potential. The original $^1S_0$ phase shift (black) gets modified at all energies (red), even well below the energy scale of the cutoff (blue). From [132].

Instead of a simple cutoff, the renormalization group (RG) approach employs a unitary transformation of the Hamiltonian that decouples low and high energies. This is known as "flow equations" or "similarity renormalization group" (SRG) and was developed in parallel by Wegner [134–136] and by Glazek and Wilson [137]. By either creating a block-diagonal structure or a band structure (shown in Figure 3.6), the decoupling is realized. Note how at the same time the low-energy part of the two different interactions becomes more similar.

Formally, the SRG flow equations transform the initial Hamiltonian $H = T + V$ in a series of steps that are labeled by the flow parameter s (which is related to the resolution scale $\lambda = s^{-1/4}$):

$$H_s = U_s H U_s^\dagger \,, \tag{3.19}$$

with a unitary matrix U_s (i. e., $U_s^\dagger U_s = U_s U_s^\dagger = \mathbb{1}$).

Taking the derivative with respect to s and appropriately inserting $\mathbb{1}$,

$$\frac{\mathrm{d}H_s}{\mathrm{d}s} = \frac{\mathrm{d}U_s}{\mathrm{d}s} U_s^\dagger U_s H U_s^\dagger + U_s H U_s^\dagger U_s \frac{\mathrm{d}U_s^\dagger}{\mathrm{d}s} = [\eta_s, H_s] \,, \tag{3.20}$$

with the anti-Hermitian generator

$$\eta_s \equiv \frac{\mathrm{d}U_s}{\mathrm{d}s} U_s^\dagger = -\eta_s^\dagger \,. \tag{3.21}$$

It can be expressed in terms of the commutator

$$\eta_s = [G_s, H_s] \,, \tag{3.22}$$

where G_s is a Hermitian operator. A typical generator G_s used in SRG calculations is the relative kinetic energy T_{rel}. The final flow equation (T is taken to be fixed, only the potential is evolved) is then

$$\frac{\mathrm{d}H_s}{\mathrm{d}s} = \frac{\mathrm{d}V_s}{\mathrm{d}s} = \big[[G_s, H_s], H_s\big] \,. \tag{3.23}$$

The SRG evolution greatly enhances the convergence with the basis size, making computations faster and more feasible (Figure 3.8). However, the converged results now depend on the value of λ, see Fig. 3.8. Since λ has no physical meaning, any observables should be independent of this parameter. Induced many-body forces provide the solution to this puzzle. Even if the initial H in Eq. (3.23) only includes two-body terms, the commutators will

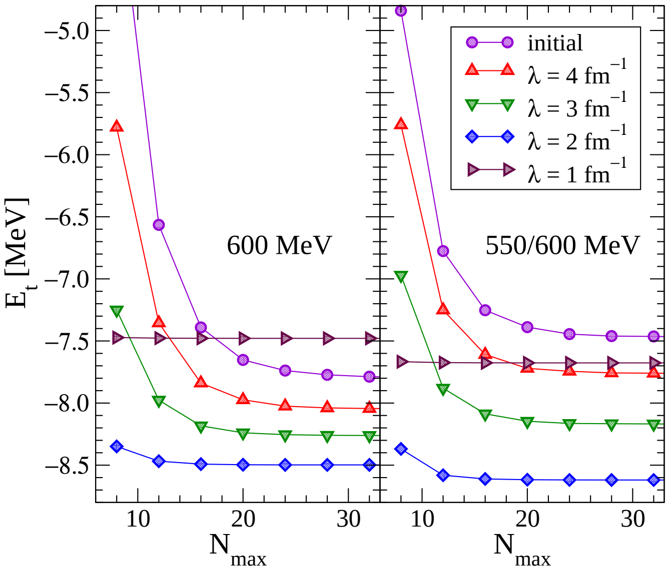

Figure 3.8: Convergence of triton ground-state energies for different SRG parameter values λ and for two different chiral NN potentials. From [132].

induce many-body forces and in particular three-body forces. If all induced forces are included in the calculation, the λ dependence will vanish. To calculate observables other than the energy, the operator ought to be evolved as well.

A more thorough introduction to SRG in nuclear physics (on which this section is based) can be found in Ref. [132]. The SRG approach has been applied in numerous nuclear structure and nuclear matter calculations, e. g., Refs. [88, 93, 96, 99, 102, 133, 138].

3.6 Three-Body Forces and Normal-Ordering

If one writes down the Hamiltonian of a system with two- and three-body interactions in terms of creation and annihilation operators (in so-called second quantization),

$$H = \sum_{12} T_{12} a_1^\dagger a_2 + \frac{1}{(2!)^2} \sum_{1234} \langle 12|V_{NN}|34\rangle a_1^\dagger a_2^\dagger a_4 a_3 + \frac{1}{(3!)^2} \sum_{123456} \langle 123|V_{3N}|456\rangle a_1^\dagger a_2^\dagger a_3^\dagger a_6 a_5 a_4 \,, \tag{3.24}$$

using Wick's theorem this can be written exactly as

$$H = E_0 + \sum_{12} f_{12} \{a_1^\dagger a_2\} + \frac{1}{(2!)^2} \sum_{1234} \langle 12|\Gamma|34\rangle \{a_1^\dagger a_2^\dagger a_4 a_3\} + \frac{1}{(3!)^2} \sum_{123456} \langle 123|\Gamma^{(3)}|456\rangle \{a_1^\dagger a_2^\dagger a_3^\dagger a_6 a_5 a_4\} \,. \tag{3.25}$$

Here, the curly brackets denote normal-ordering with respect to the reference state $|\Phi\rangle$, i. e., the normal-ordered creation and annihilation operators obey $\langle\Phi|\{a_1^\dagger \cdots a_n\}|\Phi\rangle = 0$.

The zero-body E_0, one-body f_{12}, and two-body $\langle 12|\Gamma|34\rangle$ parts all include contributions from the three-body interaction V_{3N}. Explicitly, the two-body part is given by

$$\langle 12|\Gamma|34\rangle = \langle 12|V_{NN}|34\rangle + \sum_i \langle 12i|V_{3N}|34i\rangle n_i = \langle 12|V_{NN}|34\rangle + \langle 12|\overline{V}^{as}_{3N}|34\rangle \,. \tag{3.26}$$

Normal-ordering hence allows to approximately treat three-nucleon interactions in a framework that only handles two-body forces. A density-dependent two-nucleon interaction $\overline{V}_{3N}$ can be constructed from the chiral three-nucleon potential V_{3N} by summing the third nucleon over occupied states of the non-interacting system [102, 139, 140],

$$\overline{V}^{as}_{3N} = \mathrm{Tr}_{\sigma_3} \mathrm{Tr}_{\tau_3} \int \frac{\mathrm{d}\boldsymbol{k}_3}{(2\pi)^3} n^{\tau_3}_{\boldsymbol{k}_3} \mathcal{A}_{123} V_{3N} \,. \tag{3.27}$$

Here, $n_{\boldsymbol{k}_3}^{\tau_3}$ is the momentum distribution of particle 3 with spin (isospin) projection σ_3 (τ_3). In infinite degenerate matter, this would be a Heaviside step function $n_{\boldsymbol{k}_3}^{\tau_3} = \Theta(k_\mathrm{F} - |\boldsymbol{k}_3|)$, in infinite non-degenerate matter, a Fermi-Dirac distribution function is used instead.

In a diagrammatic representation this treatment corresponds to an antisymmetrized three-nucleon force with one incoming and one outgoing line connected (see Figure 3.9). Instead of a three-body force, one can now use an effective two-body force. Unlike the original three-body force, this effective force depends on the thermodynamic quantities, i. e., density, temperature, and proton or electron fraction. While the first calculations were done in operator basis, the formalism to derive such a normal-ordered potential from partial-wave matrix elements has been developed recently [102], allowing to include N^{3}LO 3N interactions.

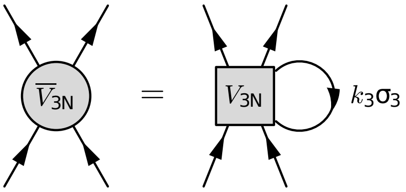

Figure 3.9: Diagrammatic representation of Eq. (3.27). From [140].

Due to its construction, $\overline{V}_{3N}$ does not include the full three-body interaction strength and we neglect the last term of the Hamiltonian in Eq. (3.25), but the normal-ordered two-body part is expected to dominate based on phase space arguments for normal Fermi systems [141]. This was investigated recently [142]. Most of the induced forces are therefore captured in the two-body formalism. In calculations that include three-body forces, we will use the total two-body potential according to Eq. (3.26).

Normal-ordering is a well-established method both in nuclei [96, 138, 139] and in infinite nuclear matter [88, 100, 101, 140]. An introduction to normal-ordering can be found, e. g., in Ref. [133].

One way to reduce the impact of induced many-body forces found in the previous section is in-medium SRG (IM-SRG) [143, 144], which applies the flow equations using a reference state that is not the vacuum. It uses normal-ordering with respect to this non-vacuum reference state and consequently captures most of the induced three-body forces in a two-body calculation.

4 Neutral-Current Interaction Rates and Pair-Absorption Opacities

Neutral-current neutrino-nucleon interactions were already introduced in Section 2.2. A structure factor describing bremsstrahlung and pair absorption has been derived by Hannestad and Raffelt (HR) in 1998 [51]. They treated all nucleons as neutrons, neglected correlations and nuclear recoil, and used the one-pion-exchange potential for the nuclear interaction. They provided analytical fit functions valid for arbitrary degeneracy that are currently used in most supernova simulations (e. g., Refs. [42–45, 62, 63, 145]).

In degenerate neutron matter, neutrino processes with more realistic nuclear interactions, including chiral EFT potentials, have been studied subsequently [47, 146–148]. The formalism was generalized to non-degenerate neutron matter in Ref. [57]. There, the non-degenerate formalism was also shown to be a good approximation in partially-degenerate matter, i. e., at temperatures well below the Fermi temperature.

In this chapter, we build on this work by generalizing the formalism to non-degenerate mixtures of protons and neutrons. Sections 4.1 to 4.3 follow our discussion in Ref. [149]. We derive equations for the relaxation rate, provide analytical expressions for the OPE case, perform a partial-wave expansion and use the result to compare OPE to modern nuclear interactions. In addition, we evaluate the impact of three-body forces and calculate the mean-free path for pair-absorption (the inverse of the bremsstrahlung process). Some results for proton-neutron bremsstrahlung have been discussed before in Refs. [50, 150, 151].

The axial coupling is spin dependent at low energies, while the vector coupling is spin independent. For our further discussion we will neglect the vector term in Eq. (2.26) and focus on the axial structure factor. The energy transfer in vector interactions vanishes as the momentum transfer goes to zero due to vector-current conservation. Hence, the vector response is suppressed. The axial current, on the other hand, is not a conserved quantity [57]. In addition, the weak charge for protons is small, so neutron-proton mixture effects are far more dominant in the axial part.

4.1 Structure Factor for Mixtures of Protons and Neutrons

The axial structure factor for a one-component system is defined by [152]

$$S_A(\omega,\boldsymbol{q}) \equiv \frac{C_A^2}{2\pi n V}\int\limits_{-\infty}^{\infty} \mathrm{d}t\, e^{i\omega t}\,\langle \sigma(\boldsymbol{q},t)\sigma(-\boldsymbol{q},0)\rangle \ . \tag{4.1}$$

Here, n is the particle density, V the normalization volume, $\langle\ \rangle$ the statistical average and $\sigma(\boldsymbol{q},t)$ are the Fourier components of the spin-density operator.

The nucleon-nucleon interaction effects on neutrino rates can be discussed by considering the scattering of neutrinos from fluctuations in the system. In the case of axial currents, these are spin fluctuations. Using the fluctuation-dissipation theorem, one can express the spin structure factor S_A in terms of the axial charge-density correlation function χ_A as [152]

$$S_A(\omega,\boldsymbol{q}) = \frac{1}{\pi n}\frac{1}{1-e^{-\omega/T}}\mathrm{Im}\chi_A(\omega,\boldsymbol{q}) \ . \tag{4.2}$$

Here, T is the temperature and n is the total density of nucleons.

Together with Chris Pethick and Achim Schwenk, we have derived the structure factor for mixtures of protons and neutrons [149]. We neglect mean-field (Fermi-liquid-type) effects which are thought to be small for neutral currents at subnuclear densities. We work in the long-wavelength limit ($\boldsymbol{q} \to 0$), neglecting recoil. This limit was shown to be a good approximation for bremsstrahlung processes as typical neutrino momenta are small compared to representative nucleon momenta, but see also Chapter 6.

At zero frequency, χ_A is given by [153]

$$\chi_A^0 = \sum_{i=n,p} \sum_{1} (C_A^i \sigma_1)^2 \left(-\frac{\partial n_1^i}{\partial \epsilon_1^i} \right) , \tag{4.3}$$

with shorthand notation $1 \equiv (\boldsymbol{p}_1, \sigma_1)$ for momentum and spin, quasiparticle distribution function n_1^i and quasiparticle energy ϵ_1^i for species $i = n, p$. Following Refs. [46, 51, 150], we calculate the response at frequencies high compared with a typical collision frequency and then extend the results to low frequencies by assuming that the response function has the standard (Debye) form for a simple relaxation process.

Generalizing the formalism of Ref. [57] to mixtures of neutrons and protons, the only difference compared with the result for pure neutrons is that the particles can be either neutrons or protons. For $q = 0$, we find

$$\chi_A \approx \frac{\mathrm{i}}{\omega} \frac{\chi_A^0}{\tau_A} \tag{4.4}$$

and define

$$\tau_A^{-1} \equiv \frac{1}{\chi_A^0} \Upsilon_A \quad \text{with} \quad \Upsilon_A = \Upsilon_A^{nn} + \Upsilon_A^{pp} + 2\Upsilon_A^{np} , \tag{4.5}$$

where the superscripts indicate the nucleons involved in the process. This is the high-frequency limit. To interpolate between low and high frequencies, one can use

$$\chi_A = \frac{\chi_A^0}{1 - \mathrm{i}\omega\tau_A} . \tag{4.6}$$

Following Ref. [57], Υ_A^{ij} is given by

$$\begin{aligned} \Upsilon_A^{ij} = \frac{1}{1+\delta_{ij}} \frac{(2\pi)^4}{4\omega} \sum_{1234} \delta_\epsilon^+ \delta_{\boldsymbol{p}} \left| \langle 34 | \mathcal{T}^{ij} | 12 \rangle \right|^2 \left[n_1^i n_2^j (1-n_3^i)(1-n_4^j) - n_3^i n_4^j (1-n_1^i)(1-n_2^j) \right] \\ \times (C_A^i \sigma_1 + C_A^j \sigma_2 - C_A^i \sigma_3 - C_A^j \sigma_4)^2 , \end{aligned} \tag{4.7}$$

where $\delta_\epsilon^+ \equiv \delta(\omega + \epsilon_1^i + \epsilon_2^j - \epsilon_3^i - \epsilon_4^j)$ and $\delta_{\boldsymbol{p}} \equiv \delta^{(3)}(\boldsymbol{p}_1 + \boldsymbol{p}_2 - \boldsymbol{p}_3 - \boldsymbol{p}_4)$ are energy and momentum conserving delta functions[1] and we use the short-hand notation

$$\sum_\lambda \equiv \int \frac{\mathrm{d}^3 p_\lambda}{(2\pi)^3} \sum_{\sigma_\lambda} . \tag{4.8}$$

Our scattering amplitudes $\mathcal{T}^{ij}$ include exchange contributions, and the factor of $1/(1+\delta_{ij})$ in Eq. (4.7) is necessary to avoid double-counting of final states for collisions between particles of the same species. We can then write

$$\begin{aligned} \Upsilon_A^{ij} = \frac{(2\pi)^4}{2\,\omega} \sum_{1234} \delta_\epsilon^+ \delta_{\boldsymbol{p}} \left| \langle 34 | \mathcal{T}^{ij} | 12 \rangle \right|^2 \left[n_1^i n_2^j (1-n_3^i)(1-n_4^j) - n_3^i n_4^j (1-n_1^i)(1-n_2^j) \right] \\ \times \begin{cases} C_A^{i\,2} \sigma_1 (\sigma_1 + \sigma_2 - \sigma_3 - \sigma_4) & \text{for } i = j , \\ C_A^{i\,2} \sigma_1 (\sigma_1 - \sigma_3) + C_A^{j\,2} \sigma_2 (\sigma_2 - \sigma_4) + 2 C_A^i C_A^j \sigma_1 (\sigma_2 - \sigma_4) & \text{for } i \neq j . \end{cases} \end{aligned} \tag{4.9}$$

The two combinations of distribution functions just differ by a factor of $\exp(-\omega/T)$ [57]:

$$\frac{n_3^i n_4^j (1-n_1^i)(1-n_2^j)}{n_1^i n_2^j (1-n_3^i)(1-n_4^j)} = e^{x_1 + x_2 - x_3 - x_4} \overset{\delta_\epsilon^+}{=} e^{-\omega/T} , \tag{4.10}$$

---

[1] The additional factor $(2\pi)^3$ in Eq. (4.7) compared to Refs. [57, 149] arises because in these references a discrete Kronecker $\delta_{\boldsymbol{p}}$ was used whereas we use a three-dimensional Dirac delta function.

with the short-hand notation $x_\lambda = (\epsilon_\lambda - \mu_\lambda)/T$, the chemical potential μ_λ of the species of the particle with index λ, and $\frac{n_\lambda}{1-n_\lambda} = e^{-x_\lambda}$. Hence we can rewrite Eq. (4.9) as

$$\begin{aligned}\Upsilon_A^{ij} &= \frac{(2\pi)^4}{2\,\omega}(1-e^{-\omega/T})\sum_{1234}\delta_\epsilon^+\delta_{\boldsymbol{p}}\left|\left\langle 34\left|\mathcal{T}^{ij}\right|12\right\rangle\right|^2 n_1^i n_2^j(1-n_3^i)(1-n_4^j) \\ &\quad\times\begin{cases}{C_A^i}^2\sigma_1(\sigma_1+\sigma_2-\sigma_3-\sigma_4) & \text{for } i=j\,, \\ {C_A^i}^2\sigma_1(\sigma_1-\sigma_3)+{C_A^j}^2\sigma_2(\sigma_2-\sigma_4)+2C_A^iC_A^j\sigma_1(\sigma_2-\sigma_4) & \text{for } i\neq j\end{cases} \qquad (4.11)\\ &= \frac{(2\pi)^4\sinh\big(\omega/(2T)\big)}{\omega}\sum_{1234}\delta_\epsilon^+\delta_{\boldsymbol{p}}\left|\left\langle 34\left|\mathcal{T}^{ij}\right|12\right\rangle\right|^2\prod_{\lambda=1}^{4}\frac{1}{2\cosh[(\epsilon_\lambda-\mu_\lambda)/(2T)]} \\ &\quad\times\begin{cases}{C_A^i}^2\sigma_1(\sigma_1+\sigma_2-\sigma_3-\sigma_4) & \text{for } i=j\,, \\ {C_A^i}^2\sigma_1(\sigma_1-\sigma_3)+{C_A^j}^2\sigma_2(\sigma_2-\sigma_4)+2C_A^iC_A^j\sigma_1(\sigma_2-\sigma_4) & \text{for } i\neq j\,.\end{cases} \qquad (4.12)\end{aligned}$$

Here, we brought Eq. (4.11) into the more symmetric form of Eq. (4.12) by using

$$\begin{aligned}n_1n_2(1-n_3)(1-n_4) &= \frac{1}{e^{x_1}+1}\frac{1}{e^{x_2}+1}\frac{e^{x_3}}{e^{x_3}+1}\frac{e^{x_4}}{e^{x_4}+1} \qquad (4.13)\\ &= \frac{e^{-x_1/2}}{e^{-x_1/2}(e^{x_1}+1)}\frac{e^{-x_2/2}}{e^{-x_2/2}(e^{x_2}+1)}\frac{e^{-x_3/2}e^{x_3}}{e^{-x_3/2}(e^{x_3}+1)}\frac{e^{-x_4/2}e^{x_4}}{e^{-x_4/2}(e^{x_4}+1)} \qquad (4.14)\\ &= e^{-(x_1+x_2-x_3-x_4)/2}\prod_{\lambda=1}^{4}\frac{1}{2\cosh(x_\lambda/2)} \overset{\delta_\epsilon^+}{=} e^{\omega/(2T)}\prod_{\lambda=1}^{4}\frac{1}{2\cosh(x_\lambda/2)}\,. \qquad (4.15)\end{aligned}$$

It is helpful to separate the spin sums from the phase-space integration, hence we introduce the quantities

$$W^{ij} = \frac{1}{12}\sum_{\sigma_i}\langle 34|\mathcal{T}^{ij}|12\rangle^*\,\boldsymbol{\sigma}_1\begin{cases}{C_A^i}^2\big[\boldsymbol{\sigma}_1+\boldsymbol{\sigma}_2,\langle 34|\mathcal{T}^{ij}|12\rangle\big] & \text{for } i=j\,,\\ \Big(({C_A^i}^2+{C_A^j}^2)\big[\boldsymbol{\sigma}_1,\langle 34|\mathcal{T}^{ij}|12\rangle\big]+2\,C_A^iC_A^j\big[\boldsymbol{\sigma}_2,\langle 34|\mathcal{T}^{ij}|12\rangle\big]\Big) & \text{for } i\neq j\,.\end{cases} \qquad (4.16)$$

The W^{ij} are functions of P, p, p' and three angles specifying the orientation of the total momentum $\boldsymbol{P} = \boldsymbol{p}_1+\boldsymbol{p}_2 = \boldsymbol{p}_3+\boldsymbol{p}_4$ and the relative momenta $\boldsymbol{p} = (\boldsymbol{p}_1-\boldsymbol{p}_2)/2$ and $\boldsymbol{p}' = (\boldsymbol{p}_3-\boldsymbol{p}_4)/2$.

For the OPE or the leading-order chiral potential of Eq. (3.13), the spin traces can be calculated analytically [67]:

$$W_{\text{LO}}^{ii} = {C_A^i}^2\left(\frac{g_A}{2F_\pi}\right)^4\frac{4}{3}\left(\frac{k^4}{\left(k^2+m_\pi^2\right)^2}+\frac{k'^4}{\left(k'^2+m_\pi^2\right)^2}+\frac{k^2k'^2-3(k\cdot k')^2}{\left(k^2+m_\pi^2\right)\left(k'^2+m_\pi^2\right)}\right)\,, \qquad (4.17)$$

$$\begin{aligned}W_{\text{LO}}^{i\neq j} &= ({C_A^i}^2+{C_A^j}^2)\left[4C_T^2+\left(\frac{g_A}{2F_\pi}\right)^2C_T\left(\frac{8}{3}\frac{k^2}{k^2+m_\pi^2}-\frac{8}{3}\frac{k'^2}{k'^2+m_\pi^2}\right)\right.\\ &\quad\left.+\left(\frac{g_A}{2F_\pi}\right)^4\left(\frac{4}{3}\frac{k^4}{\left(k^2+m_\pi^2\right)^2}+4\frac{k'^4}{\left(k'^2+m_\pi^2\right)^2}-\frac{8}{3}\frac{k^2k'^2-2(k\cdot k')^2}{\left(k^2+m_\pi^2\right)\left(k'^2+m_\pi^2\right)}\right)\right]+2C_A^iC_A^j\left[-4C_T^2\right.\\ &\quad\left.-\left(\frac{g_A}{2F_\pi}\right)^2C_T\left(\frac{8}{3}\frac{k^2}{k^2+m_\pi^2}-\frac{8}{3}\frac{k'^2}{k'^2+m_\pi^2}\right)+\left(\frac{g_A}{2F_\pi}\right)^4\left(\frac{4}{3}\frac{k'^4}{\left(k'^2+m_\pi^2\right)^2}+\frac{8}{3}\frac{(k\cdot k')^2}{\left(k^2+m_\pi^2\right)\left(k'^2+m_\pi^2\right)}\right)\right]\,.\end{aligned} \qquad (4.18)$$

Here, $\boldsymbol{k} = \boldsymbol{p}_2-\boldsymbol{p}_4 = \boldsymbol{p}'-\boldsymbol{p}$ and $\boldsymbol{k}' = \boldsymbol{p}_2-\boldsymbol{p}_3 = -(\boldsymbol{p}+\boldsymbol{p}')$ are the momentum exchanges between the nucleons and the coupling constant C_S does not appear in the final result because it commutes with all spin structures. Setting $C_T = 0$ corresponds to an OPE-only calculation. The functional form agrees with the neutron-neutron and neutron-proton bremsstrahlung expressions of Refs. [50, 154].[2]

---

[2] For neutron-proton bremsstrahlung, the expression in Ref. [50] differs from ours by a factor of 2 in front of the mixed k, k' terms. This typo was pointed out in Ref. [154].

We replace the p_λ integrals by integrals in terms of $\boldsymbol{P}, \boldsymbol{P}', \boldsymbol{p}$, and $\boldsymbol{p}'$ and use $\delta_{\boldsymbol{p}}$ to perform the $\boldsymbol{P}' = \boldsymbol{p}_3 + \boldsymbol{p}_4$ integration trivially. Then, Υ_A^{ij} is given by

$$\Upsilon_A^{ij} = \frac{2\pi \sinh\big(\omega/(2T)\big)}{\omega} \int \frac{\mathrm{d}^3P}{(2\pi)^3} \int \frac{\mathrm{d}^3p}{(2\pi)^3} \int \frac{\mathrm{d}^3p'}{(2\pi)^3} \delta_\epsilon^+ 4W^{ij} \prod_{\lambda=1}^{4} \frac{1}{2\cosh[(\epsilon_\lambda - \mu_\lambda)/(2T)]} \,. \tag{4.19}$$

The energy-conserving delta function can be written as

$$\delta_\epsilon^+ = \delta\left(\frac{p^2}{2m_{ij}^*} - \frac{p'^2}{2m_{ij}^*} + \omega\right), \tag{4.20}$$

where $m_{ij}^* = m_i^* m_j^*/(m_i^* + m_j^*)$ is the reduced (effective) mass, and hence

$$\int_0^\infty \mathrm{d}p'\, p'^2\, \delta_\epsilon^+ = \int_0^\infty \mathrm{d}p'\, p'^2\, \delta\left(p' - \sqrt{p^2 + 2m_{ij}^*\omega}\right) \frac{m_{ij}^*}{p'} = m_{ij}^* \sqrt{p^2 + 2m_{ij}^*\omega} \,. \tag{4.21}$$

We can then use the fact that W only depends on three angles to finally write Eq. (4.19) as

$$\Upsilon_A^{ij} = \frac{m_{ij}^* \sinh\big(\omega/(2T)\big)}{8\pi^6\, \omega} \int_{-1}^{1} \mathrm{d}\cos\theta \int_{-1}^{1} \mathrm{d}\cos\theta' \int_0^{2\pi} \mathrm{d}\phi \int_0^\infty \mathrm{d}P\, P^2 \int_0^\infty \mathrm{d}p\, p^2 \sqrt{p^2 + 2m_{ij}^*\omega}\, W^{ij} \prod_{\lambda=1}^{4} \frac{1}{2\cosh[(\epsilon_\lambda - \mu_\lambda)/(2T)]} \,. \tag{4.22}$$

In the non-degenerate limit, the distribution functions n_λ^i are Maxwell-Boltzmann distributions and we can write Eq. (4.3) as

$$\chi_A^0 = \sum_{i=np} \int \frac{\mathrm{d}^3p_1}{(2\pi)^3} \sum_{\sigma_1} (C_A^i \sigma_1)^2\, n_1^i(\epsilon_1^i)\, \frac{1}{T} \tag{4.23}$$

$$= \sum_{i=np} C_A^{i\,2} \frac{n_i}{T} \,, \tag{4.24}$$

with proton and neutron densities $n_{p,n}$. Assuming a non-relativistic quasiparticle energy of the form $\epsilon_{\boldsymbol{p}}^i = \epsilon_0^i + p^2/(2m_i^*)$, we can use

$$\prod_{i=1}^{4} \frac{1}{2\cosh[(\epsilon_i - \mu)/(2T)]} \approx e^{-(\epsilon_1+\epsilon_2+\epsilon_3+\epsilon_4)/(2T)} e^{(\mu_i+\mu_j)/T} \tag{4.25}$$

$$= e^{-[P^2/(2(m_i^*+m_j^*))+p^2/(2m_{ij}^*)+\omega/2]/T} e^{(\mu_i+\mu_j-\epsilon_0^i-\epsilon_0^j)/T} \,. \tag{4.26}$$

If $\mathcal{T}^{ij}$ is independent of $\boldsymbol{P}$, the integrals over θ' and ϕ become trivial. The product of densities is given by

$$n_i n_j = \frac{1}{\pi^4} \int \mathrm{d}P\, P^2 \int \mathrm{d}p\, p^2\, e^{-[P^2/(2(m_i^*+m_j^*))+p^2/(2m_{ij}^*)-\mu_i-\mu_j+\epsilon_0^i+\epsilon_0^j]/T} \,, \tag{4.27}$$

so Υ_A^{ij} can be written as

$$\Upsilon_A^{ij} = \frac{n_i n_j\, m_{ij}^* \sinh\big(\omega/(2T)\big)}{\pi\, \omega} e^{-\omega/(2T)} \frac{\int \mathrm{d}p\, p^2\, e^{-p^2/(2m_{ij}^* T)} \int \mathrm{d}\cos\theta\, \sqrt{p^2 + 2m_{ij}^*\omega}\, W^{ij}}{\int \mathrm{d}p\, p^2\, e^{-p^2/(2m_{ij}^* T)} \int \mathrm{d}\cos\theta} \tag{4.28}$$

$$= \frac{n_i n_j \sinh\big(\omega/(2T)\big)}{\pi\, \omega \sqrt{2\pi m_{ij}^* T^3}} e^{-\omega/(2T)} \int_{p_{\min}}^{\infty} dp\, p^2\, e^{-p^2/(2m_{ij}^* T)} \int_{-1}^{1} d\cos\theta\, \sqrt{p^2 + 2m_{ij}^*\omega}\, W^{ij} \,, \tag{4.29}$$

where $p_{\min}$ is given by

$$p_{\min} = \begin{cases} 0 & \text{for } \omega \geq 0 \,, \\ \sqrt{2m_{ij}^*|\omega|} & \text{for } \omega < 0 \,. \end{cases} \tag{4.30}$$

So far, $\omega > 0$ was assumed for definiteness.

In addition, we can expand Υ_A^{ij} in partial waves, following the steps in Ref. [67]. We write the spin trace in Eq. (4.16) in terms of single-particle spin states and then couple spins:

$$W^{ij} = \frac{3\cdot 2^2}{12} \sum_{m_{s_1} m_{s_2} m_{s_3} m_{s_4}} \left\langle s_3 m_{s_3} s_4 m_{s_4} \left| \mathcal{T}^{ij} \right| s_1 m_{s_1} s_2 m_{s_2} \right\rangle \left\langle s_1 m_{s_1} s_2 m_{s_2} \left| \mathcal{T}^{ij} \right| s_3 m_{s_3} s_4 m_{s_4} \right\rangle \\ \times \begin{cases} C_A^{i\,2}\, m_{s_1} (m_{s_1} + m_{s_2} - m_{s_3} - m_{s_4}) & \text{for } i = j\,, \\ C_A^{i\,2}\, m_{s_1} (m_{s_1} - m_{s_3}) + C_A^{j\,2}\, m_{s_2} (m_{s_2} - m_{s_4}) + 2 C_A^i C_A^j\, m_{s_1} (m_{s_2} - m_{s_4}) & \text{for } i \neq j \end{cases} \tag{4.31}$$

$$= \sum_{SS'M_S M_S'} \sum_{\tilde{S}\tilde{S}'\tilde{M}_S \tilde{M}_S'} \sum_{m_{s_1} m_{s_2} m_{s_3} m_{s_4}} C^{SM_S}_{s_1 m_{s_1} s_2 m_{s_2}} C^{S'M_S'}_{s_3 m_{s_3} s_4 m_{s_4}} C^{\tilde{S}\tilde{M}_S}_{s_1 m_{s_1} s_2 m_{s_2}} C^{\tilde{S}'\tilde{M}_S'}_{s_3 m_{s_3} s_4 m_{s_4}} \\ \times \left\langle (34) S' M_S' \left| \mathcal{T}^{ij} \right| (12) S M_S \right\rangle \left\langle (12) \tilde{S} \tilde{M}_S \left| \mathcal{T}^{ij} \right| (34) \tilde{S}' \tilde{M}_S' \right\rangle \\ \times \begin{cases} C_A^{i\,2}\, m_{s_1} (m_{s_1} + m_{s_2} - m_{s_3} - m_{s_4}) & \text{for } i = j\,, \\ C_A^{i\,2}\, m_{s_1} (m_{s_1} - m_{s_3}) + C_A^{j\,2}\, m_{s_2} (m_{s_2} - m_{s_4}) + 2 C_A^i C_A^j\, m_{s_1} (m_{s_2} - m_{s_4}) & \text{for } i \neq j\,. \end{cases} \tag{4.32}$$

Here, $s_i = 1/2$ and the potential conserves total spin, hence $S = S'$ and $\tilde{S} = \tilde{S}'$. The product of Clebsch-Gordan coefficients C^{ef}_{abcd} is only non-zero if $M_S = \tilde{M}_S$ and $M_S' = \tilde{M}_S'$. The sum over m_{s_i} can then be evaluated analytically and we can rewrite Eq. (4.32) as

$$W^{ij} = \sum_{S\tilde{S}M_S M_S'} \left\langle (34) S M_S' \left| \mathcal{T}^{ij} \right| (12) S M_S \right\rangle \left\langle (12) \tilde{S} M_S \left| \mathcal{T}^{ij} \right| (34) \tilde{S} M_S' \right\rangle 2 M^{ij}\,, \tag{4.33}$$

with

$$M^{ij} = (-1)^{S+\tilde{S}} \begin{cases} C_A^{i\,2}\, M_S\, \Delta M_S & \text{for } i = j, \\ \frac{1}{8} (C_A^{i\,2} + C_A^{j\,2})(1 - M_S M_S') + \frac{1}{2} C_A^i C_A^j \left(M_S\, \Delta M_S - \frac{1}{2}(1 - M_S M_S') \right) & \text{for } i \neq j\,. \end{cases} \tag{4.34}$$

We can then follow the steps in Ref. [155] and use the expansion in spherical harmonics Y_{lm},

$$|\boldsymbol{p}\rangle = \sum_{lm} 4\pi i^l Y^*_{lm} \, |p\rangle \, |lm\rangle \ , \tag{4.35}$$

to write

$$\left\langle S M_S' \left| \mathcal{T}^{ij}_{pp'} \right| S M_S \right\rangle = \left\langle \boldsymbol{p}' S M_S' \left| \mathcal{T}^{ij} \right| \boldsymbol{p} S M_S \right\rangle \tag{4.36}$$

$$= (4\pi)^2 \sum_{ll'mm'} i^{l-l'} \left\langle p' \right| \left\langle l'm' \right| \underbrace{\left\langle S M_S' \right| \mathcal{T}^{ij} \left| S M_S \right\rangle}_{\mathbb{1} = \sum_{Jm_J} |Jm_J\rangle \langle Jm_J|} |lm\rangle \, |p\rangle \, Y_{l'm'}(\hat{\boldsymbol{p}}') Y^*_{lm}(\hat{\boldsymbol{p}}) \tag{4.37}$$

$$= (4\pi)^2 \sum_{ll'mm'Jm_J} i^{l-l'} C^{Jm_J}_{l'm'SM_S'} C^{Jm_J}_{lmSM_S} \left\langle p' \left| \mathcal{T}^{ij}_{l'lJS} \left(1 - (-1)^{l+S+T} \right) \right| p \right\rangle Y_{l'm'}(\hat{\boldsymbol{p}}') Y^*_{lm}(\hat{\boldsymbol{p}})\,. \tag{4.38}$$

The factor $\left(1 - (-1)^{l+S+T}\right)$ represents the direct and the exchange term assuming an antisymmetrized matrix element. We can make the isospin dependence of the matrix element explicit by using $\mathcal{T}^{ij}_{l'lJS} = \frac{1}{2}\left(\mathcal{T}^{ij,T=0}_{l'lJS} + \mathcal{T}^{ij,T=1}_{l'lJS} \right)$. Inserting this into Eq. (4.33) yields

$$W^{ij} = \sum_{S\tilde{S}M_S M_S'} \sum_{T\tilde{T}} \sum_{ll'mm'Jm_J} \sum_{\tilde{l}\tilde{l}'\tilde{m}\tilde{m}'\tilde{J}\tilde{m}_J} \frac{1}{2} \left(1 - (-1)^{l+S+T} \right) \left(1 - (-1)^{\tilde{l}+\tilde{S}+\tilde{T}} \right) i^{l'-l+\tilde{l}-\tilde{l}'} M^{ij} \\ \times (4\pi)^4 C^{Jm_J}_{l'm'SM_S'} C^{Jm_J}_{lmSM_S} C^{\tilde{J}\tilde{m}_J}_{\tilde{l}'\tilde{m}'\tilde{S}M_S'} C^{\tilde{J}\tilde{m}_J}_{\tilde{l}\tilde{m}\tilde{S}M_S} \left\langle p \left| \mathcal{T}^{ij,T}_{l'lJS} \right| p' \right\rangle \left\langle p' \left| \mathcal{T}^{ij,\tilde{T}}_{\tilde{l}\tilde{l}'\tilde{J}\tilde{S}} \right| p \right\rangle Y^*_{l'm'}(\hat{\boldsymbol{p}}') Y_{lm}(\hat{\boldsymbol{p}}) Y_{\tilde{l}'\tilde{m}'}(\hat{\boldsymbol{p}}') Y^*_{\tilde{l}\tilde{m}}(\hat{\boldsymbol{p}})\,, \tag{4.39}$$

where we assume the matrix elements to be real. When using the T-matrix formalism, the first matrix element needs to be complex conjugated.

The spherical harmonics are irreducible tensors and can be coupled into one object [156],

$$\begin{aligned} &Y^*_{l'm'}(\hat{\boldsymbol{p}}')Y_{lm}(\hat{\boldsymbol{p}})Y_{\tilde{l}'\tilde{m}'}(\hat{\boldsymbol{p}}')Y^*_{\tilde{l}\tilde{m}}(\hat{\boldsymbol{p}}) \\ &\quad = (-1)^{m'+\tilde{m}} \sum_{LM\tilde{L}\tilde{M}HM_H} C^{LM}_{l'm'lm} C^{\tilde{L}\tilde{M}}_{\tilde{l}'\tilde{m}'\tilde{l}\tilde{m}} C^{HM_H}_{LM\tilde{L}\tilde{M}} \left\{ \left\{ Y_{l'}(\hat{\boldsymbol{p}}') \otimes Y_l(\hat{\boldsymbol{p}}) \right\}^L_M \otimes \left\{ Y_{\tilde{l}'}(\hat{\boldsymbol{p}}') \otimes Y_{\tilde{l}}(\hat{\boldsymbol{p}}) \right\}^{\tilde{L}}_{\tilde{M}} \right\}^H_{M_H} , \end{aligned} \tag{4.40}$$

where $\{X \otimes Y\}^L_M = \sum_{M_1 M_2} C^{LM}_{L_1 M_1 L_2 M_2} X_{L_1 M_1} Y_{L_2 M_2}$ is the M component of the irreducible tensor product. The left-hand side of this equation is scalar, therefore $H = M_H = 0$ and from the Clebsch-Gordan coefficients we obtain $\tilde{M} = -M$ and $\tilde{L} = L$.

We can further simplify the spherical harmonics:

$$\begin{aligned} &\left\{ \left\{ Y_{l'}(\hat{\boldsymbol{p}}') \otimes Y_l(\hat{\boldsymbol{p}}) \right\}^L_M \otimes \left\{ Y_{\tilde{l}'}(\hat{\boldsymbol{p}}') \otimes Y_{\tilde{l}}(\hat{\boldsymbol{p}}) \right\}^L_{-M} \right\}^0_0 \\ &\quad = \sum_{gh} \hat{L}^2 \begin{Bmatrix} l' & l & L \\ \tilde{l}' & \tilde{l} & L \\ g & h & 0 \end{Bmatrix} \left\{ \left\{ Y_{l'}(\hat{\boldsymbol{p}}') \otimes Y_{\tilde{l}'}(\hat{\boldsymbol{p}}') \right\}_g \otimes \left\{ Y_l(\hat{\boldsymbol{p}}) \otimes Y_{\tilde{l}}(\hat{\boldsymbol{p}}) \right\}_h \right\}^0_0 \qquad (4.41) \\ &\quad = \hat{L}^2 \sum_K \frac{(-1)^{l+L+\tilde{l}'+K}}{\hat{L}\hat{K}} \begin{Bmatrix} l' & l & L \\ \tilde{l} & \tilde{l}' & K \end{Bmatrix} (-1)^{l'+\tilde{l}'+l+\tilde{l}} \frac{\hat{l}'\hat{\tilde{l}}'\hat{l}\hat{\tilde{l}}}{4\pi} \begin{pmatrix} l' & \tilde{l}' & K \\ 0 & 0 & 0 \end{pmatrix} \begin{pmatrix} l & \tilde{l} & K \\ 0 & 0 & 0 \end{pmatrix} \left\{ Y_K(\hat{\boldsymbol{p}}') \otimes Y_K(\hat{\boldsymbol{p}}) \right\}^0_0 . \end{aligned} \tag{4.42}$$

Here, $\hat{a} \equiv \sqrt{2a+1}$ and we have used $g = h \equiv K$ in the last step. We use the standard notations for Wigner $3j$, $6j$, and $9j$ symbols, $\left(\begin{smallmatrix} a & b & c \\ d & e & f \end{smallmatrix}\right)$, $\left\{\begin{smallmatrix} a & b & c \\ d & e & f \end{smallmatrix}\right\}$, and $\left\{\begin{smallmatrix} a & b & c \\ d & e & f \\ g & h & i \end{smallmatrix}\right\}$, respectively. The coupled spherical harmonics in Eq. (4.42) can be transformed into a Legrende polynomial using

$$\left\{ Y_K(\hat{\boldsymbol{p}}') \otimes Y_K(\hat{\boldsymbol{p}}) \right\}^0_0 = (-1)^K \frac{1}{\hat{K}} Y_K(\hat{\boldsymbol{p}}') \cdot Y_K(\hat{\boldsymbol{p}}) = \frac{(-1)^K}{4\pi} P_K(\cos\theta) . \tag{4.43}$$

The Clebsch-Gordan coefficients can be combined and evaluated using relations from [156]:

$$\begin{aligned} \sum_{mm'm_J} C^{Jm_J}_{l'm'SM'_S} C^{Jm_J}_{lmSM_S} C^{LM}_{l'-m'lm} (-1)^{m'} &= \sum_{mm'm_J} C^{Jm_J}_{l'm'SM'_S} C^{Jm_J}_{lmSM_S} C^{LM}_{lml'-m'} (-1)^{m'+l+l'-L} \\ &= \sum_{mm'm_J} C^{Jm_J}_{l'm'SM'_S} C^{Jm_J}_{lmSM_S} C^{l'm'}_{lmL-M} (-1)^{m'+l+l'-L+l-m} \frac{\hat{L}}{\hat{l}'} \\ &= \frac{\hat{L}\hat{J}^2}{\hat{S}} (-1)^{3l+l'-M+J+S} C^{SM_S}_{L-MSM'_S} \begin{Bmatrix} l' & l & L \\ S & S & J \end{Bmatrix} , \qquad (4.44) \\ \sum_{\tilde{m}\tilde{m}'\tilde{m}_J} C^{\tilde{J}\tilde{m}_J}_{\tilde{l}'\tilde{m}'\tilde{S}M'_S} C^{\tilde{J}\tilde{m}_J}_{\tilde{l}\tilde{m}\tilde{S}M_S} C^{\tilde{L}\tilde{M}}_{\tilde{l}'\tilde{m}'\tilde{l}-\tilde{m}} (-1)^{\tilde{m}} &= \sum_{\tilde{m}\tilde{m}'\tilde{m}_J} C^{\tilde{J}\tilde{m}_J}_{\tilde{l}'\tilde{m}'\tilde{S}M'_S} C^{\tilde{J}\tilde{m}_J}_{\tilde{l}\tilde{m}\tilde{S}M_S} C^{\tilde{l}\tilde{m}}_{\tilde{l}'\tilde{m}'\tilde{L}-\tilde{M}} (-1)^{\tilde{m}+\tilde{l}'-\tilde{m}'} \frac{\hat{\tilde{L}}}{\hat{\tilde{l}}} \\ &= \frac{\hat{\tilde{L}}\hat{\tilde{J}}^2}{\hat{\tilde{S}}} (-1)^{2\tilde{l}'+L-\tilde{M}+\tilde{J}+\tilde{S}} C^{\tilde{S}M'_S}_{\tilde{L}-\tilde{M}\tilde{S}M_S} \begin{Bmatrix} \tilde{l} & \tilde{l}' & \tilde{L} \\ \tilde{S} & \tilde{S} & \tilde{J} \end{Bmatrix} , \qquad (4.45) \\ C^{00}_{LML-M} &= \frac{(-1)^{L+M}}{\hat{L}} , \text{ and} \qquad (4.46) \\ (-1)^{\tilde{M}} C^{\tilde{S}M_S}_{\tilde{L}-\tilde{M}\tilde{S}M'_S} = (-1)^{\tilde{M}} (-1)^{\tilde{L}+\tilde{M}} C^{\tilde{S}-M'_S}_{\tilde{L}-\tilde{M}\tilde{S}-M_S} &= (-1)^{2\tilde{L}} C^{\tilde{S}M'_S}_{\tilde{L}\tilde{M}\tilde{S}M_S} = C^{\tilde{S}M'_S}_{\tilde{L}\tilde{M}\tilde{S}M_S} , \qquad (4.47) \end{aligned}$$

where in the first equations $M = m - m'$ and $\tilde{M} = \tilde{m}' - \tilde{m}$ were identified from the Clebsch-Gordan coefficients, respectively.

The cosine integral in Eq. (4.29) can be done analytically as the only θ-dependence is the Legendre polynomial. Hence,

$$\int_{-1}^{1} \mathrm{d}\cos\theta \, P_K(\cos\theta) = 2\delta_{K0} \,. \tag{4.48}$$

Using the properties of the $3j$ symbols and the Clebsch-Gordan coefficients one concludes that $l = \tilde{l}$, $l' = \tilde{l}'$, and $M = M_S' - M_S \equiv -\Delta M_S$. Putting it all together,

$$\begin{aligned} \int_{-1}^{1} \mathrm{d}\cos\theta \, W^{ij} = \sum_{S\tilde{S}T\tilde{T}} \sum_{Ll l' J\tilde{J}} \sum_{M_S M_S'} 16\pi^2 (-1)^{L+J+\tilde{J}+S+\tilde{S}} \left(\hat{L}\hat{J}\hat{\tilde{J}}\right)^2 \frac{\hat{l}\hat{l}'}{\hat{S}\hat{\tilde{S}}} \begin{Bmatrix} l' & l & L \\ l & l' & 0 \end{Bmatrix} \begin{Bmatrix} l' & l & L \\ S & S & J \end{Bmatrix} \begin{Bmatrix} l & l' & L \\ \tilde{S} & \tilde{S} & \tilde{J} \end{Bmatrix} \\ \times \left(1-(-1)^{l+S+T}\right)\left(1-(-1)^{l+\tilde{S}+\tilde{T}}\right) \left\langle p \middle| \mathcal{T}^{ij,T}_{l'lJS} \middle| p' \right\rangle \left\langle p' \middle| \mathcal{T}^{ij,\tilde{T}}_{ll'\tilde{J}\tilde{S}} \middle| p \right\rangle C^{SM_S}_{L\Delta M_S S M_S'} C^{\tilde{S}M_S}_{L\Delta M_S \tilde{S} M_S'} M^{ij} \,. \end{aligned} \tag{4.49}$$

Inserting this expression into Eq. (4.29) finally yields

$$\begin{aligned} \Upsilon_A^{ij} =& 16\sqrt{\pi}\, n_i n_j \frac{\sinh\left(\omega/(2T)\right)}{\omega\sqrt{2m_{ij}^* T^3}} \int_{p_{\min}}^{\infty} \mathrm{d}p\, p^2 \sqrt{p^2 + 2m_{ij}^*\omega}\, e^{-p^2/(2m_{ij}^* T) - \omega/(2T)} \sum_{S\tilde{S}T\tilde{T}} \sum_{Ll l' J\tilde{J}} (-1)^{L+J+\tilde{J}} \left(\hat{L}\hat{J}\hat{\tilde{J}}\right)^2 \frac{\hat{l}\hat{l}'}{\hat{S}\hat{\tilde{S}}} \\ &\times \begin{Bmatrix} l' & l & L \\ l & l' & 0 \end{Bmatrix} \begin{Bmatrix} l' & l & L \\ S & S & J \end{Bmatrix} \begin{Bmatrix} l & l' & L \\ \tilde{S} & \tilde{S} & \tilde{J} \end{Bmatrix} \left(1-(-1)^{l+S+T}\right)\left(1-(-1)^{l+\tilde{S}+\tilde{T}}\right) \left\langle p \middle| \mathcal{T}^{ij,T}_{l'lJS} \middle| p' \right\rangle \left\langle p' \middle| \mathcal{T}^{ij,\tilde{T}}_{ll'\tilde{J}\tilde{S}} \middle| p \right\rangle \\ &\times \sum_{M_S M_S'} C^{SM_S}_{L\Delta M_S S M_S'} C^{\tilde{S}M_S}_{L\Delta M_S \tilde{S} M_S'} \begin{cases} C_A^{i\,2} M_S \, \Delta M_S & \text{for } i = j, \\ \frac{1}{8}(C_A^{i\,2} + C_A^{j\,2})(1 - M_S M_S') + \frac{1}{2} C_A^i C_A^j \left(M_S\, \Delta M_S - \frac{1}{2}(1 - M_S M_S')\right) & \text{for } i \neq j \,. \end{cases} \end{aligned} \tag{4.50}$$

The sums for $i = j$ collapse to $S = \tilde{S} = T = \tilde{T} = 1$.

The partial-wave expansion was checked by comparing the $Y_e = 0$ results to calculations in and based on Ref. [57] for the OPE, chiral and T-matrix potentials. We also used partial-wave-expanded OPE matrix elements (B.3) to check the partial-wave expansion at different Y_e against the analytical OPE calculations mentioned above.

One should note that for $\omega \neq 0$ the scattering amplitudes required to calculate the structure factor are generally off-shell ones, and therefore it is necessary to specify the energy and momenta at which the scattering amplitude is evaluated. This is particularly important at low energies because the interactions are resonant. From Eq. (4.20), we obtain $p' = \sqrt{p^2 + 2m_{ij}^*\omega}$. In this thesis, we will approximate the full result using scattering amplitudes evaluated at momenta that correspond to the mean of the initial and final state energies,

$$\left\langle p \middle| \mathcal{T}^{ij,T}_{l'lJS} \middle| p' \right\rangle \quad \longrightarrow \quad \left\langle \sqrt{p^2 + m_{ij}^*\omega} \middle| \mathcal{T}^{ij,T}_{l'lJS} \middle| \sqrt{p^2 + m_{ij}^*\omega} \right\rangle \equiv \left\langle \overline{p} \middle| \mathcal{T}^{ij,T}_{l'lJS} \middle| \overline{p} \right\rangle \,. \tag{4.51}$$

For the OPE potential, the analytical expression allows us to directly evaluate the quality of this approximation. The direct and exchange momentum transfers k and k' of Eqs. (4.17) and (4.18) as well as their scalar product are given by

$$k^2 = p^2 + p'^2 - 2pp'\cos\theta \,, \tag{4.52}$$

$$k'^2 = p^2 + p'^2 + 2pp'\cos\theta \,, \tag{4.53}$$

$$\boldsymbol{k} \cdot \boldsymbol{k}' = p^2 - p'^2 \,. \tag{4.54}$$

In the on-shell approximation, $p = p' = \overline{p}$ and thus

$$k^2 = 2(p^2 + m_{ij}^*\omega)(1 - \cos\theta) \,, \tag{4.55}$$

$$k'^2 = 2(p^2 + m_{ij}^*\omega)(1 + \cos\theta) \,, \tag{4.56}$$

$$\boldsymbol{k} \cdot \boldsymbol{k}' = 0 \,, \tag{4.57}$$

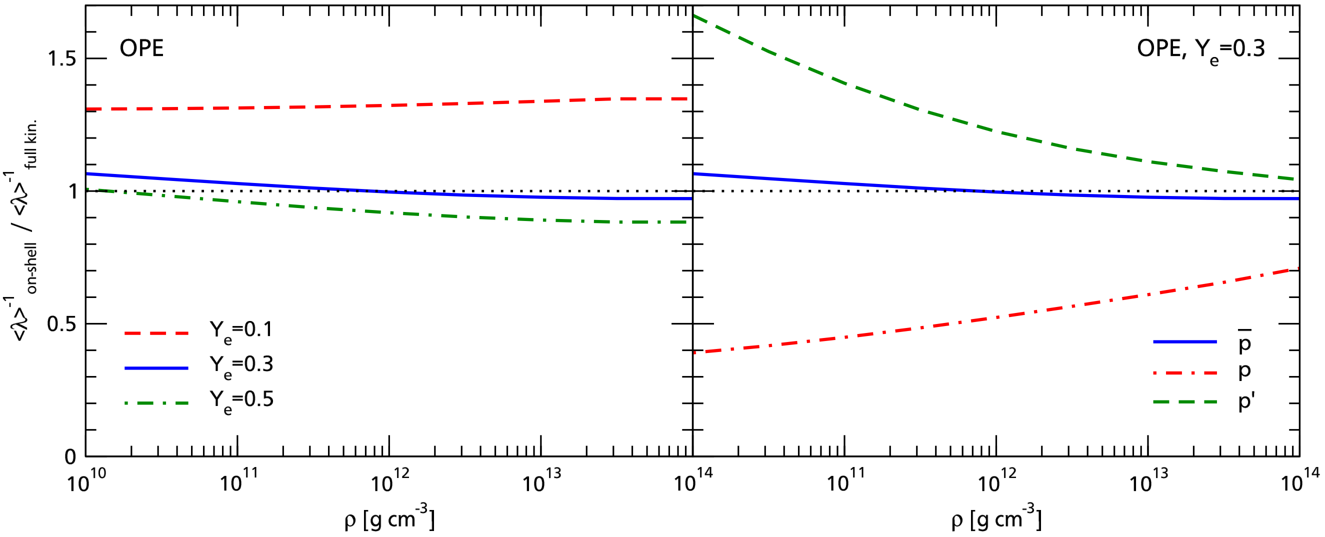

Figure 4.1: Left panel: Ratio of inverse mean-free paths based on the OPE potential calculated with and without the on-shell approximation as a function of density at $Y_e = 0.1$ (dashed red line), $Y_e = 0.3$ (solid blue line), and $Y_e = 0.5$ (green dash-dotted line). Right panel: Same, but at fixed $Y_e = 0.3$ and comparing calculations using $\langle \overline{p} \,|\mathcal{T}|\, \overline{p} \rangle$ (blue solid line), $\langle p \,|\mathcal{T}|\, p \rangle$ (red dash-dotted line), and $\langle p' \,|\mathcal{T}|\, p' \rangle$ (green dashed line) in the on-shell calculation.

while in full kinematics,

$$k^2 = 2p^2 + 2m_{ij}^*\omega - 2p\sqrt{p^2 + 2m_{ij}^*\omega}\cos\theta \,, \tag{4.58}$$

$$k'^2 = 2p^2 + 2m_{ij}^*\omega + 2p\sqrt{p^2 + 2m_{ij}^*\omega}\cos\theta \,, \tag{4.59}$$

$$\boldsymbol{k} \cdot \boldsymbol{k}' = -2m_{ij}^*\omega \,. \tag{4.60}$$

In Figure 4.1, we show the deviation of the on-shell from the full-kinematics result for the energy-averaged mean-free path (see Section 4.3). The on-shell approximation works especially well at $Y_e = 0.3$ and sufficiently well in symmetric nuclear matter. It works less well in strongly asymmetric nuclear matter, in contrast to findings in Ref. [57], where the $(\boldsymbol{k} \cdot \boldsymbol{k}')^2$ term in Eq. (4.17) was neglected. This has been checked against the partial-wave-expanded formalism using the analytical matrix element in Appendix B, which allows $p \neq p'$. Electron fractions at or below $Y_e = 0.1$ are mostly relevant for neutron star cooling, where matter becomes more and more degenerate and the $(\boldsymbol{k} \cdot \boldsymbol{k}')^2$ term goes to 0 also for the full-kinematics result [50].

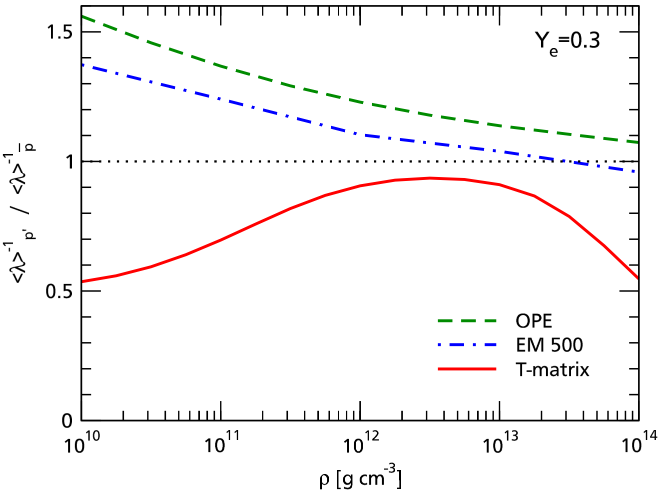

Figure 4.2: Ratio of inverse mean-free paths in the on-shell approximation at $Y_e = 0.3$ using p' and $\overline{p}$ for the OPE (green dashed line), EM 500 (blue dash-dotted line), and T-matrix (red solid line) interactions.

In the right panel of Figure 4.1, we compare results obtained using $\left\langle p \middle| \mathcal{T}^{ij,T}_{l'lJS} \middle| p \right\rangle$, $\left\langle p' \middle| \mathcal{T}^{ij,T}_{l'lJS} \middle| p' \right\rangle$, and $\left\langle \overline{p} \middle| \mathcal{T}^{ij,T}_{l'lJS} \middle| \overline{p} \right\rangle$ relative to the full-kinematics result. This clearly motivates the use of our mean-energy momentum $\overline{p}$ in the on-shell expression. In addition, using p' is a significantly better approximation than using p, which seems reasonable as using p neglects all ω dependence of the matrix elements.

For the chiral and T-matrix potentials, no analytical expression is available. In Figure 4.2, we instead plot the deviation using p' rather than $\overline{p}$ in the on-shell matrix elements. While this cannot be considered the uncertainty of the on-shell approximation, it shows that the T-matrix is especially sensitive to the on-shell treatment. Hence, going beyond the on-shell approximation will be an important next step.

In order to increase code performance, we use $M_T = 0$ matrix elements for all contributions, allowing us to combine the nn, np, and pp contributions in Eq. (4.50), cf. Fig. 4.13 and Appendix A.

4.2 Spin Relaxation Rate

In the following discussion of our results, we work in the long-wavelength limit, neglect effective mass effects, and use $m_n^* = m_p^* = 939\,\text{MeV}$. This should be a justified approximation since the densities of interest are relatively low compared to nuclear saturation density. In general, the axial couplings C_A^i are momentum dependent and there are contributions from two-body currents [67, 157] and strange quarks. We will keep them constant at $C_A^p = -C_A^n = g_A/2$, where $g_A = 1.26$ is the free weak charge.

We plot the spin relaxation rate $1/\tau_A$ at $\omega = 0$ as a function of density in Figure 4.3, varying the electron fraction Y_e from pure neutron matter (top left panel) to symmetric nuclear matter. We parametrize the temperature in terms of the density according to Eq. (2.44), see the discussion of typical conditions in Section 2.4.

4.2.1 Results in Born Approximation

The blue dashed line in Figure 4.3 is conceptually similar to the results of Hannestad and Raffelt (HR, Ref. [51]), i. e., we use the one-pion-exchange approximation and assume all protons interact like neutrons (OPE nn-only). We stress that these results are not identical to those obtained using the structure factor provided in Ref. [51], see discussion in Section 4.4. The black solid line adds the Y_e dependence while still using the one-pion-exchange (OPE) approximation. For OPE, the Y_e dependence is small and working in pure neutron matter is a good approximation. Next, we add the contact terms of the leading-order chiral potential (black dotted line) which do not enter the final result in pure neutron matter. In mixtures, the C_T term increases the rate at low densities.

Adding all two-body terms in the chiral potential up to N^{3}LO, we obtain the grey-orange band spanned by the chiral EM 500 MeV, EGM 450/500 MeV and EGM 450/700 MeV potentials [108, 158]. The Y_e dependence is weak and the rates are similar at low densities and about a factor of two smaller at high densities compared with the OPE results, confirming findings made in pure neutron matter [57]. Looking at the width of the chiral band and hence the uncertainty of the calculation, the band is wide at low densities (better visible in Fig. 4.4 which extends to lower densities). Here, momenta are low and the main contribution is the momentum-independent leading-order contact term (cf. Eq. (3.13)). As the coupling constant C_T differs between the potentials, this uncertainty translates to a wide band. With increasing density, better-constrained terms dominate and the band becomes narrow until its width grows again as the convergence of the chiral expansion worsens with increasing density (and hence increasing momenta).

Three-body forces will be included using the formalism of normal-ordering, see Section 4.5.

4.2.2 T-Matrix Results and Resonant Enhancement at Low Densities

All previously mentioned results were obtained at Born level. However, at low energies NN interactions are resonant. We use the T-matrix based on NN phase shifts as a model-independent input at low densities. This approach is similar to the virial expansion for energy contributions [159]. The red solid line shows the resulting $1/\tau_A$ based on the Nijmegen partial wave analysis [131]. In pure neutron matter, these results are very similar to the ones obtained with the chiral N^{3}LO potential. In proton-neutron mixtures, central interactions contribute and

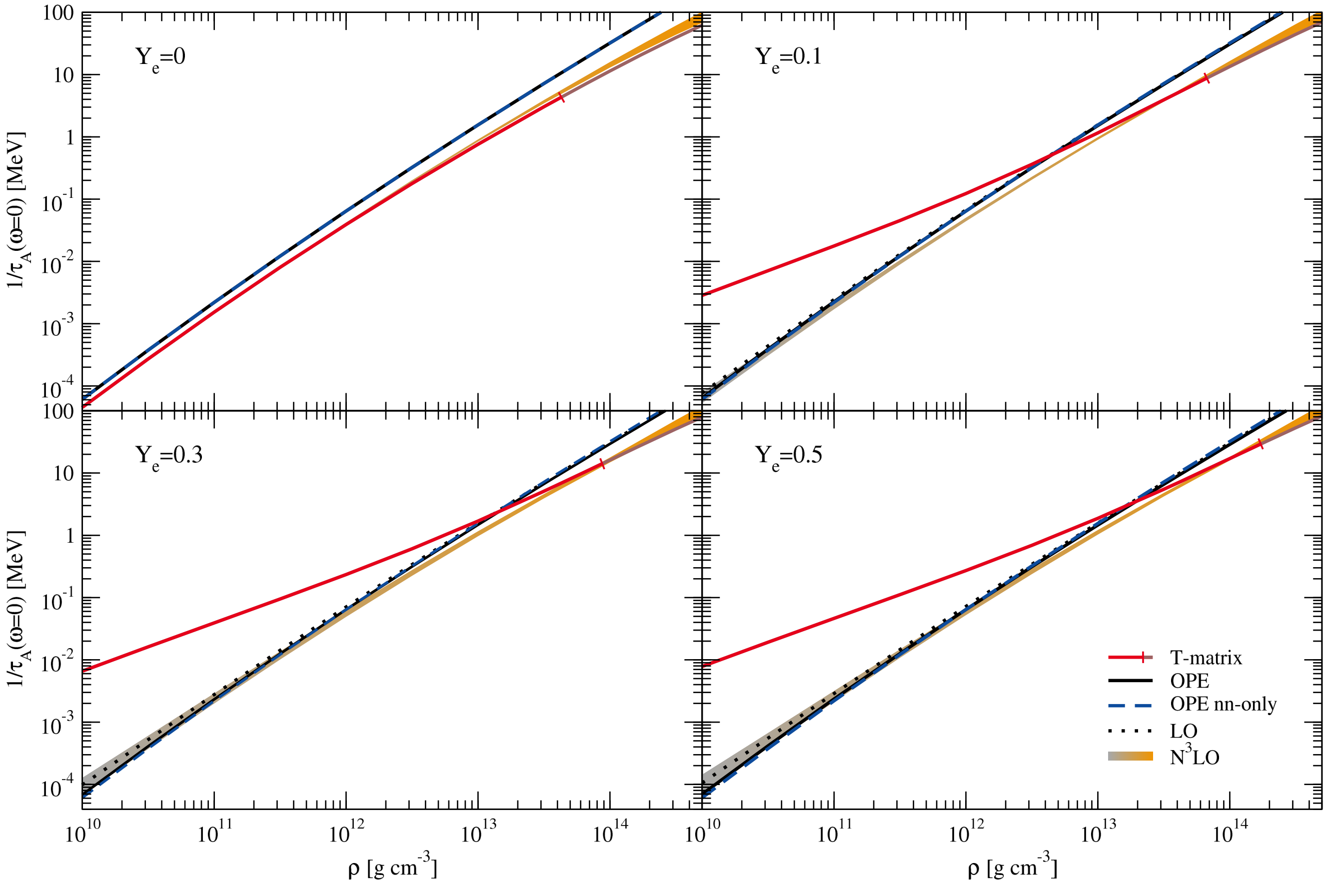

Figure 4.3: Spin relaxation rate $1/\tau_A$ at $\omega = 0$ as a function of density ρ for different electron fractions Y_e from pure neutron matter to symmetric nuclear matter. The temperature is density dependent along typical supernova conditions, Eq. (2.44). The black solid line shows results for the OPE approximation, the blue dashed line additionally assumes pure neutron matter, conceptually similar to approximations used in supernova simulations (see text). The dotted black line shows results from leading-order (LO) chiral EFT interactions, and including NN interactions at N^{3}LO at the Born level we obtain the grey-orange band. The color change from grey to orange indicates that the N^{3}LO results should only be trusted at higher densities where the Born approximation works well. In addition, we show the results based on NN phase shifts (T-matrix) in red. The T-matrix results are expected to be valid up to a fugacity of $z = 1/2$, which is marked by the small bar.

we find a striking enhancement of the rates at low densities $\rho \lesssim 10^{13}\,\mathrm{g\,cm^{-3}}$ compared to both the N^{3}LO and OPE results. The small bar indicates the density at which the fugacity $z \approx n_n \lambda_n^3/2$ with neutron thermal wavelength λ_n reaches 1/2. Below this, the T-matrix results are expected to be valid. Above, they agree well with the N^{3}LO results, thus supporting each other.

To find the source of the low-density enhancement, we employ increasingly stronger approximations of the T-matrix potential and show the results in Figure 4.4.

In the first step, we neglect all partial waves with $l \geq 1$, keeping only the S-waves. We can then write Eq. (4.50) as

$$
\begin{aligned}
\Upsilon_A^{ij}\Big|_{\text{S-wave}} =& 16\sqrt{\pi}\, n_i n_j \frac{\sinh\big(\omega/(2T)\big)}{\omega\sqrt{2m_{ij}^* T^3}} \int_0^\infty dp\, p^2 \sqrt{p^2 + 2m_{ij}^*\omega}\, e^{-p^2/(2m_{ij}^* T) - \omega/(2T)} \sum_{S\tilde{S}T\tilde{T}} \sum_{LJ\tilde{J}} (-1)^{L+J+\tilde{J}} \left(\hat{L}\hat{J}\hat{\tilde{J}}\right)^2 \frac{1}{\hat{S}\hat{\tilde{S}}} \\
& \times \left(1-(-1)^{S+T}\right)\left(1-(-1)^{\tilde{S}+\tilde{T}}\right) \begin{Bmatrix} 0 & 0 & L \\ 0 & 0 & 0 \end{Bmatrix} \begin{Bmatrix} 0 & 0 & L \\ S & S & J \end{Bmatrix} \begin{Bmatrix} 0 & 0 & L \\ \tilde{S} & \tilde{S} & \tilde{J} \end{Bmatrix} \left\langle p \middle| \mathcal{T}_{00JS}^{ij,T} \middle| p' \right\rangle \left\langle p' \middle| \mathcal{T}_{00\tilde{J}\tilde{S}}^{ij,\tilde{T}} \middle| p \right\rangle \\
& \times \sum_{M_S M_S'} C_{L\Delta M_S S M_S'}^{S M_S} C_{L\Delta M_S \tilde{S} M_S'}^{\tilde{S} M_S} \begin{cases} C_A^{i\,2} M_S\, \Delta M_S & \text{for } i = j, \\ \frac{1}{8}(C_A^{i\,2} + C_A^{j\,2})(1 - M_S M_S') + \frac{1}{2} C_A^i C_A^j \left(M_S\, \Delta M_S - \frac{1}{2}(1 - M_S M_S')\right) & \text{for } i \neq j. \end{cases}
\end{aligned}
\tag{4.61}
$$

The first $6j$ symbol evaluates to δ_{L0}. From the other two $6j$ symbols we obtain $S = J$ and $\tilde{S} = \tilde{J}$. The Clebsch-Gordan coefficients are non-zero only if $\Delta M_S = 0$ and the only surviving M_S terms for $\Delta M_S = 0$ require $M_S = M'_S = 0$. Furthermore, $T = 1 - S$ and $\tilde{T} = 1 - \tilde{S}$. The expression thus simplifies significantly,

$$\begin{aligned}\Upsilon_A^{ij}(\omega=0)\Big|_{\text{S-wave}} &= 4\sqrt{\pi}\, n_i n_j \frac{1}{\sqrt{2m^*_{ij}T^5}} \left(C_A^{i\,2} + C_A^{j\,2} - 2C_A^i C_A^j\right)(1-\delta_{ij}) \\ &\quad \times \sum_{S\tilde{S}} (-1)^{S+\tilde{S}} \int_0^\infty dp\, p^3\, e^{-p^2/(2m^*_{ij}T)} \left\langle p \left| \mathcal{T}^{ij,T}_{00JS} \right| p \right\rangle \left\langle p \left| \mathcal{T}^{ij,\tilde{T}}_{00\tilde{J}\tilde{S}} \right| p \right\rangle . \end{aligned} \tag{4.62}$$

Instead of using the T-matrix expressions based on phase shifts, we can write the matrix elements in terms of the scattering length

$$\left\langle p \left| \mathcal{T}^{ij,T}_{00JS} \right| p \right\rangle = -\frac{1}{2m^*_{np}} \frac{1}{-{}^1\!/\!{}_a - ip} , \tag{4.63}$$

where a is either the ${}^1\mathrm{S}_0$ or ${}^3\mathrm{S}_1$ scattering length. In this case, the integral can be evaluated analytically,

$$I_{a_1,a_2} = \mathrm{Re}\left[\int \mathrm{d}p\, p^3 \exp(-p^2/2m^*_{np}T) \left(\frac{1}{2m^*_{np}}\right)^2 \frac{1}{{}^1\!/\!{}_{a_1} + ip} \frac{1}{{}^1\!/\!{}_{a_2} - ip}\right] \tag{4.64}$$

$$\begin{aligned} &= \frac{T}{4m^*_{np}} - \frac{a_2}{8a_1^2(a_1+a_2)m^{*\,2}_{np}} \exp\left(\frac{1}{2a_1^2 m^*_{np}T}\right) \Gamma\left(0, \frac{1}{2a_1^2 m^*_{np}T}\right) \\ &\quad - \frac{a_1}{8a_2^2(a_1+a_2)m^{*\,2}_{np}} \exp\left(\frac{1}{2a_2^2 m^*_{np}T}\right) \Gamma\left(0, \frac{1}{2a_2^2 m^*_{np}T}\right) \\ &= I_{a_2,a_1} , \end{aligned} \tag{4.65}$$

where Γ is the incomplete gamma function and the imaginary parts cancel in the calculation.

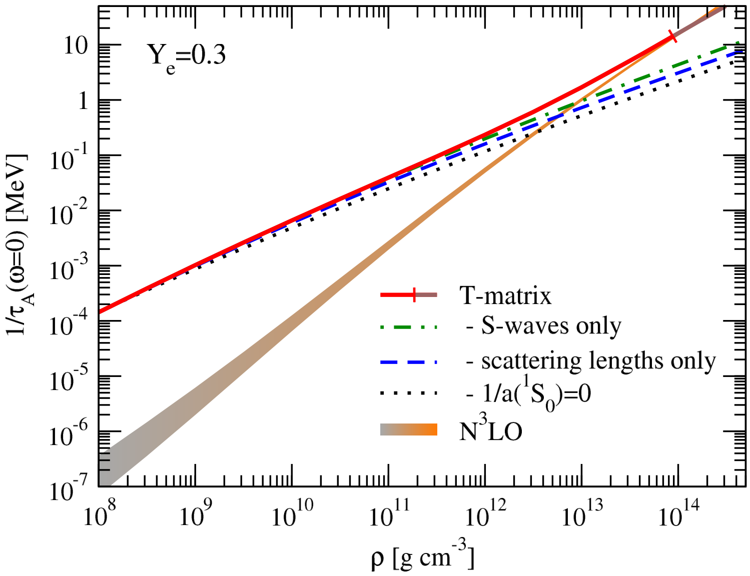

Figure 4.4: T-matrix results for $1/\tau_A(\omega = 0)$ as a function of density ρ for $Y_e = 0.3$, with temperature along supernova conditions (2.44) (identical to third panel of Fig. 4.3). The full T-matrix results (solid line) are compared to various approximations: keeping only S-waves (dash-dotted line), only S-wave scattering lengths (dashed line), and finally also setting the ${}^1\mathrm{S}_0$ scattering length to infinity (dotted line). For comparison, the N^{3}LO results are also shown.

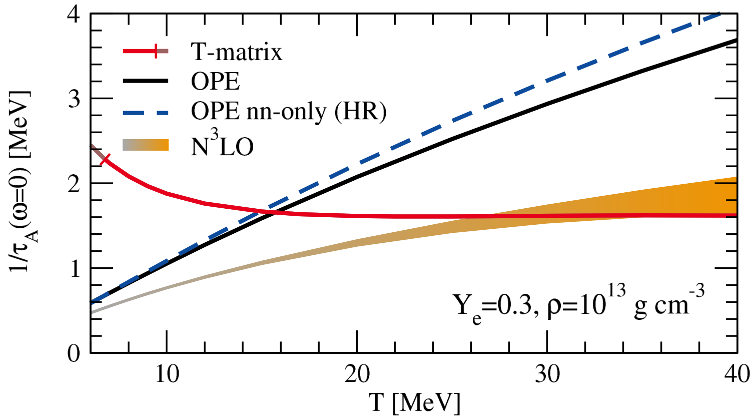

Figure 4.5: Spin relaxation rate $1/\tau_A(\omega = 0)$ as a function of temperature T for $\rho = 10^{13}\,\mathrm{g\,cm^{-3}}$ and a typical $Y_e = 0.3$. The temperature $T = 13.9\,\mathrm{MeV}$ is also used at this density in earlier plots. See Fig. 4.3 for a description of the lines.

Finally, we set the already large $^1\mathrm{S}_0$ scattering length to infinity, leaving the $^3\mathrm{S}_1$ scattering length as the only parameter:

$$\lim_{a_1\to\infty}\left(I_{a_1,a_1} - 2I_{a_1,a_2} + I_{a_2,a_2}\right) = \frac{1}{8a_2^2 m_{np}^{*2}} \exp\left(\frac{1}{2a_2^2 m_{np}^* T}\right) \Gamma\left(0, \frac{1}{2a_2^2 m_{np}^* T}\right). \tag{4.66}$$

Combining this equation with Eqs. (4.62) and (4.5), we find a simple analytical expression for the relaxation rate in this limit,

$$\frac{1}{\tau_A(\omega = 0)} \approx \frac{8\pi\, n_n n_p\, x}{n\sqrt{2\pi\, T}(m_{np}^*)^{3/2}}\, e^x\, \Gamma(0, x), \tag{4.67}$$

where $x^{-1} = 2m_{np}^* T\left(a(^3\mathrm{S}_1)\right)^2$. As clearly visible in Fig. 4.4, this still reproduces our results at small densities. We therefore conclude that the enhancement is caused by the large scattering lengths of nuclear physics and the fact that nuclear matter behaves similar to a resonant Fermi gas at subnuclear densities [149]. A next step would therefore be to calculate chiral results beyond the Born approximation.

We find a similar enhancement at low temperatures (Fig. 4.5). This is due to the fact that the energy scale of the collision is set by the temperature in the non-degenerate limit. At higher temperatures, T-matrix and N^{3}LO results agree again and are a factor of ~ 2 smaller compared to the OPE calculations.

4.2.3 SRG-Evolved Potentials

In addition, we looked at SRG-evolved potentials, mainly as a preparation for using three-body potentials later in this chapter (Figure 4.6). In both panels we show the unevolved EM 500 potential used in the previous sections along with SRG-evolved potentials provided by Kai Hebeler [88]. The unevolved potential and the SRG potential at very high resolution scale agree perfectly, providing a check for our code that reads in the new potentials.

In pure neutron matter, the rate shows hardly any dependence on the SRG parameter at low densities and a small dependence at high densities. This difference at high densities becomes slightly reduced at $Y_e = 0.3$. However, the difference becomes significant at small ρ as the SRG evolution changes the low-energy contact terms including C_T. This is connected to the widening of the N^{3}LO band at low densities and $Y_e > 0$ in Figure 4.3. Of course, the result should be independent of λ, but we neglect induced three-body forces and do not evolve our operator, see discussion in Section 3.5. Hence, the variation with λ should not be considered a complete error band.

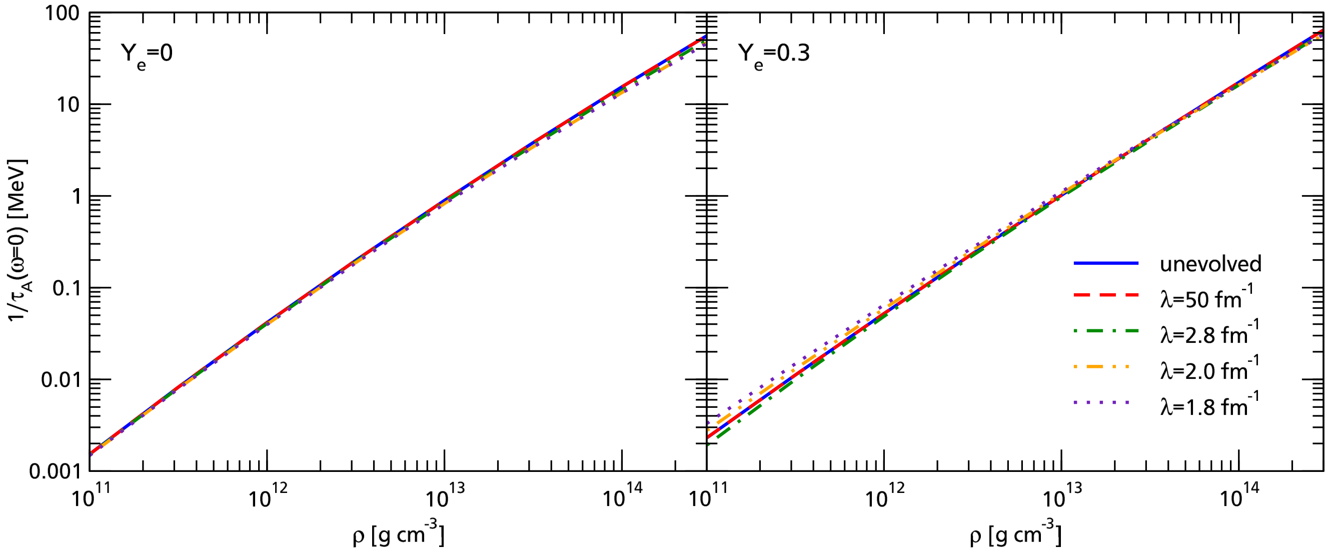

Figure 4.6: Dependence on the SRG evolution parameter. Relaxation rate at $\omega = 0$ with the EM 500 potential in pure neutron matter (left panel) and at $Y_e = 0.3$ (right panel) as a function of density along the temperature relation of Eq. (2.44). The unevolved potential (blue solid line) is the same as in the previous sections. We also show the effectively unevolved potential at $\lambda = 50\,\mathrm{fm}^{-1}$ (red dashed line) as well as the potential evolved to $\lambda = 2.8\,\mathrm{fm}^{-1}$ (green dash-dotted line), $\lambda = 2.0\,\mathrm{fm}^{-1}$ (orange dash-dot-dotted line), and $\lambda = 1.8\,\mathrm{fm}^{-1}$ (indigo dotted line).

4.3 Mean-Free Path for Pair Absorption

As it has been mentioned in Section 2.2.1, astrophysically relevant quantities can easily be derived from the structure factor. For example, the energy-averaged inverse mean-free path for a neutrino against pair absorption is given by [51]

$$\left\langle \lambda^{-1} \right\rangle = \left\langle 2\pi\, G_\mathrm{F}^2\, n \int \frac{\mathrm{d}^3 k_2}{(2\pi)^3} (3 - \cos\theta)\, \bar{f}_2\, S_A(\omega) \right\rangle_{E_\nu} \tag{4.68}$$

$$= 2\pi\, G_\mathrm{F}^2\, n \frac{\int \frac{\mathrm{d}^3 k_1}{(2\pi)^3} \int \frac{\mathrm{d}^3 k_2}{(2\pi)^3} (3 - \cos\theta)\, f_1 \bar{f}_2\, S_A(\omega)}{\int \frac{\mathrm{d}^3 k_1}{(2\pi)^3} f_1} \,. \tag{4.69}$$

Here, G_F is Fermi's constant, n the particle density, T the temperature, $\omega = E_\nu + E'_\nu$ the sum of the neutrino and antineutrino energies, and f_1 and $\bar{f}_2$ are the neutrino and antineutrino distribution functions. These can be determined in the simulation or a Fermi-Dirac or Maxwell-Boltzmann distribution can be assumed. In the latter case, Eq. (4.69) can be simplified, yielding a single ω-integral over the structure factor S_A,

$$\left\langle \lambda^{-1} \right\rangle = 2\pi\, G_\mathrm{F}^2\, n \frac{\pi^2}{T^3} \frac{(4\pi)^2}{(2\pi)^6}\, 3 \int\limits_0^\infty \mathrm{d}E_\nu \int\limits_0^\infty \mathrm{d}E'_\nu\, E_\nu^2\, E'^2_\nu\, e^{-\frac{E_\nu + E'_\nu}{T}}\, S_A(\omega) \tag{4.70}$$

$$= 2\pi\, G_\mathrm{F}^2\, n \frac{\pi^2}{T^3} \frac{3}{4\pi^4} \int\limits_0^\infty \mathrm{d}\omega\, e^{-\frac{\omega}{T}} S_A(\omega) \underbrace{\int\limits_0^\omega \mathrm{d}E'_\nu\, (\omega - E'_\nu)^2\, E'^2_\nu}_{=\,\omega^5/30} \tag{4.71}$$

$$= \frac{G_\mathrm{F}^2}{20\pi} \frac{n}{T^3} \int\limits_0^\infty \mathrm{d}\omega\, \omega^5 e^{-\omega/T} S_A(\omega) \,. \tag{4.72}$$

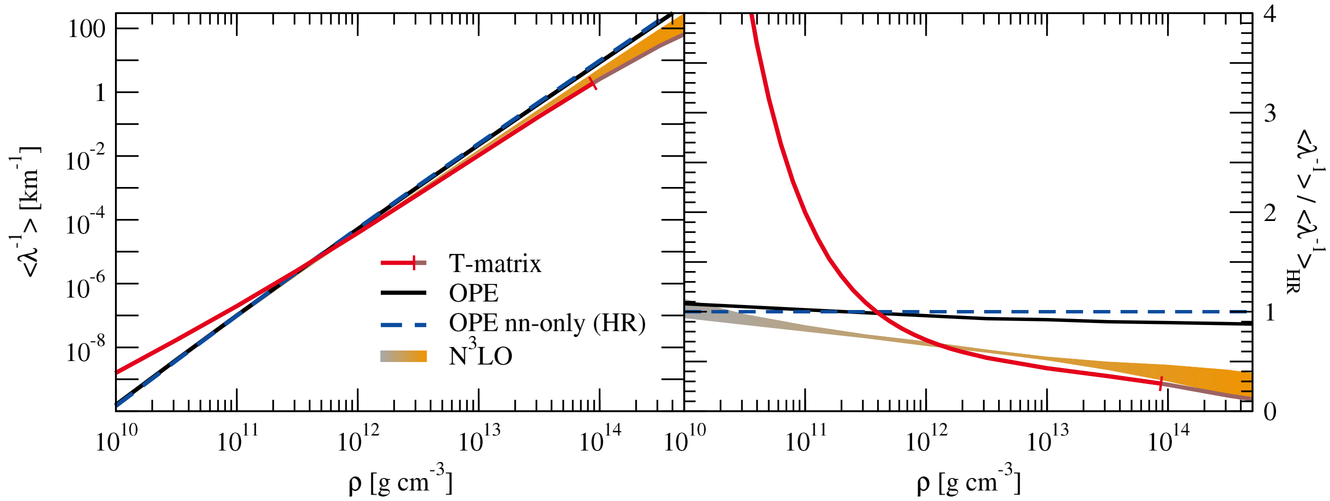

Figure 4.7: Left panel: Energy-averaged inverse mean-free path $\langle\lambda^{-1}\rangle$ of a neutrino against pair absorption as a function of density ρ for $Y_e = 0.3$, with temperature along typical supernova conditions (2.44). Right panel: Same data, but normalized to the OPE nn-only result.

If we instead assumed Fermi-Dirac distributions, we would have to do two integrals (over E_ν and E'_ν). This is conceptually just as straightforward, but it requires more resources. Hence, we use Maxwell-Boltzmann distributions unless mentioned otherwise.

To give a first insight into the astrophysical impact of our findings, we show the energy-averaged inverse mean-free path of a neutrino against pair absorption along typical supernova temperatures given by Eq. (2.44) in Fig. 4.7. The enhancement at low densities ($\rho \lesssim 10^{12}\,\mathrm{g\,cm^{-3}}$) is reduced compared to Figure 4.3 because the T-matrix based spin relaxation rate decreases faster with increasing ω than OPE or chiral EFT based rates and the integral in Eq. (4.72) samples S_A at various ω. Again, the T-matrix and N^{3}LO results are very close at higher densities.

4.4 OPE nn-only vs. Hannestad & Raffelt

As mentioned in the introduction of this chapter, supernova simulations often rely on the structure factor provided by Hannestad and Raffelt [51]. In the previous sections, we compared our T-matrix and chiral results to calculations done in our formalism, but conceptually similar to HR, i. e., using $Y_e = 0$, the one-pion-exchange potential, and the long-wavelength structure factor. In this section, we compare these OPE nn-only results to numbers obtained with the actual HR structure factor.

The top panel of Figure 4.8 shows the energy-averaged absorption opacities for $NN\nu\bar{\nu} \to NN$ as a function of density and with the temperature set by Eq. (2.44). HR and OPE results seem to agree quite well for most densities, but at a few times $10^{13}\,\mathrm{g\,cm^{-3}}$ deviations become visible. Since the y-axis is logarithmic and spans many orders of magnitude, the actual ratio is hard to read off. We therefore plot the same numbers again in the second panel, this time relative to the OPE result. Deviations increase from 10 to 30 % for densities between 10^{10} and $6 \times 10^{13}\,\mathrm{g\,cm^{-3}}$. Afterwards, deviations grow even faster.

One possible explanation for this deviation is degeneracy. At the upper end of the density range, the temperature is about two thirds of the Fermi temperature T_F, so degeneracy effects are expected to contribute. Our formalism is purely non-degenerate (but was shown in pure neutron matter to be a good approximation for partially-degenerate matter, see Ref. [57]), while the HR formalism interpolates between degenerate and non-degenerate conditions.

In order to test this explanation, we make the conditions more degenerate in the third panel by reducing the temperature by a factor of 5. At low densities, OPE and HR still visually agree. At $10^{14}\,\mathrm{g\,cm^{-3}}$, $T/T_\mathrm{F} \approx 0.2$ and deviations between the non-degenerate OPE result and the HR calculation are significant. A degenerate version of our formalism is available [47, 148] which we would expect to match the HR results at lower T/T_F. The opacity obtained with this structure factor is also shown in the third panel. While it lies closer to the HR opacity at high densities, there is still a significant deviation.

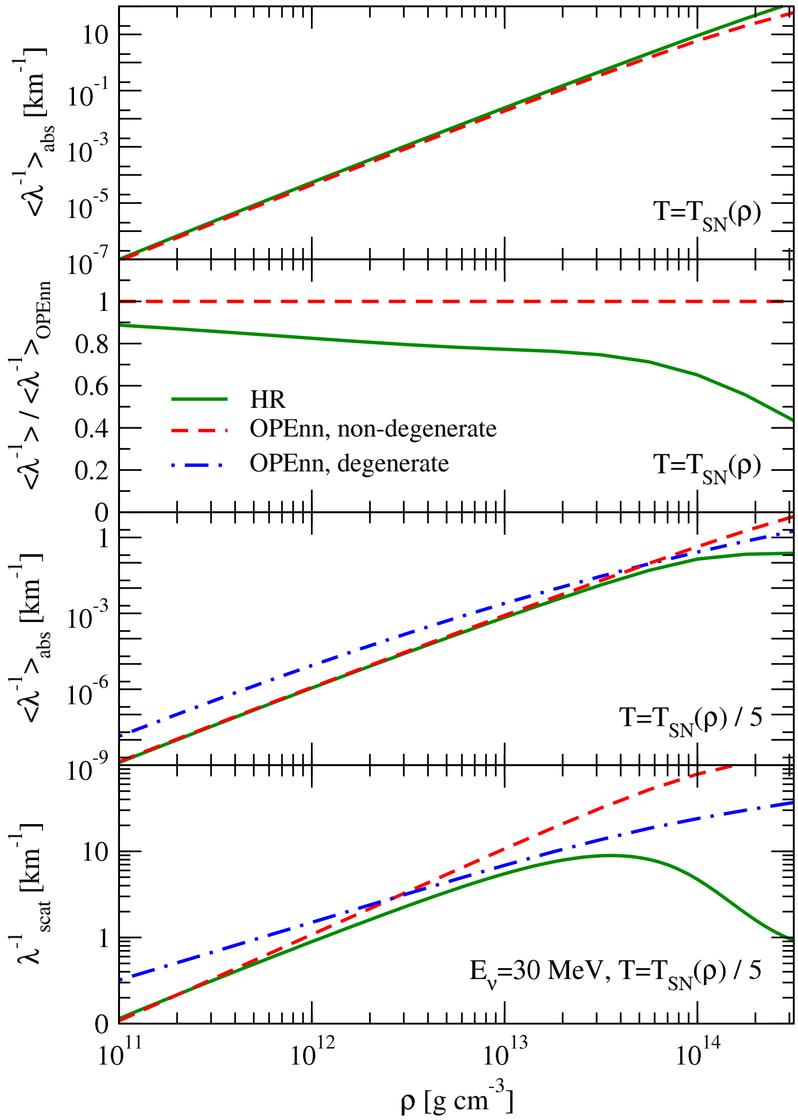

Figure 4.8: Comparison between HR and our OPE mean-free paths in pure neutron matter as a function of density. The bottom plot shows the energy-dependent inverse mean-free path for scattering (calculated with our $q \to 0$ structure factor, see also Section 6.3), while the other plots show energy-averaged absorption opacities. The two topmost panels are calculated along the conditions of Eq. (2.44), for the lower two panels temperature is reduced by a factor of 5. In these panels we show degenerate results (blue dash-dotted line) in addition to our non-degenerate results (red dashed line) and the HR result (green solid line) shown in all panels. The data in the two topmost panels is identical; in the second panel, we show the HR result relative to the OPE calculation to allow for an easier comparison.

The HR opacity levels off and would eventually decrease if we increase the density even further. This maximum can be moved to lower densities by making the conditions even more degenerate. We consider it unphysical as a denser medium should always be more opaque.

The peak in the HR opacity is even more visible if we look instead at the inverse mean-free path for a 30 MeV neutrino against scattering on interacting nucleons (bottom panel of Figure 4.8 – this process will be looked at in detail in Section 6). Our findings are similar to the absorption opacities. At low densities, the non-degenerate structure factor agrees reasonably well with the HR result. Deviations grow and for a while (in this case between a few times $10^{12}\,\mathrm{g\,cm^{-3}}$ and $\approx 2 \times 10^{13}\,\mathrm{g\,cm^{-3}}$) our degenerate results lie rather close to the HR computations. For this process, the HR inverse mean-free path reaches its maximum already at about $3 \times 10^{13}\,\mathrm{g\,cm^{-3}}$ and then decreases by an order of magnitude.

The occurrence of a maximum can be traced back to a function called $g(y,\eta_\star)$ in the HR formalism, where $y \sim T^{-1}$ and $\eta_\star \sim \rho^{2/3}T^{-1}$. This function is introduced to include multiple-scattering effects. If g is set, e. g., to 0.1 independent of its arguments, the peak disappears.

With this likely unphysical behavior of the HR opacities, it cannot be our goal to reproduce the HR numbers with our formalism. While the two calculations differ significantly, insights can be gained from comparing our improved results to both of them: Comparing to HR numbers indicates the change in the opacities etc. one would see in supernova simulations if they implemented our rates rather than HR. The comparison with OPE *nn*-only results on the other hand has the advantage that the assumptions and approximations of the formalism are the same and we can directly look at the impact of the more advanced nuclear potentials compared to OPE.

4.5 Impact of Three-Body Forces

In order to investigate the impact of three-body forces on the neutrino opacities, we employ the formalism of normal-ordering discussed in Section 3.6, using Eq. (3.26). We concentrate on densities in the range of $n_0/10$ to n_0, where $n_0 = 0.16\,\text{fm}^{-3}$ is the nuclear saturation density. We fix the temperature for each density according to the relation in Eq. (2.44).

The top panel of Figure 4.9 shows the relaxation rate at $\omega = 0$ in pure neutron matter. We use the EM 500 potential as a baseline (green line) and add normal-ordered three-body interactions at N^{2}LO and N^{3}LO. The

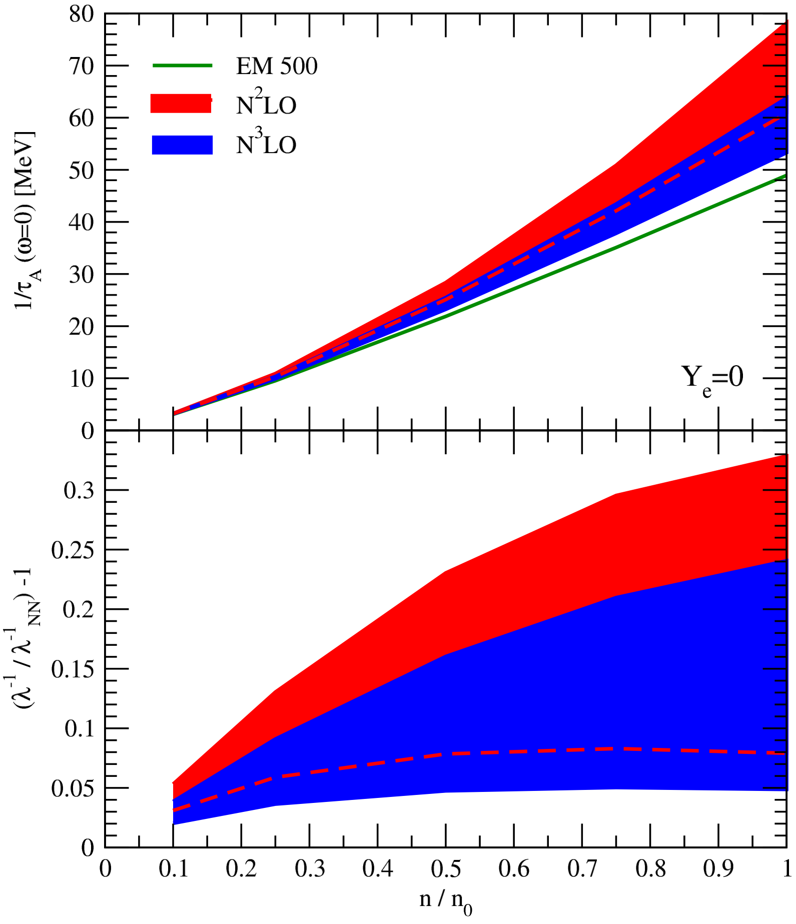

Figure 4.9: Relaxation rate $1/\tau_A(\omega = 0)$ (top) and opacity shift with three-body forces relative to the two-body result (bottom) as a function of particle density n in pure neutron matter. The blue band includes three-body forces up to N^{3}LO, while in the red band only three-body forces at N^{2}LO are included. The bands are spanned by variations in Λ_{3N}, c_1, and c_3 (see text). The green solid line shows the result without three-body forces and using the EM 500 potential. In the lower panel, this is 0 by definition.

bands are spanned by varying the three-body cutoff $\Lambda_{3N} = 2.0, 2.5\,\mathrm{fm}^{-1}$ as well as the low-energy constants $c_1 = -(0.37\ldots0.81)\,\mathrm{GeV}^{-1}$ $(-(0.75\ldots1.13)\,\mathrm{GeV}^{-1})$ and $c_3 = -(2.71\ldots3.40)\,\mathrm{GeV}^{-1}$ $(-(4.77\ldots5.51)\,\mathrm{GeV}^{-1})$ in the three-body forces at N^{2}LO (N^{3}LO). These are the ranges suggested by Ref. [111] and discussed in Ref. [100]. The LEC c_4 does not contribute.

Three-body forces increase the relaxation rate. At saturation density, we find an increase of about 24 — 60 % at the N^{2}LO level. This effect is strongly reduced when the next order is also taken into account, leading to a 9 — 30 % effect. As expected, the higher-order band is smaller in width.

As shown in Section 4.3, just looking at the $\omega = 0$ rate can overestimate effect sizes. To sample the whole ω range, we again calculate the energy-averaged inverse mean-free path against pair absorption, assuming Maxwell-Boltzmann distributions for both the neutrino and antineutrino. In the lower panel of Figure 4.9 we show the effect size of three-body forces on the neutrino opacities relative to the two-body-only result, namely the EM 500 potential. The overall trends are similar to those for the relaxation rate, however the three-body impact at N^{2}LO is significantly reduced and the two bands overlap much more. At nuclear saturation density, the three-body effect on the opacities is 8 — 33 % if one only takes the leading N^{2}LO forces into account. It reduces to 5 — 24 % at N^{3}LO. Below $n_0/10$, 3N forces have a small impact, as was expected.

As the EM 500 potential that is used as a reference is calculated at N^{3}LO, consistent calculations should include three-body forces at that order, too. However, three-body forces in mixtures include terms proportional to the three-body coupling constants c_D and c_E that have to be fit to few-body observables. No reasonable fits of N^{3}LO three-body potentials are currently available, therefore we can only use N^{3}LO potentials in pure neutron matter where the c_D and c_E terms do not contribute [140].

To be completely consistent, four-body forces should also be included at N^{3}LO. However, these were shown to only give minor contributions in nuclear matter calculations [100, 109], so we also expect them to be minor for the inverse mean-free path.

For the following calculations, we use six normal-ordered potentials provided by Christian Drischler [102] with c_D and c_E fit to the triton binding energy and the alpha particle charge radius [88]. All six potentials use SRG-evolved EM 500 potentials in the NN sector. Four of the potentials use the EM 500 coupling constants c_i while varying the SRG cutoff λ. Potential 3 uses a different three-body cutoff Λ_{3N} while potential 6 uses c_i values from the partial-wave analysis (PWA) in Ref. [160]. While this is inconsistent with the EM 500 c_i's in the two-body sector, it allows to check the c_i dependence of our results. The potential parameters along with the fit c_D and c_E are shown in Table 4.1. The normal-ordering was done assuming a free Fermi-Dirac spectrum in Eq. (3.27).

In Figures 4.10 and 4.11, we present our results for these potentials. We again plot the effect size going from the NN-only to the $NN+3N$ calculation. Here, NN refers to the SRG-evolved EM 500 potentials with the corresponding SRG parameters λ. While the set of six potentials does not provide a systematic (uncertainty) band, it can help estimate the impact of the uncertainties in the potential.

In pure neutron matter, we find 10 — 39 % effects, comparable to what we saw for the unevolved potentials. The dependence on λ is very small. Using the PWA instead of the EM c_i's leads to an additional increase in opacity. The strongest effect clearly comes from the three-body cutoff, with the result for $\Lambda_{3N} = 2.5\,\mathrm{fm}^{-1}$ almost 40 % larger than the corresponding two-body calculation at nuclear saturation density.

This changes completely when we look at the situation at $Y_e = 0.3$ (Fig. 4.11). Here, three-body effects are effectively non-existent for the $\Lambda_{3N} = 2.5\,\mathrm{fm}^{-1}$ potential independent of density. For the other potentials, effects

Name	$\lambda/\Lambda_{3\mathrm{N}}$ [fm^{-1}]	c_1 [GeV^{-1}]	c_3 [GeV^{-1}]	c_4 [GeV^{-1}]	c_D	c_E
EM 1.8/2.0	1.8/2.0	−0.81	−3.2	5.4	1.264	−0.120
EM 2.0/2.0	2.0/2.0	−0.81	−3.2	5.4	1.271	−0.131
EM 2.0/2.5	2.0/2.5	−0.81	−3.2	5.4	−0.292	−0.592
EM 2.2/2.0	2.2/2.0	−0.81	−3.2	5.4	1.214	−0.137
EM 2.8/2.0	2.8/2.0	−0.81	−3.2	5.4	1.278	−0.078
PWA 2.0/2.0	2.0/2.0	−0.76	−4.78	3.96	−3.007	−0.686

Table 4.1: Cutoffs and coupling constants of the potentials used in this section [88, 102].

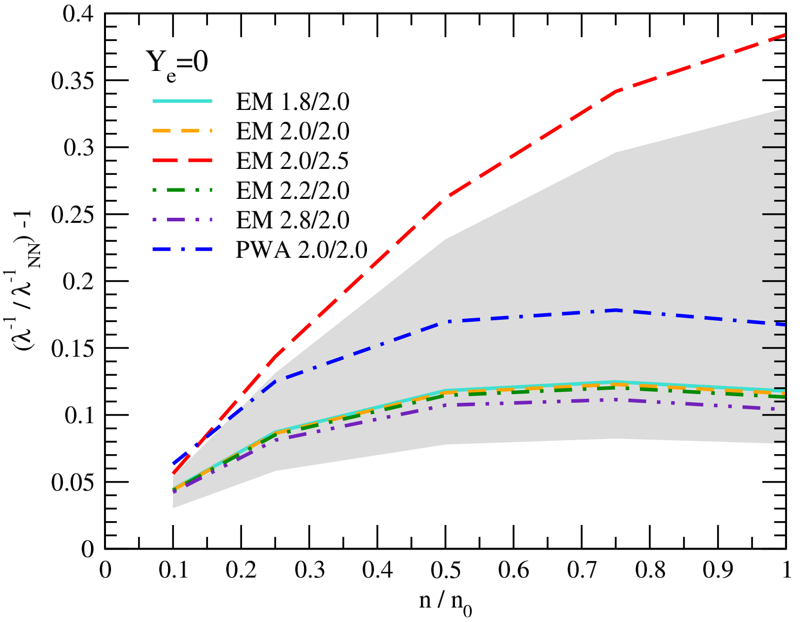

Figure 4.10: Shift in opacity obtained by including normal-ordered three-body interactions in addition to the two-body interaction as a function of particle density n in pure neutron matter. The six lines correspond to the six potentials summarized in Table 4.1. For reference, we also show the band created by the unevolved N^{2}LO potentials (grey, cf. Fig. 4.9).

are small as well, with all EM c_i potentials showing effect sizes of $\lesssim 3\%$ across the density range considered. The effects obtained with the PWA c_i's are larger, but still significantly below 10%.

To understand this behavior in more detail, we look at the Y_e dependence of three of the discussed potentials in Figure 4.12 and turn on the 3N terms one by one. The c_3 term leads to a significant increase in the opacity. In mixtures, the c_4 term counteracts this change and at $Y_e = 0.3, 0.5$ the two terms approximately cancel for the EM c_i's. The c_4 term does not contribute in pure neutron matter, explaining the large total effects seen in the previous

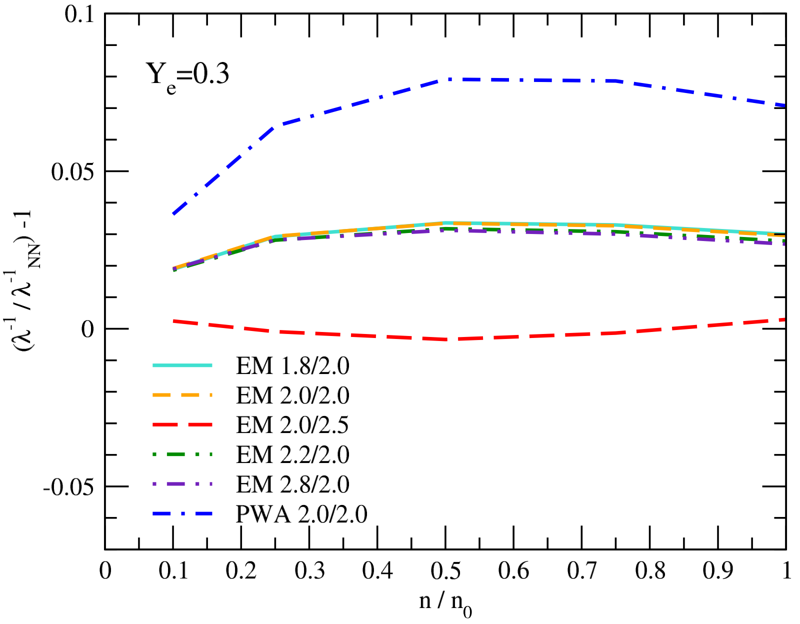

Figure 4.11: Same as Figure 4.10, but at electron fraction $Y_e = 0.3$.

figures. The other terms (c_1 in pure neutron matter, c_1, c_D, and c_E at $Y_e > 0$) only lead to small shifts, the direction of which seems to depend mainly on the sign of c_D. In particular, we conclude that the negligible effect of three-body forces at $Y_e = 0.3$ for the EM 2.0/2.5 potential is caused by an almost perfect cancellation between c_3 and c_4 terms.

The dominant part of the interaction for the opacities is the tensor part. Our results therefore hint at the c_3 and c_4 terms having tensor contributions that are comparable in size but have different signs.

We find that in mixtures, three-body forces only have a small impact on the neutrino opacity. They tend to increase the opacity, while going from OPE to chiral NN results showed a significant decrease. The chiral two-body results (as well as the T-matrix results) discussed before should therefore be good enough when estimating the impact of using modern nuclear interactions on supernova dynamics and the neutrino signal in Chapter 5.

Finally, we want to stress the fact that the dependence of the nuclear matrix elements on the isospin projection M_T should not be neglected for these calculations. In the previous sections, results were obtained using $M_T = 0$ for all matrix elements. This way, the nn, np and pp contributions in Eq. (4.50) can be combined and the integral over p only has to be evaluated once, increasing code performance.

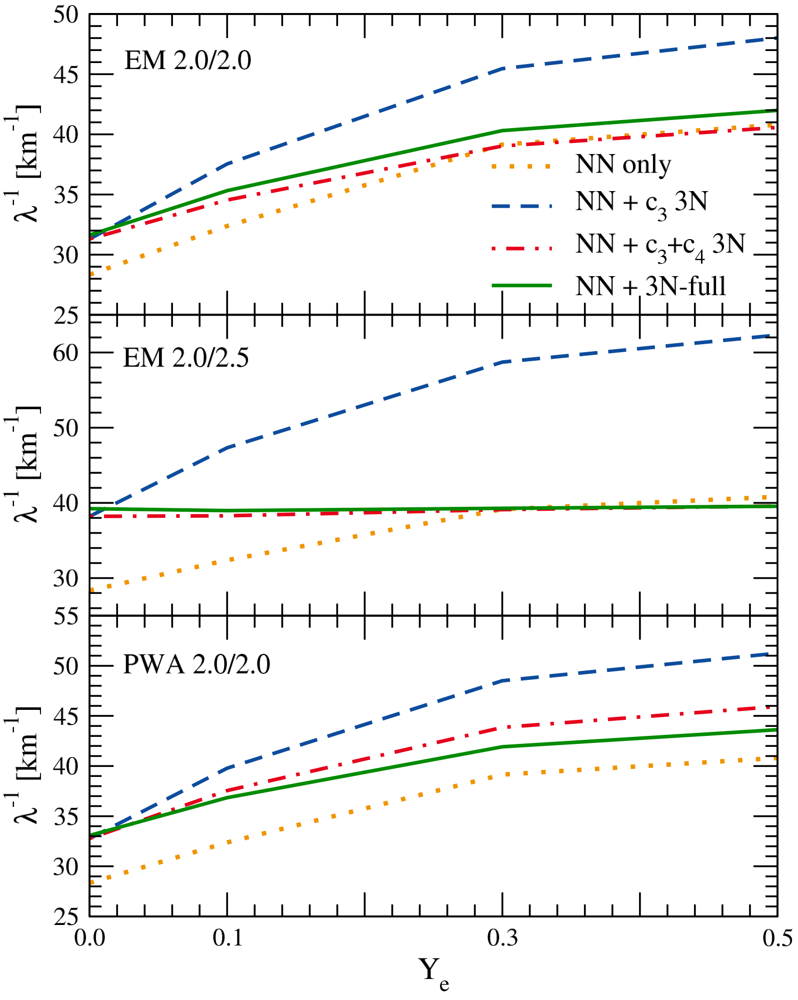

Figure 4.12: Opacity at nuclear saturation density as a function of electron fraction ranging from pure neutron matter to symmetric nuclear matter. For each of the three potentials (EM 2.0/2.0, EM 2.0/2.5, and PWA 2.0/2.0), we show the EM 500 potential evolved to $\lambda = 2.0\,\text{fm}^{-1}$ without three-body forces (orange dotted line), with the c_3 three-body term included (blue dashed line), with both the c_3 and c_4 terms included (red dash-dotted line) and the full result including all N^{2}LO three-body terms (green solid line).

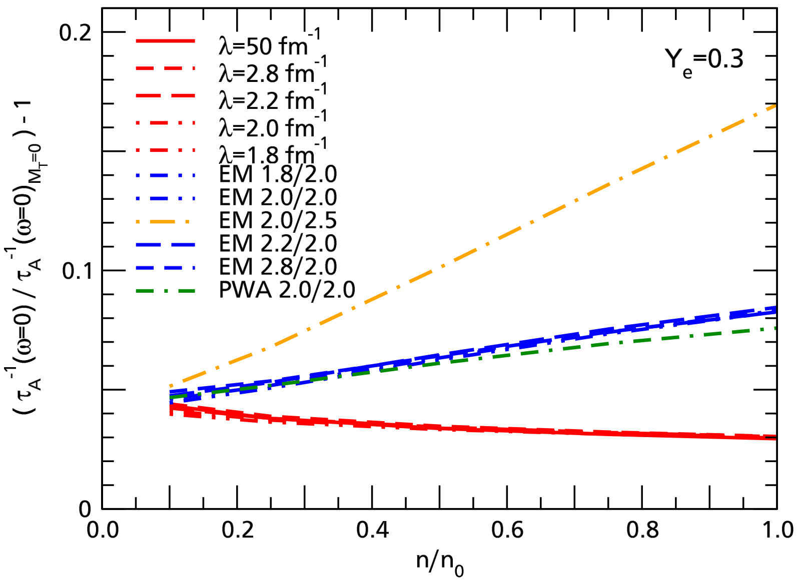

Figure 4.13: Deviation of the relaxation rate at $\omega = 0$ from the result in the $M_T = 0$ approximation as a function of density at $Y_e = 0.3$. Shown are SRG-evolved EM 500 two-body potentials (red) as well as the potentials described in Table 4.1. The $\Lambda_{3N} = 2.5\,\mathrm{fm}^{-1}$ potential is marked yellow, the potential with PWA c_i's is marked green and the remaining four are shown in blue.

In Figure 4.13 we show the deviation of the full result from the $M_T = 0$ approximation for the $3N$ Hamiltonians discussed above and for the SRG calculations shown in Section 3.5. While the deviations are around or below 4 % for all SRG potentials including the effectively unevolved $\lambda = 50\,\mathrm{fm}^{-1}$, they grow beyond 8 % for the $\Lambda_{3N} = 2.0\,\mathrm{fm}^{-1}$ potentials and more than twice as large for the $\Lambda_{3N} = 2.5\,\mathrm{fm}^{-1}$ potential. Therefore, all results shown in this section have been calculated with the full M_T dependence.

This stronger dependence of the $3N$ interactions on M_T can be motivated by looking at species labels for the right diagram in Figure 3.9: For $M_T = 0$, particles 1 and 2 are one neutron and one proton, while the third particle is either a neutron or a proton. Hence, the npn and npp three-body forces are probed. For $M_T = 1$, particles 1 and 2 are protons, hence probing ppn and ppp three-body forces, and similar for $M_T = -1$. The asymmetry of neutron-rich matter leads to an isospin-symmetry breaking that is significantly larger than the isospin dependence of nuclear forces. The leading $3N$ interactions are isospin symmetric and the isospin dependence in the NN sector is small.

5 Explorations in Supernovae

In Chapter 4, “typical” supernova conditions were considered. However, evaluating the impact of our findings on supernova dynamics and neutrino signals requires more realistic conditions based directly on supernova simulations. In this chapter, we present results from two different strategies, in collaboration with astrophysicists, that explore the impact our improved interaction rates have in supernovae.

5.1 Post-Processing with Detailed Rates

Together with Hannah Yasin, Albino Perego, and Almudena Arcones from TU Darmstadt we have evaluated the impact of our improved rates under more realistic conditions than in Section 4.3 by post-processing simulations. Post-processing means that the numerical simulations have been performed without our detailed rates. These are then applied along the radial profiles obtained in these simulations. This treatment does not take into account the feedback on the supernova dynamics or thermodynamic conditions.

5.1.1 Method

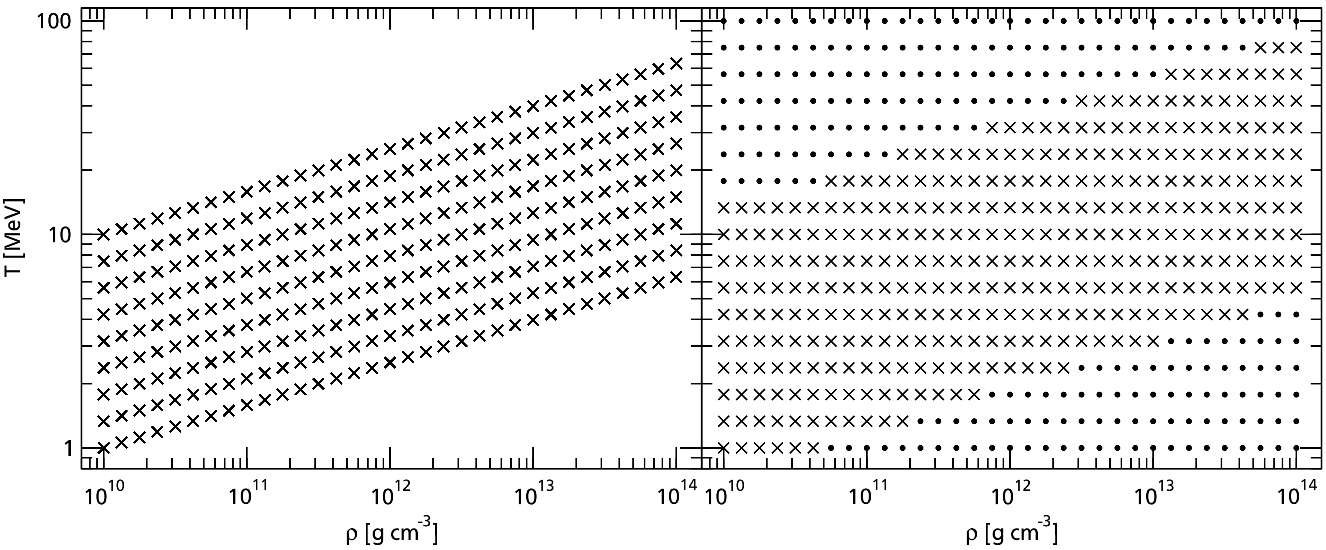

Figure 5.1: Skewed (left) and rectangular (right) ρ–T grid used for the tables. Dots indicate conditions where instead of a calculation $\mathrm{Im}\chi_A = 0$ was used.

Rather than to recalculate the rate for each set of (ρ, T, Y_e) occurring in the profiles, we provide one big table so that the rates needed can be interpolated from that data. The most flexible quantity to provide is the structure factor. The inverse mean-free path can be easily calculated from this according to Eq. (4.69) or (4.72).

Instead of the structure factor S_A, we tabulate $\mathrm{Im}\chi_A$. The two are related closely (Eq. (4.2)), and unlike the structure factor, $\mathrm{Im}\chi_A$ does not have a pole at $\omega = 0$.

Keeping in mind the conditions discussed in Section 2.4, we choose the thermodynamic conditions

$$10^{10}\,\mathrm{g\,cm^{-3}} \le \rho \le 10^{15}\,\mathrm{g\,cm^{-3}}\,, \tag{5.1}$$

$$\left(\frac{\rho}{10^{10}\,\mathrm{g\,cm^{-3}}}\right)^{1/5} \mathrm{MeV} \le T \le \left(\frac{\rho}{10^{5}\,\mathrm{g\,cm^{-3}}}\right)^{1/5} \mathrm{MeV}\,, \tag{5.2}$$

$$Y_e \in \{0.01, 0.05, 0.1, 0.2, 0.3, 0.5\}\,. \tag{5.3}$$

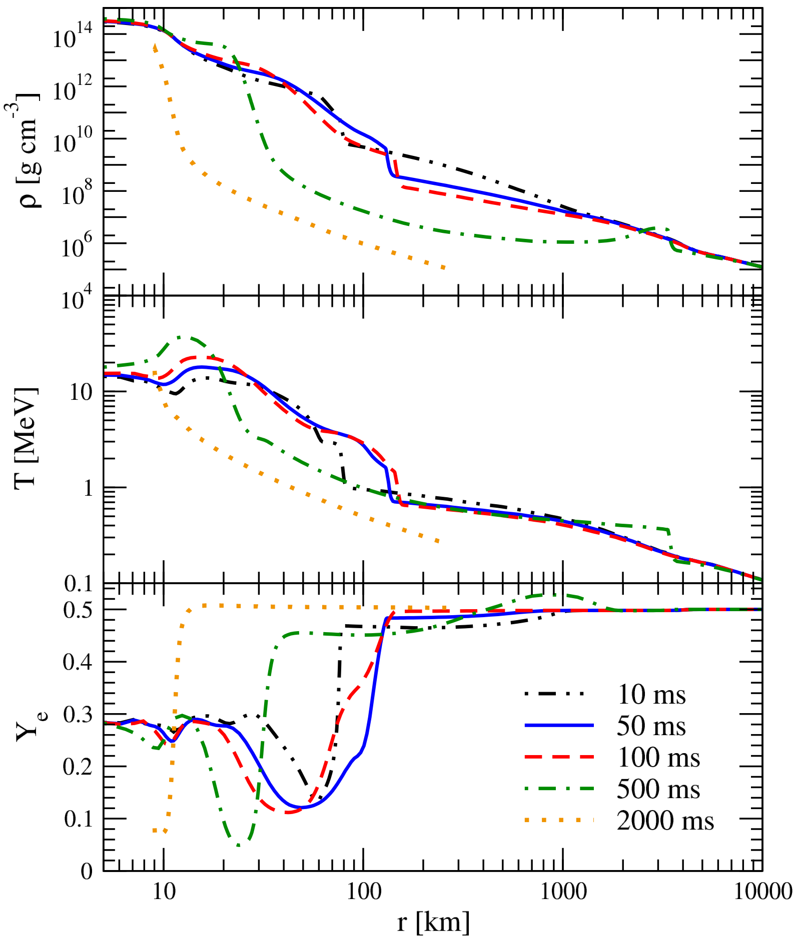

Figure 5.2: Density (top), temperature (center), and electron fraction (bottom) along the radial profiles at 10 ms (black dash-dot-dotted line), 50 ms (blue solid line), 100 ms (red dashed line), 500 ms (green dash-dotted line), and 2000 ms (orange dotted line). Not shown is the 200 ms profile which has a density and temperature profile very similar to the 50 and 100 ms profiles.

This creates a skewed ρ–T grid (left panel of Fig. 5.1), which created numerical problems in the integration. We therefore switched to a rectangular grid (right panel of Fig. 5.1) but set $\mathrm{Im}\chi_A = 0$ for values outside the band defined by Eq. (5.2).

For the ω integration we use $\Delta\frac{\omega}{T} = 1$ and $(\frac{\omega}{T})_{\mathrm{max}} = 15$ in agreement with our findings in Section A.1. The resulting table is four-dimensional (ρ, T, Y_e, and $\frac{\omega}{T}$). It contains 62 730 rows (41 steps in ρ × 17 in T × 6 in Y_e × 15 in $\frac{\omega}{T}$), 41 % of which are outside of the band and hence set to 0.

The profiles used are five profiles obtained at 10 ms, 50 ms, 100 ms, 200 ms, and 500 ms after bounce in a 1D simulation of a 18 $M_\odot$ progenitor described in Ref. [161], as well as a neutrino-driven-wind profile 2000 ms after bounce from Ref. [162]. We show the thermodynamic conditions found along these profiles in Figure 5.2. Clearly visible in the ρ and T plots is the position of the shock at approximately 65 km at 10 ms after bounce, at about 130 km at 50 and 100 ms, and at around 3000 km at 500 ms, after the shock is revived.

We also see the transition from a rather broad central density distribution to a clearly-defined central high-density region, the proto-neutron star, which subsequently shrinks and cools. The electron fraction is about 0.5 in front of the shock. Behind it, matter is neutron-rich, reaching to values of $Y_e = 0.02$ at 500 ms post-bounce. In the neutrino-driven wind (dashed orange lines), it is slightly proton-rich.

We stress again that the 2000 ms profile stems from a different simulation with a different progenitor and different codes. Some additional details on the implementation and more results can be found in Ref. [163].

We used a trilinear interpolation in ρ, T, and Y_e, along with a trapezoidal integral in $\frac{\omega}{T}$ to calculate the averaged inverse mean-free path (or opacity κ) along these profiles.

We compare various neutrino reactions along the 100 ms profile in Figure 5.3. The dominant reactions are elastic scattering on neutrons and protons. We look at ν_x, so charged-current reactions do not contribute. Pair absorption on nucleons is the dominant absorption contribution in the interior of the explosion. Beyond about 54 km, electron-positron pair creation dominates. In this plot, we also compare our OPE nn-only result (which is conceptually similar to HR) with the actual HR result. See Section 4.4 for a discussion of the difference.

The effect of T-matrix rates compared to those based on HR is shown in Fig. 5.4 for multiple times after bounce. The enhancement of T-matrix rates compared to HR at low densities is clearly visible. However, in the regions where these differences are significant, matter is quite transparent (at least for this process), so the expected impact on spectra and dynamics is small. Significant deviations are also visible at small radii, caused by the high-density reduction of T-matrix rates compared to HR as well as the HR behavior at large densities discussed in Section 4.4.

We also show results obtained directly by our code, without generating interpolation tables and feeding them into Hannah Yasin's code. This allows for a cross-check of the implementations and an evaluation of the quality of the interpolation. The direct and the interpolated results agree well.

In Table 5.1, we show the neutrinosphere positions obtained including all reactions shown in Fig. 5.3. For electron (anti)neutrinos, neutrino capture on neutrons (protons) is the dominant absorption source and the neutrinosphere position is not sensitive to changes in the bremsstrahlung/pair absorption rate on the scale we found. We therefore only show results for ν_x. The differences between the HR and T-matrix results are quite small. This is in good

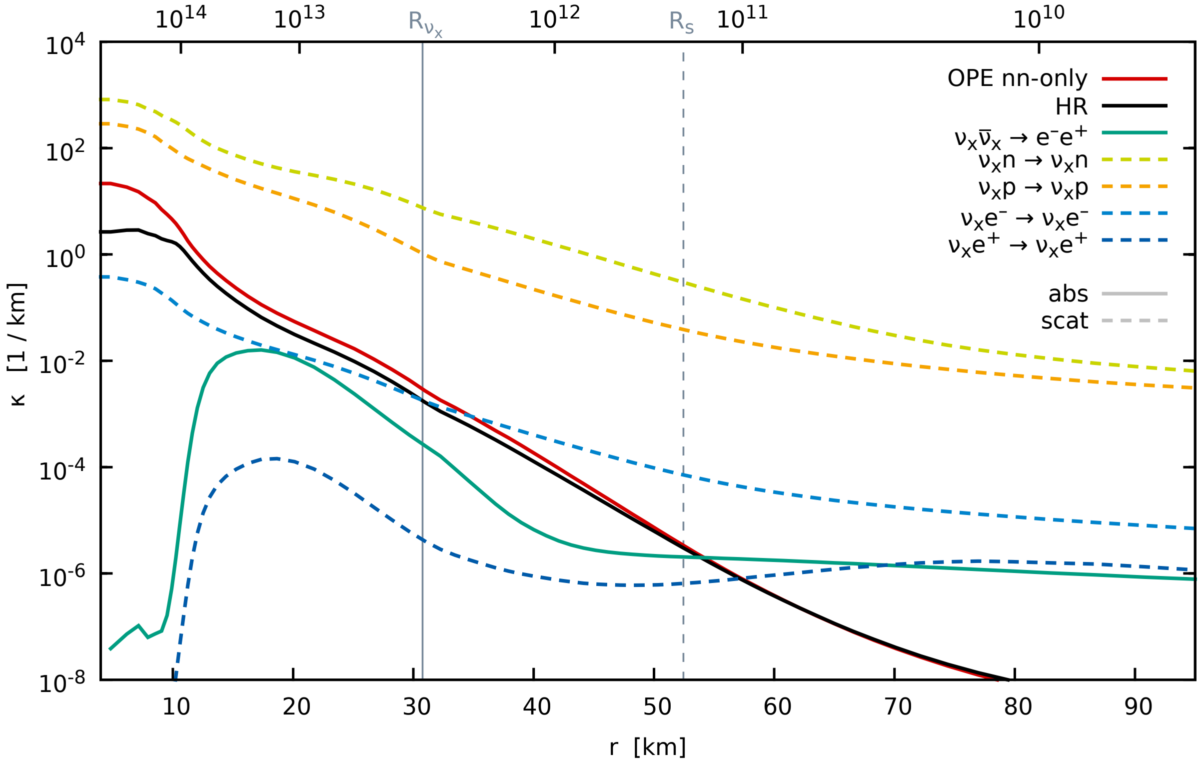

Figure 5.3: Opacity / inverse mean-free path for ν_x as a function of radius along the 100 ms profile. Shown are various scattering reactions (dashed lines) along with electron-positron pair creation (green solid line) and two pair absorption ($NN\nu\nu \rightarrow NN$) results: The black solid line shows the results obtained with the HR structure factor, the red solid line results based on the interpolation table using our formalism and OPE nn-only. The solid vertical line marks the position of the neutrinosphere while the dashed vertical line marks the (average) position of last scattering. Plot provided by Hannah Yasin, modified.

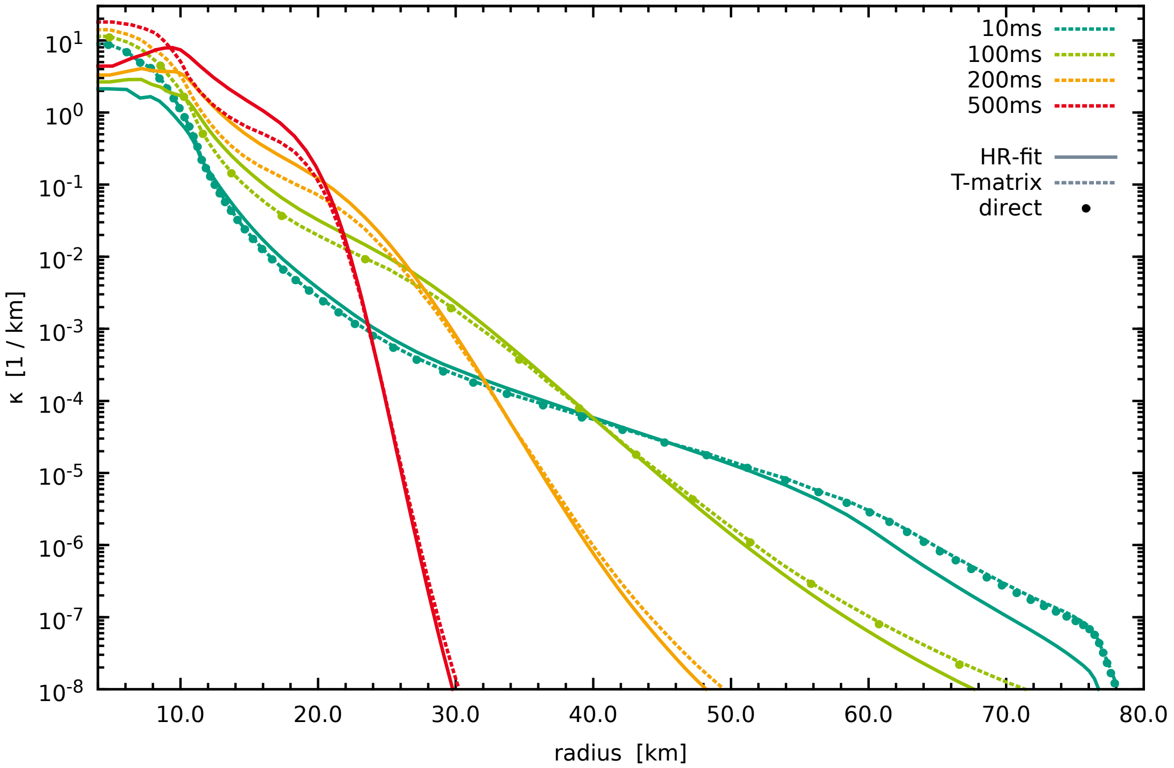

Figure 5.4: Opacity / inverse mean-free path for pair absorption as a function of radius along various profiles. The dashed lines show results based on our interpolation table and the T-matrix potential while the solid lines are based on the HR structure factor. In addition, for 10 and 100 ms we show T-matrix results directly obtained from our code without using interpolation tables (dots). The neutrino spectrum is assumed to be a Fermi-Dirac distribution, ignoring decoupling effects. Plot provided by Hannah Yasin.

agreement with the findings presented in Section 4.4, where HR (like T-matrix) gave smaller opacities than OPE nn-only at high densities. We therefore also compare to OPE results, thus evaluating the impact of the nuclear potential on the neutrinosphere. Going from OPE to T-matrix decreases the neutrinosphere radius due to the lowered opacity, which in turn increases the corresponding neutrino temperature by about $6-7\%$. Comparing T-matrix and the EM 500 chiral potential, one finds very small differences since the enhancement at low densities found in Section 4.3 lies outside the neutrinosphere while at and beyond typical neutrinosphere densities of a few times $10^{13}\,\mathrm{g\,cm^{-3}}$ the difference between EM 500 and T-matrix results are found to be small.

For νNN scattering, many more sampling points in $\frac{\omega}{T}$ are needed for a converged result. The value of the integral, which for scattering starts at negative ω, is very sensitive to values of $\mathrm{Im}\chi_A$ around 0. In addition, the inverse mean-free path was shown to be very similar to the νN opacity for typical neutrino energies (cf. Section 6.3). Therefore, we did not study this reaction in detail with interpolation tables.

	Radius [km]				Temperature [MeV]			
	HR	OPE	T-matrix	EM 500	HR	OPE	T-matrix	EM 500
50 ms	32.44	33.19	31.87	32.17	10.86	10.45	11.17	11.00
500 ms	22.09	22.23	22.01	22.05	8.13	7.84	8.30	8.21
2000 ms	9.15	9.21	9.10	9.13	13.92	13.45	14.37	14.12

Table 5.1: Radial position and corresponding temperature of the ν_x neutrinospheres obtained by Hannah Yasin's code using the HR structure factor [51] as well as the OPE, T-matrix, and EM 500 tables we provided.

5.2 Impact Estimate on Neutrino Emission and the Cooling of the Proto-Neutron Star

Post-processing cannot change the dynamics or thermodynamic conditions of the simulation. However, using the detailed rates in a full simulation is challenging. In collaboration with Robert Bollig and Thomas Janka from the Max Planck Institute for Astrophysics in Garching, we calculate and employ an analytical correction factor to the HR rates. Results have been published in Ref. [164].

5.2.1 Analytical Correction Factor

For a first estimate of the impact the findings described in Chapter 4 will have on proto-neutron-star cooling and neutrino emission, we calculate an analytical correction factor,

$$r_{Y_e}(\rho) \equiv \frac{\left\langle \lambda^{-1} \right\rangle (\rho, Y_e, T(\rho))}{\langle \lambda^{-1} \rangle_{\text{OPEnn}} (\rho, T(\rho))} \,, \tag{5.4}$$

of the opacity based on the partial-wave-expanded structure factor (4.50) with the T-matrix potential (3.15, 3.16) relative to the one-pion-exchange neutron-only (OPEnn) results conceptually similar to Hannestad and Raffelt. In this first step, the correction factor is a function of density ρ only. The temperature T is parametrized according to Eq. (2.44). The electron fraction Y_e is taken as a parameter that only takes fixed values.

The inverse mean-free path is averaged over Boltzmann distributed neutrino and antineutrino spectra. Both the T-matrix and OPEnn results are calculated using the formalism discussed in Ref. [149], which assumes non-degenerate conditions. Our results are then fit by a function of the form $r(\rho) = a \ln(\rho) + 10^{10}/\rho^b + c$, where ρ is given in g cm^{-3}.

High-density rates are needed in the simulation, but beyond nuclear saturation density, neutrinos are trapped and therefore reactions are in equilibrium. In addition, our formalism breaks down at high densities. As we do not expect r to go to 0, beyond $2.8 \times 10^{14}\,\text{g cm}^{-3}$ (about nuclear saturation density) we extrapolate our results with a constant, $r(\rho \geq \rho_0) = 0.14$. While the choice is not well constrained, it is not expected to impact the simulation due to the equilibrium conditions. We show the fit parameters in Table 5.2 and a visual comparison of our data points with fits in Figure 5.5. We note that the fit is far less sensitive than the number of digits in Table 5.2 suggests. Nevertheless, these are the parameters implemented in the simulation.

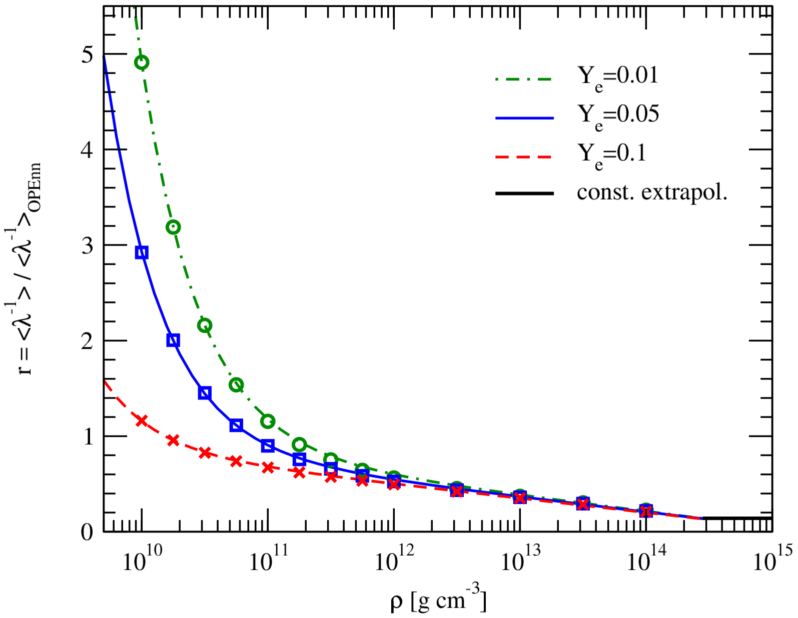

Figure 5.5: Calculated correction factors r (symbols) and fit results (lines) for $Y_e = 0.01, 0.05,$ and 0.1 as a function of density. Also shown is the constant extrapolation beyond nuclear saturation density.

Y_e	a	b	c	used in Y_e range
0.01	-0.0649830	1.0446877	2.2954877	≤ 0.05
0.05	-0.0685806	0.9680116	2.4176686	$0.05 - 0.1$
0.1	-0.0726502	0.9395710	2.5558616	≥ 0.1

Table 5.2: Fit parameters obtained for the three different Y_e values. Shown in the last column is the Y_e range for which a radial zone in the simulation uses the corresponding parameters.

5.2.2 Numerical Setup

The supernova simulations are performed by the Garching group using the PROMETHEUS-VERTEX code [165] in the one-dimensional version and the set of neutrino reactions as described in Refs. [53, 145, 165]. Proto-neutron star convection is taken into account by a mixing-length treatment. Two simulations are done for a $27\,M_\odot$ progenitor (model s27.0; [166]) with the LS 220 equation of state [55], one with the original HR bremsstrahlung rates from Ref. [51] and one taking into account our correction factor. Depending on the Y_e of the radial zone, one of our three fits is used, see Table 5.2.

The chosen progenitor does not explode in spherical symmetry. Therefore, the explosion was artificially triggered at 500 ms post-bounce by reducing the pre-shock density by a scaling factor. Between 500 and 2 500 km radius, a linearly increasing scaling factor was used, i. e., 1 at 500 km, 15 at 1 500 and 30 at 2 500 km. Beyond 2 500 km the factor was kept constant at 30. This lowers the mass-accretion rate, thus facilitating the explosion.

In addition, a $9.6\,M_\odot$ progenitor with the SFHo equation of state [167] was simulated, showing effects similar to the $27\,M_\odot$ simulation. In this thesis, we will only discuss the $27\,M_\odot$ progenitor. Additional details can be found in Refs. [53, 164].

As multi-dimensional effects are known to have a strong influence on the explosion dynamics, a one-dimensional simulation is not sufficient to evaluate the impact of our correction factor on the explosion mechanism. We will therefore concentrate our discussion on differences occuring during the cooling phase of the proto-neutron star.

5.2.3 Post-Processing Opacities

Before discussing the impact of the correction factor on the cooling of the proto-neutron star and on neutrino emission, we can evaluate the quality of our approximation by post-processing the radial profiles obtained in the simulation and comparing the corrected HR results with the full T-matrix results. We use the reference simulation with the unmodified HR rate.

We show the density along these profiles in Figure 5.7 and the comparison of inverse mean-free paths for a neutrino with $E = \langle E_{\nu_x} \rangle$ against pair absorption in Figure 5.6, assuming a Fermi-Dirac distribution for the antineutrino. Here, $\langle E_{\nu_x} \rangle$ is the local mean neutrino energy of muon/tau neutrinos and is part of the profile exported from the simulation. The plot range is determined by the radius where the density drops below $10^{10}\,\mathrm{g\,cm^{-3}}$. The ν_x neutrinosphere position (for the sum of absorption, inelastic scattering and pair absorption processes) is indicated by the green vertical line and we define it by the radius where the optical depth of a neutrino with local mean energy becomes smaller than one.

Ideally, the blue lines showing the approximated and full T-matrix result should lie on top of each other. Looking at the earlier profiles up to 1 s, we find good agreement between the two lines over a wide density range and especially around the neutrinosphere where the rates are most relevant.

We do find deviations, however, at small and large radii. The former can be attributed to degeneracy effects, which are neither included in our non-degenerate T-matrix formalism nor in the OPEnn calculations used to fit the correction factor, but they are taken into account by the HR rate. The black solid lines show the ratio of the temperature over the Fermi temperature, T/T_F, as an indicator of the degeneracy. Deviations appear where this value is significantly below 1. No formalism has been derived yet to calculate bremsstrahlung rates in mixtures of protons and neutrons at degenerate conditions using modern potentials. Nevertheless, we can use the formalism developed in Refs. [47, 148] to calculate T-matrix opacities in pure neutron matter under degenerate conditions (in the region where $T/T_\mathrm{F} < 1/\pi$). This can explain some of the discrepancy, but the original HR result still lies closer to the T-matrix opacities than the corrected one. This is partly a result of the HR issues discussed in Section 4.4.

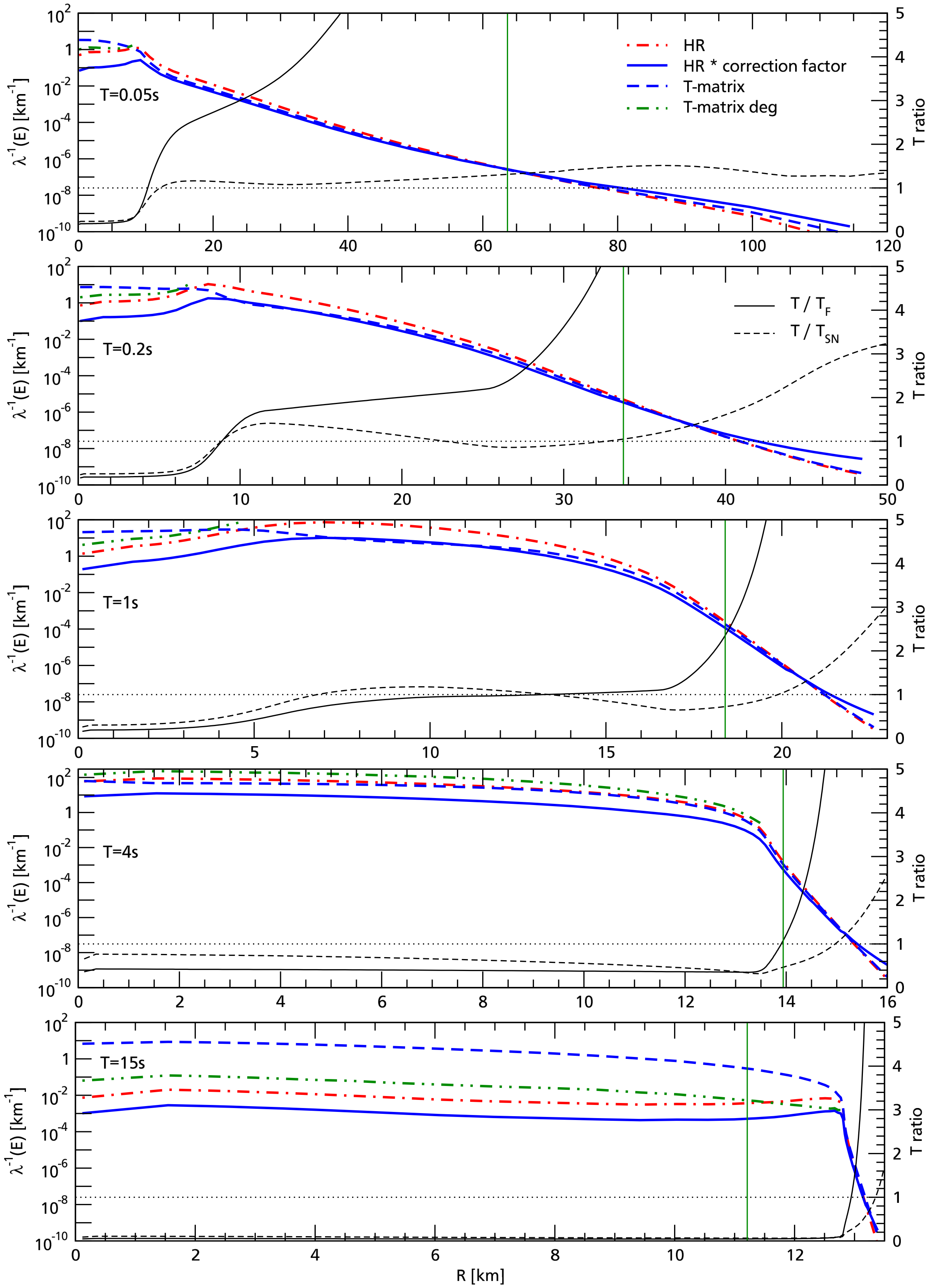

Figure 5.6: Inverse mean-free path against pair absorption for a ν_x with local mean energy as a function of radius along profiles at $50\,\mathrm{ms}$, $200\,\mathrm{ms}$, $1\,\mathrm{s}$, $4\,\mathrm{s}$, and $15\,\mathrm{s}$. Shown is the opacity used in the simulation (HR · correction factor, blue solid line) along with the HR (red dash-dotted line) and T-matrix (blue dashed line) opacities. For comparison, we also show degenerate T-matrix results calculated in pure neutron matter (green dash-dot-dotted line). The black solid line shows the degeneracy T/T_F, the black dashed line shows T/T_SN (cf. Eq. (2.44)). The green vertical line indicates the position of the ν_x neutrinosphere.

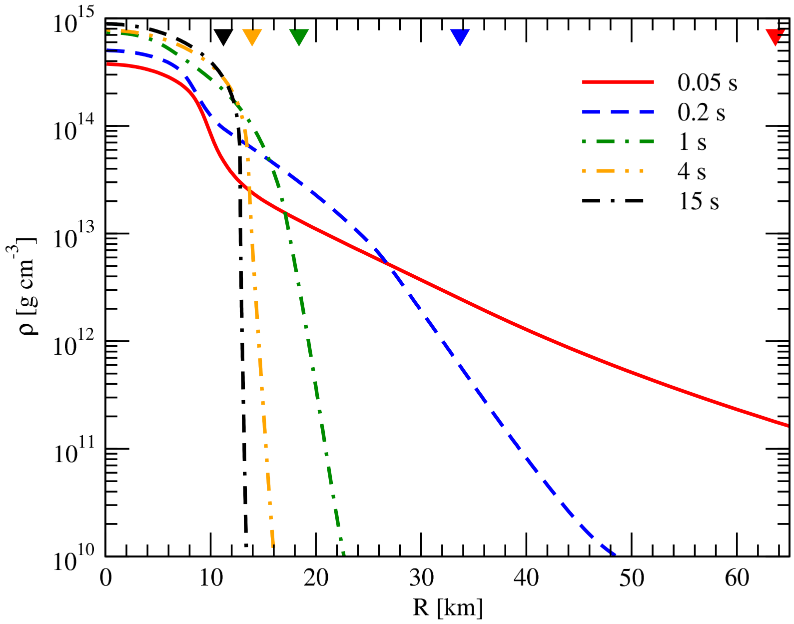

Figure 5.7: Density profiles of the timesteps shown in Fig. 5.6, i. e., at 50 ms (red solid line), 200 ms (blue dashed line), 1 s (green dash-dotted line), 4 s (orange dash-dot-dotted line), and 15 s (black dash-dash-dotted line) after bounce. The colored triangles indicate the position of the ν_x neutrinosphere at the corresponding time.

The deviations found at small densities in the outer regions can be attributed to temperature effects. Our fit factor is a one-dimensional function of density, assuming temperature to be parametrized by $T_{\mathrm{SN}}(\rho)$ given by Eq. (2.44). We plot T/T_{SN} along the profiles in Figure 5.6 and see significant deviations from unity especially in the core and at large radius. This contributes to the large deviations found at small radii.

At later times, the proto-neutron star has cooled and become highly degenerate. In the outer regions, our approximation still works fine, while in the center, degeneracy effects lead to huge deviations between our non-degenerate T-matrix results and the corrected HR opacities. As expected, this is significantly reduced when using the degenerate T-matrix rate instead. However, the discrepancies remain sizable.

Since neutrinos are in equilibrium in the high-density regions of the proto-neutron star interior and free-streaming in the low-density outer regions, the intermediate region around the neutrinosphere is most important for both the cooling of the proto-neutron star and the neutrino signal. In this region our approximation works reasonably well, except for very late times when the neutrinospheres lie inside the degenerate proto-neutron star. Furthermore, our corrected HR result tends to overestimate the effects and hence can be considered an upper bound on the effect size for this first sensitivity test.

5.2.4 Simulation Results

Above densities of $\rho \approx 10^{11}\,\mathrm{g\,cm^{-3}}$, the correction factor is smaller than one (see Fig. 5.5), so both the absorption opacity for pair annihilation and the production rate of neutrino-antineutrino pairs by the bremsstrahlung process are reduced. This mainly affects heavy-lepton neutrinos, as electron neutrinos also interact via charged-current reactions. There is no significant effect on the diffusion time scale of the neutrinos, because the total opacity is dominated by neutral-current neutrino-nucleon reactions and pair absorption only plays a negligible role (cf. Fig. 5.3).

The reduced emission of ν_x due to our effective T-matrix rates (i. e., the HR rates multiplied by the correction factor of Eq. (5.4)) reduces the cooling rate, increasing the temperature both in the interior of the neutron star and at the radius where $\rho = 10^{11}\,\mathrm{g\,cm^{-3}}$ (Figure 5.8). The cooling time is slightly increased by about $0.5-1$ s.

The reduction in the muon and tau neutrino luminosity compared to the unaltered HR rates is visible in Figure 5.9, where we show the luminosities for the different neutrino species as they appear to an observer at infinity and evaluated at 500 km radius. Electron-neutrino and antineutrino luminosities are slightly higher with our modified rate (up to 4 %) and seem to transport some of the energy that muon and tau neutrinos carry in the unmodified case. This is not caused directly by the bremsstrahlung modification as $\nu_e, \overline{\nu}_e$ emission is dominated by charged-current processes. Instead, it is a consequence of the increased temperatures. The total luminosity is slightly reduced.

In addition, the modified rate affects neutrino energies. In Figure 5.9 we also show the mean neutrino energy for an observer at infinity evaluated at 500 km as a function of time. All mean energies are increased with the modified rate. For heavy-lepton neutrinos, this is consistent with a reduced opacity, moving the energy sphere to smaller radii and consequently higher temperatures. For electron-type neutrinos, the effect is again mostly indirect, caused by the increased temperature. The energy differences grow with time and are largest for the electron antineutrino, with $\Delta \left\langle E_{\overline{\nu}_e} \right\rangle = 0.7\,\mathrm{MeV}$ at $t = 4\,\mathrm{s}$ after bounce. This in turn slightly reduces the electron fraction ($\Delta Y_e < 0.01$).

The gradual growth of differences in the neutrino emission with time is mostly caused by the thermal evolution of the proto-neutron star, which diverges more and more between the two simulations as the time-integrated effects of the two bremsstrahlung rates accumulate.

The reduction of the bremsstrahlung rates by a factor of $2-5$ in the density region where the ν_x neutrinospheres are located during most of the cooling evolution of the proto-neutron star (between 10^{12} and $10^{14}\,\mathrm{g\,cm^{-3}}$) only affects ν_x luminosities at the 5 % level. The increased temperatures power higher $\nu_x \overline{\nu}_x$ production through $e^{\pm}$ and $\nu_e \overline{\nu}_e$ pair annihilation that compensate the effects. The local differences are much larger, but they only lead to small global changes due to these feedback mechanisms. The effects we find occur too late to likely have a significant impact on the explosion dynamics.

Our approximation provides a first estimate on the impact that bremsstrahlung models with modern nuclear potentials have on the cooling evolution of the proto-neutron star and the neutrino emission. We find small changes compared to the description by Hannestad and Raffelt, thus providing support for all simulations being done based on their formalism. All effects are attributed to the high-density differences. In this density region, T-matrix and chiral EFT based opacities agree (see Fig. 4.7), thus similar findings are expected for an impact estimate based on chiral potentials.

To improve on our approximation, temperature needs to be taken into account explicitly. A simple correction factor is then probably not as straight-forward to obtain. For a more detailed study, tabulated structure factors similar to

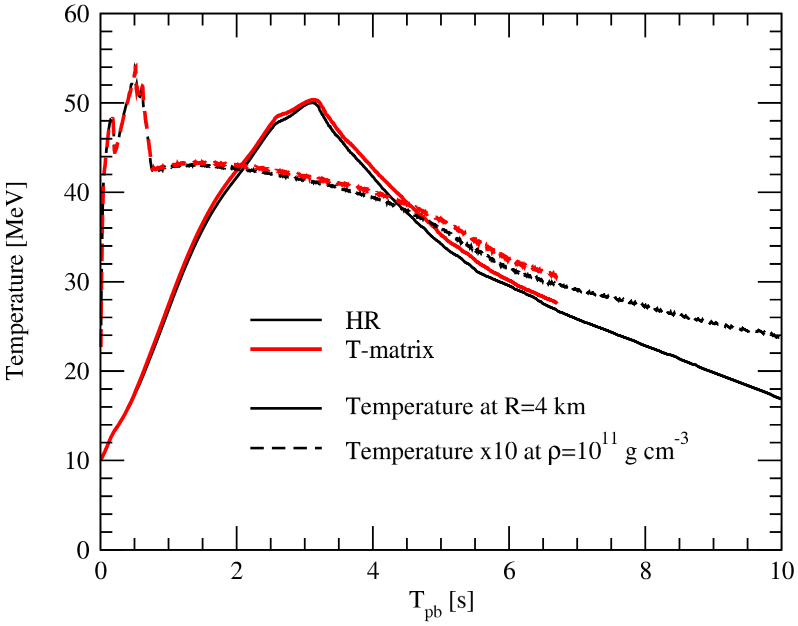

Figure 5.8: Temperature at a radius of 4 km (solid lines) and at $\rho = 10^{11}\,\mathrm{g\,cm^{-3}}$ (dashed lines) as a function of time after bounce for the simulations using the unmodified HR rate (black lines) and the effective T-matrix rate (red lines). The temperature at $\rho = 10^{11}\,\mathrm{g\,cm^{-3}}$ has been multiplied by a factor of ten to fit on the same scale.

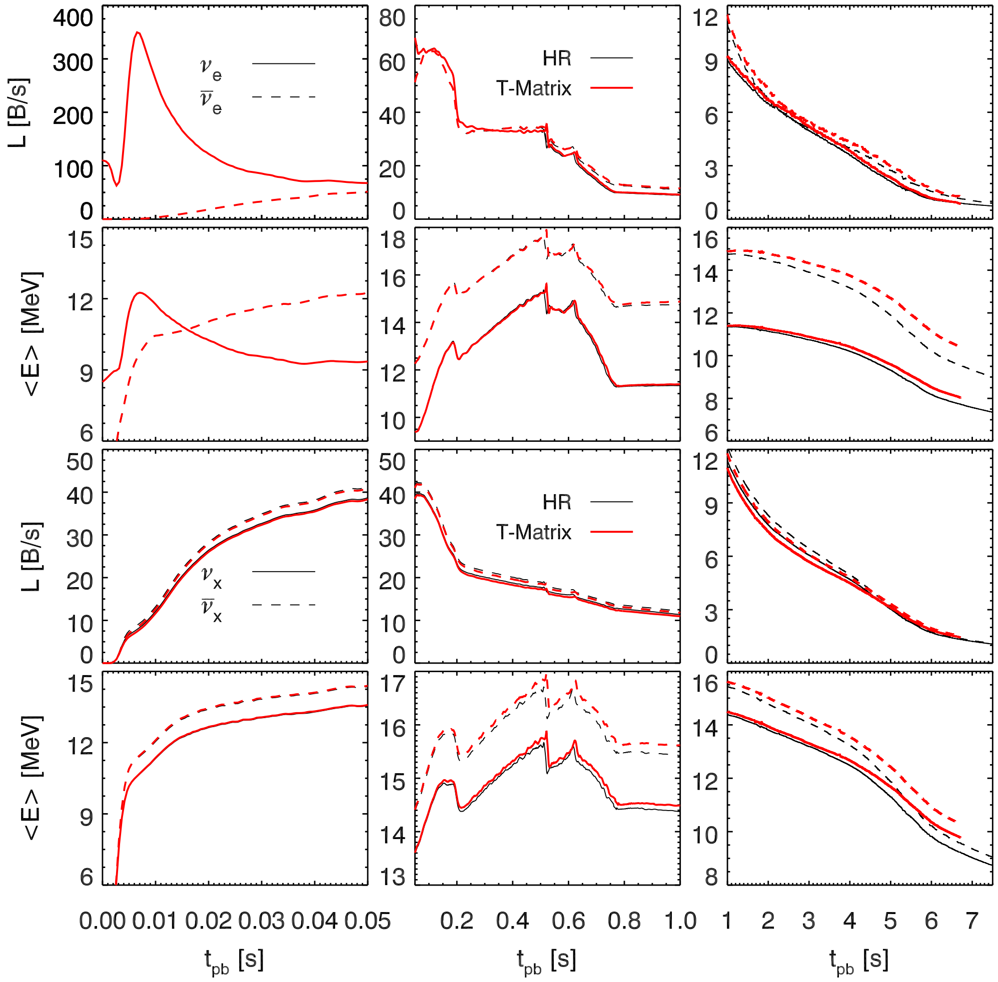

Figure 5.9: Neutrino signal as a function of time after bounce for the simulations with the unmodified HR rate (black lines) and the effective T-matrix rate (red lines). Shown is the luminosity (first and third row) and mean energy, both evaluated at 500 km radius and for an observer in the lab frame at infinity. The top (bottom) two rows show electron-type (heavy-lepton) neutrinos, where neutrinos are represented by solid and antineutrinos by dashed lines. Plot provided by Robert Bollig.

Section 5.1 should be used. In addition, an interpolation is required between our degenerate and non-degenerate formalism, which also necessitates a degenerate structure-factor formalism in mixtures of protons and neutrons.

6 Neutrino Scattering on Interacting Nucleons

Unlike scattering on free nucleons, scattering reactions on interacting nucleons ($N+N+\nu\rightarrow N+N+\nu$) are not included in current supernova simulations. Without nuclear interactions, energy transfer is limited to recoil, which is small due to the large nucleon mass. In this chapter, we derive an approximate expression for the structure factor that includes both recoil/momentum transfer and nuclear interactions and show results for the inverse mean-free path and the energy transfer per collision. We compare our results to recoil-only calculations in collaboration with Maria Voskresenskaya.

The results discussed in this chapter will be published in Ref. [168].

6.1 Scattering Formalism

The root-mean-square energy transfer per scattering collision is given by [148]

$$\Delta E = \sqrt{\frac{\langle (E_\nu - E_\nu')^2\rangle}{\langle (E_\nu - E_\nu')^0\rangle}}\,, \tag{6.1}$$

where $\langle (E_\nu - E_\nu')^l\rangle$ are the energy-exchange moments defined as the integral over neutrino energies weighted by the scattering rate $\Gamma(\omega,\boldsymbol{q})$ [169]:

$$\langle (E_\nu - E_\nu')^l\rangle = \int \frac{\mathrm{d}^3 p_\nu'}{(2\pi)^3}\,(E_\nu - E_\nu')^l\,\Gamma(\omega,\boldsymbol{q})\,. \tag{6.2}$$

Here, E_ν and E_ν' are the energies of the incoming and outgoing neutrino respectively, $\boldsymbol{q}=\boldsymbol{q}_\nu - \boldsymbol{q}_\nu'$ is the momentum transfer and $\omega = E_\nu - E_\nu'$ is the energy transfer. The axial part of the scattering rate is given by

$$\Gamma(\omega,\boldsymbol{q}) = 2\pi\, n\, G_\mathrm{F}^2\,(3-\cos\theta)\,S_A(\omega,\boldsymbol{q}) \tag{6.3}$$

and we neglect the vector part as we did in Chapter 4.

If S_A depends only on the magnitude of $\boldsymbol{q}$, the integral in Eq. (6.2) can be performed in terms of ω and $q=|\boldsymbol{q}|$ using the following relation obtained from kinematics:

$$\mathrm{d}^3 p_\nu' = 2\pi\, q\,\frac{E_\nu'}{E_\nu}\mathrm{d}\omega\,\mathrm{d}q\,. \tag{6.4}$$

Since E_ν' ranges from 0 to ∞, the limits of ω are $-\infty$ and E_ν. The limits of q are obtained by inserting $\cos\theta=\pm1$ in Eq. (2.28), hence $|\omega| < q < 2E_\nu - \omega$. The same relation can be used to express $\cos\theta$ in terms of E_ν, ω, and q.

Hence, the energy-exchange moments can be written as

$$\langle (E_\nu - E_\nu')^l\rangle = \frac{G_\mathrm{F}^2\, n}{2\pi}\int\limits_{-\infty}^{E_\nu}\mathrm{d}\omega\,\frac{E_\nu-\omega}{E_\nu}\,\omega^l\int\limits_{|\omega|}^{2E_\nu-\omega}\mathrm{d}q\,q\,(3-\cos\theta)\,S_A(\omega,q)\,. \tag{6.5}$$

The energy-dependent inverse mean-free path against scattering is equal to the zeroth energy-exchange moment,

$$\lambda^{-1}(E_\nu) = \langle (E_\nu - E_\nu')^0\rangle\,, \tag{6.6}$$

where we assume that final-state Pauli blocking for the neutrinos can be neglected.

We can compare our results for interacting nucleons to free nucleon recoil using the recoil structure factor S_A^R from Ref. [48]:

$$S_A^R(\omega, q) \;=\; \frac{C_A^2\, m^2\, T}{2\pi^2\, n\, q}\, \frac{1}{1-e^{-\omega/T}} \left(\frac{\omega}{T} + \ln \frac{1+\exp[(\epsilon_- - \mu)/T]}{1+\exp[(\epsilon_- + \omega - \mu)/T]} \right) \tag{6.7}$$

$$\overset{\text{non-deg}}{\approx} \frac{C_A^2\, m^2 T}{2\,\pi^2\, n\, q} \exp\left[\frac{\mu - \epsilon_-}{T} \right] , \tag{6.8}$$

with temperature T, nucleon mass m, nucleon chemical potential μ, and

$$\epsilon_- = \frac{p_-^2}{2m} = \frac{m}{2q^2} \left(\omega - \frac{q^2}{2m} \right)^2 \tag{6.9}$$

is the minimum energy a nucleon needs to have to accept momentum q and energy ω [27]. Equation (6.7) is the general expression. In the non-degenerate limit, $\mu/T \ll -1$ and a leading-order expansion of the logarithm yields the expression in Eq. (6.8).

Inside the neutrinosphere, neutrinos are in thermal equilibrium with matter and their energy is distributed around a typical value of $E_\nu \approx 3\,T$. In this chapter we will also look at lower-energy neutrinos, which are less common and thus less important for the supernova dynamics. This allows us to study how different parts of the neutrino spectrum are sensitive to recoil and collision effects.

6.2 Structure-Factor Formalism Beyond the Long-Wavelength Limit

The same structure factor governs bremsstrahlung, pair absorption and scattering reactions. However, the structure factor in Section 4.1 is derived in the long-wavelength limit ($\boldsymbol{q} \to 0$), i. e., momentum transfer between the neutrino and the nucleons it scatters off is neglected. Therefore, in order to include recoil in νNN scattering reactions, the $\boldsymbol{q}$-dependent structure factor has to be derived. In pure neutron matter it is given by [47]

$$S_A(\omega, \boldsymbol{q}) = C_A^{n\,2}\, S_\sigma(\omega, \boldsymbol{q}) = C_A^{n\,2}\, \frac{1}{\pi n}\, \frac{1}{1-e^{-\omega/T}}\, \mathrm{Im} \frac{X_\sigma}{1+g_0 X_\sigma} , \tag{6.10}$$

with

$$X_\sigma = 2 \int \frac{\mathrm{d}^3 p}{(2\pi)^3}\, \frac{v_{\boldsymbol{p}} \cdot \boldsymbol{q} - i/\tau_\sigma}{\omega + i/\tau_\sigma - v_{\boldsymbol{p}} \cdot \boldsymbol{q}}\, \frac{\partial n(\epsilon_{\boldsymbol{p}})}{\partial \epsilon_{\boldsymbol{p}}} . \tag{6.11}$$

Here, τ_σ is the spin relaxation time, which is identical to τ_A in the formalism discussed in the previous chapter. The partial-wave-expanded expression is given in Ref. [57]. Further, X_σ is the response function in the absence of mean-field effects, g_0 is the Landau parameter for the spin-dependent part of the interaction introducing such mean-field effects, and $\partial n(\epsilon_{\boldsymbol{p}})/\partial \epsilon_{\boldsymbol{p}}$ is the partial derivative of the Fermi distribution function with respect to the kinetic energy $\epsilon_{\boldsymbol{p}} = \boldsymbol{p}^2/(2m^*)$.

In the degenerate limit, X_σ can be written as [47]

$$X_\sigma^D = N(0) \left[1 - \frac{\omega}{2 v_\mathrm{F} q} \ln \left(\frac{\omega + i/\tau_\sigma + v_\mathrm{F} q}{\omega + i/\tau_\sigma - v_\mathrm{F} q} \right) \right] , \tag{6.12}$$

where $N(0) = m^* k_\mathrm{F}/\pi^2$ is the density of states at the Fermi surface, $v_\mathrm{F} = k_\mathrm{F}/m^*$ is the Fermi velocity and k_F the Fermi momentum. The limit of vanishing interactions ($\tau_\sigma \to \infty$) of this expression matches the degenerate structure factor for recoil in Refs. [48, 168].

To generalize Equation (6.12) to non-degenerate conditions, we start with Equation (6.11). We then approximate the velocity $v_{\boldsymbol{p}}$ by the thermal velocity $v_\mathrm{th} = \sqrt{3T/m}$ and assume a Boltzmann distribution function for $n(\epsilon_{\boldsymbol{p}})$. Equation (6.11) then becomes

$$X_\sigma^{ND} = 2 \int \frac{\mathrm{d}^3 p}{(2\pi)^3}\, \frac{v_\mathrm{th} q \cos\theta - i/\tau_\sigma}{\omega + i/\tau_\sigma - v_\mathrm{th} q \cos\theta} \left(- \frac{\exp(\frac{-\epsilon-\mu}{T})}{T} \right) \tag{6.13}$$

$$= \left[1 - \frac{\omega}{2 v_\mathrm{th} q} \ln \left(\frac{\omega + i/\tau_\sigma + v_\mathrm{th} q}{\omega + i/\tau_\sigma - v_\mathrm{th} q} \right) \right] \frac{1}{T}\, \underbrace{\frac{1}{\pi^2} \int \mathrm{d}p\, p^2 \exp\left(\frac{-\epsilon-\mu}{T} \right)}_{=n} . \tag{6.14}$$

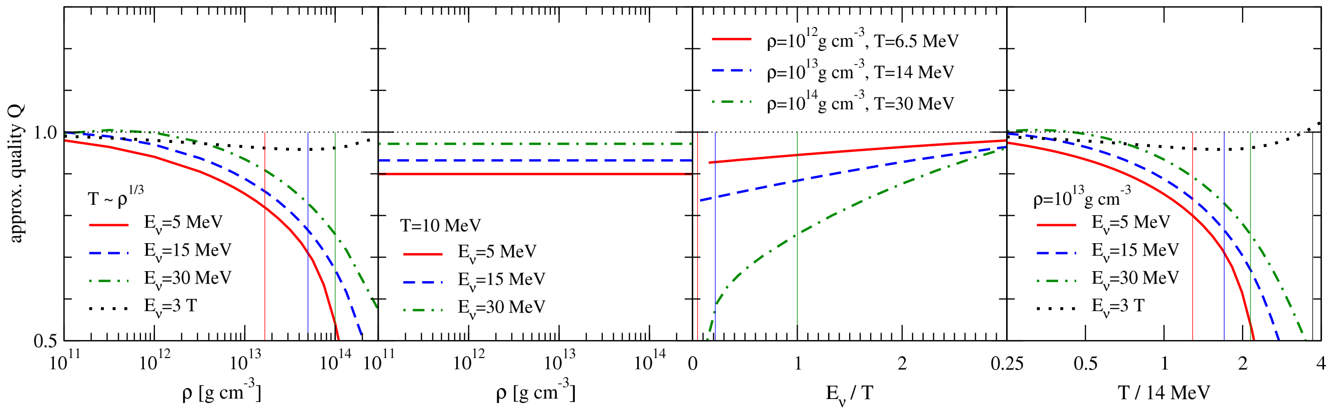

Figure 6.1: Quality of our approximation, i. e., ratio of the energy transfer calculated with the NN structure factor in the collisionless limit (6.20) and the non-degenerate nucleon-recoil structure factor (6.8) for several conditions discussed in this chapter. The colored vertical lines indicate the point where $E_\nu/T = (T/30\,\mathrm{MeV})^2$ (see text).

Our result for X_σ in the non-degenerate limit has the same form as in Eq. (6.12), but with the Fermi velocity v_F replaced by the thermal velocity v_th and $N(0)$ replaced by the density of states according to the Curie law, $\chi^0 = n/T$. In this formalism, mean-field effects are controlled by g_0. We neglect them in our exploratory study, hence g_0 is set to 0. The structure factor for non-degenerate conditions is then given by

$$S_\sigma(\omega,\boldsymbol{q}) = -\frac{\omega}{2\pi v_\mathrm{th} q T}\,\frac{1}{1-e^{-\omega/T}}\,\mathrm{Im}\left[\ln\left(\frac{\omega+i/\tau_\sigma+v_\mathrm{th}q}{\omega+i/\tau_\sigma-v_\mathrm{th}q}\right)\right]. \tag{6.15}$$

To calculate the limit of vanishing interactions, we use

$$\ln z = \ln|z| + i\arg z \quad\Rightarrow\quad \mathrm{Im}(\ln z) = \arg z \tag{6.16}$$

and find

$$\mathrm{Re}\,z = \frac{\omega^2 + {}^1\!/_{\tau_\sigma}{}^2 - (v_\mathrm{th}q)^2}{(\omega - v_\mathrm{th}q)^2 + {}^1\!/_{\tau_\sigma}{}^2} \approx \frac{\omega^2 - (v_\mathrm{th}q)^2}{(\omega - v_\mathrm{th}q)^2} + \mathcal{O}\left({}^1\!/_{\tau_\sigma}{}^2\right), \tag{6.17}$$

$$\mathrm{Im}\,z = -\frac{2v_\mathrm{th}q\,{}^1\!/_{\tau_\sigma}}{(\omega - v_\mathrm{th}q)^2 + {}^1\!/_{\tau_\sigma}{}^2} \approx -\frac{2v_\mathrm{th}q}{\tau_\sigma(\omega - v_\mathrm{th}q)^2} + \mathcal{O}\left({}^1\!/_{\tau_\sigma}{}^2\right). \tag{6.18}$$

Furthermore, since $\mathrm{Im}\,z < 0$,

$$\arg z = \begin{cases} \arctan\left(\frac{\mathrm{Im}\,z}{\mathrm{Re}\,z}\right) & \text{if } \mathrm{Re}\,z > 0 \Leftrightarrow |\omega| > v_\mathrm{th}q\,, \\ \arctan\left(\frac{\mathrm{Im}\,z}{\mathrm{Re}\,z}\right) - \pi & \text{otherwise}\,, \end{cases} \tag{6.19}$$

and $\arctan\left(\frac{\mathrm{Im}\,z}{\mathrm{Re}\,z}\right) \to 0$ for $\tau_\sigma^{-1} \to 0$. Thus the structure factor is only non-zero for $|\omega| < v_\mathrm{th}q$ and we can express the structure factor in terms of the Heaviside function $\Theta(x)$ as

$$S_\sigma(\omega,\boldsymbol{q}) \underset{\tau_\sigma\to\infty}{=} \frac{\omega}{2v_\mathrm{th}qT}\,\frac{1}{1-e^{-\omega/T}}\,\Theta\left(1 - \frac{|\omega|}{v_\mathrm{th}q}\right). \tag{6.20}$$

Inserting Eq. (6.20) into Eq. (6.5), expressing θ in terms of E_ν, ω and q, and combining the Heaviside function with the integration limits, we obtain the following expression for the collisionless limit of the energy-exchange moments:

$$\begin{aligned}\langle(E_\nu - E_\nu')^l\rangle_\text{coll.less} = {}& \frac{G_\mathrm{F}^2 C_A^{n\,2}}{4\pi}\,\frac{n}{v_\mathrm{th}T}\int_{\frac{2E_\nu}{1-1/v_\mathrm{th}}}^{\frac{2E_\nu}{1+1/v_\mathrm{th}}} \mathrm{d}\omega\,\frac{E_\nu - \omega}{E_\nu}\,\omega^{l+1}\,\frac{1}{1-e^{-\omega/T}} \\ & \times\left[\left(3 - \frac{E_\nu^2 + (E_\nu-\omega)^2}{2E_\nu(E_\nu-\omega)}\right)\left(2E_\nu - \omega - \frac{|\omega|}{v_\mathrm{th}}\right) + \frac{1}{6E_\nu(E_\nu-\omega)}\left((2E_\nu-\omega)^3 - \frac{|\omega|^3}{v_\mathrm{th}{}^3}\right)\right].\end{aligned} \tag{6.21}$$

Comparing this result to a literature recoil structure factor, we can estimate the quality of our approximation (see Figure 6.1). We define a measure of the approximation quality Q as the ratio between the energy transfer in the collisionless limit of the interacting case given by Eq. (6.21) and using the non-degenerate recoil structure factor in Eq. (6.8).

The approximation works better at higher neutrino energies and has a strong dependence on temperature. Since in deriving Eq. (6.15) we approximate the velocity distribution by a single velocity, it seems reasonable that this approximation gets worse with increasing temperature. However, our approximation works reasonably well for a wide range of thermodynamic conditions, including those most relevant for supernova simulations, thus allowing for a systematic discussion. Especially from the third panel in Figure 6.1, we can see that our approximation works well above a certain E_ν/T threshold and that this threshold will depend on temperature. One possible parametrization is $E_\nu/T > (T/30\,\mathrm{MeV})^2$, which we also indicate in the figure. Along the supernova conditions of Eq. (2.44), this corresponds to $E_\nu > 3\,\mathrm{MeV}(\rho/10^{13}\,\mathrm{g\,cm}^{-3})$. All conditions fulfilling this inequality show deviations below 25 %. In addition, the enhancements of the energy transfer due to NN interactions compared to recoil-only discussed in Section 6.4 are larger than the uncertainties suggested by Fig. 6.1.

6.3 Mean-Free Path

In Fig. 6.2 we present our results for the energy dependence of the inverse mean-free path (as defined in Eq. (6.6)) at different densities and temperatures. The temperatures chosen lie close to the line defined by Eq. (2.44). For

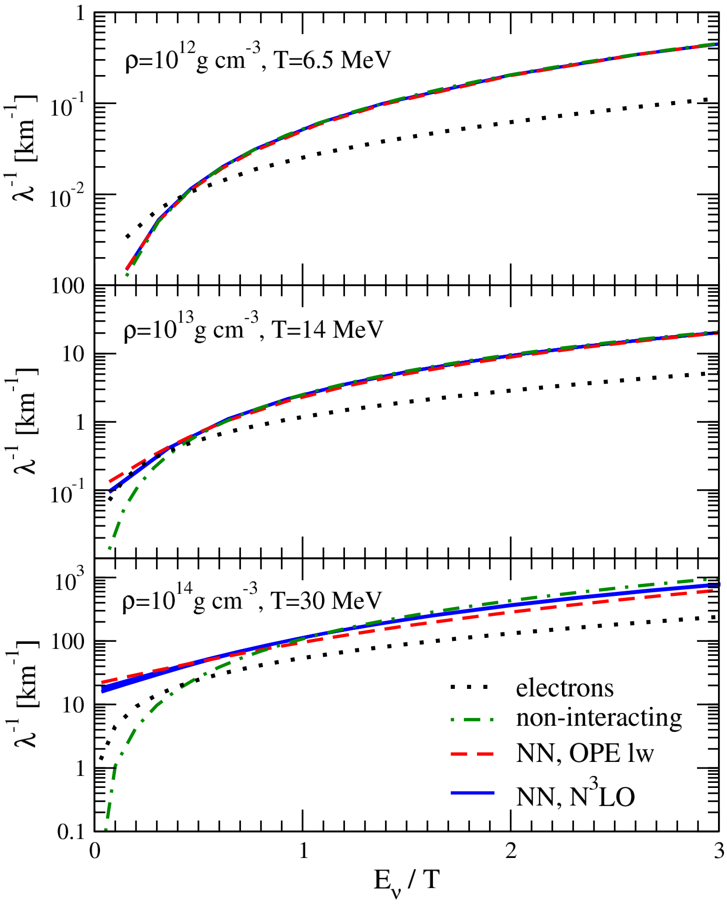

Figure 6.2: Inverse mean-free path of neutrinos against scattering on electrons (dotted black line), non-interacting (dash-dotted green line) and interacting (blue band) nucleons as a function of neutrino energies for various densities and corresponding temperatures. In addition to the chiral EFT results for interacting nucleons, we show results conceptually similar to the approach by Hannestad and Raffelt (OPE lw, see text; red dashed line).

comparison, we also include electrons in this section, assuming an electron fraction of $Y_e = 0.3$. Our electron results are based on the formalism in Ref. [170].

While the inverse mean-free path for neutrinos scattering on non-interacting nucleons is proportional to E_ν^2, the exponent for neutrino-electron scattering is smaller. Hence electrons dominate the absorption process compared to free nucleons at low neutrino energies.

Figure 6.2 shows a striking energy dependence of the effect of interactions at large densities: While interactions reduce the inverse mean-free path slightly for high-energy incoming neutrinos, they enhance it for 1 MeV neutrinos by two orders of magnitude. For non-interacting nucleons, the inverse mean-free path is set by the E_ν^2 dependence of the rates. Interactions lead to a broadening of the peak, with the width set by τ_A, which does not have a strong energy dependence. In particular, for non-interacting nucleons the outgoing neutrino has an energy distributed

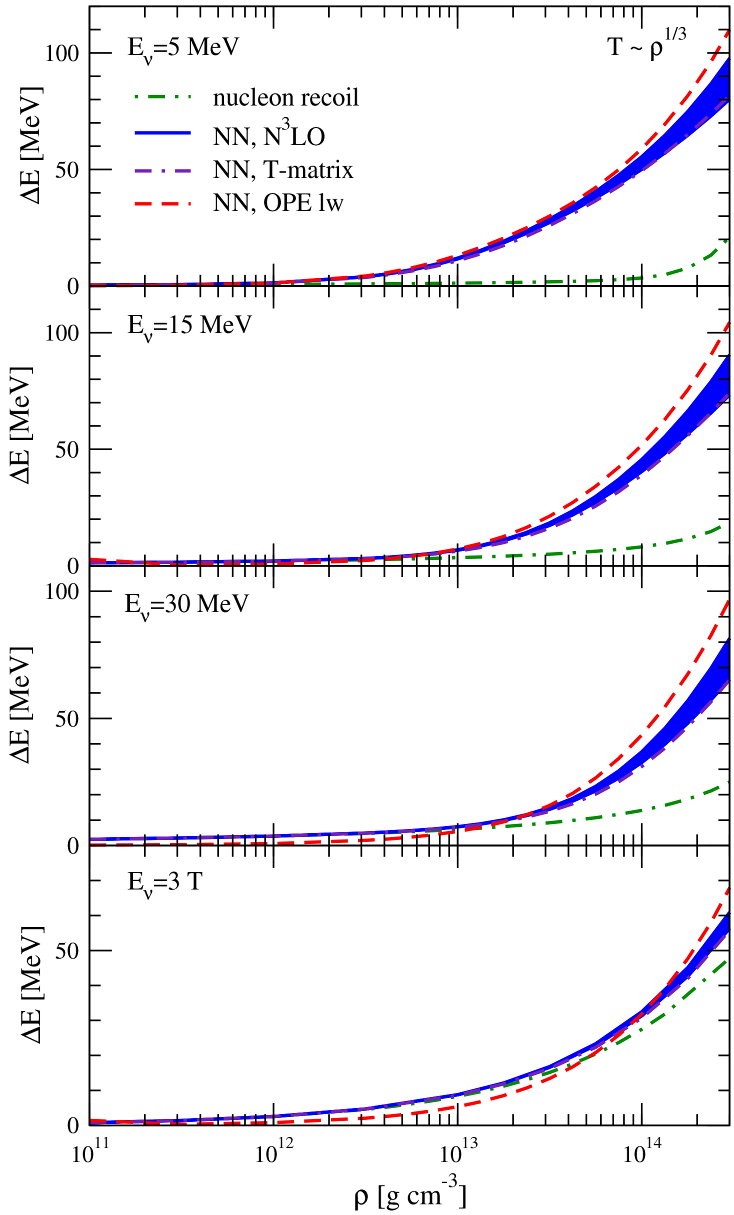

Figure 6.3: Energy transfer as a function of density for different neutrino energies showing non-degenerate nucleon recoil (green dash-dotted line) as well as T-matrix (violet dash-dash-dotted line) and chiral EFT (blue band) results for interacting nucleons. We also show results conceptually similar to the approximations by Hannestad and Raffelt, i. e., using OPE and the long-wavelength limit (red dashed line). The temperature is assumed to be density dependent as defined in Eq. (2.44).

around the incoming neutrino energy, while interactions allow outgoing neutrino energies significantly larger than the incoming energy. This effect is much more important at low incoming energies.

We also show calculations conceptually similar to the approach by Hannestad and Raffelt [51], i. e., using the one-pion-exchange approximation and only considering the long-wavelength limit of the structure factor $S_A(\omega) = S_A(\omega, \boldsymbol{q} \to 0)$. They already noted in their paper that this treatment neglects recoil effects. In order to compare our results with estimates one would get based on their approach, we calculate the inverse mean-free path and energy transfer using the long-wavelength expressions for the structure factor in Ref. [57] (identical to the structure factor derived in Section 4.1 for $Y_e = 0$) rather than Eq. (6.15) and using OPE matrix elements. We stress again that these results differ from the values one would obtain using the analytical expressions for the structure factor provided in the HR paper, see Section 4.4.

In contrast to the energy transfer (see next section), the long-wavelength limit works fine for the mean-free path, as is evident from the OPE long-wavelength (lw) lines in Figure 6.2.

6.4 Energy Transfer

We calculate the energy transfer as defined in Eq. (6.1) in combination with Eq. (6.2). For nucleon recoil we use the non-degenerate limit of the structure factor given in Eq. (6.8). The structure factor for interacting nucleons is given in Eq. (6.15).

In Figure 6.3 we show the density dependence of the energy transfer assuming that temperature grows with density as parametrized by Eq. (2.44). Comparing nucleon recoil (green) and our full NN results (blue/purple), it is evident that interactions between nucleons are important for neutrino scattering, adding about 12–18 % to the energy transfer at 10^{14} g cm^{-3} for the typical neutrino energy $E_\nu = 3T$ of a thermalized neutrino distribution, and increasing the energy transfer very significantly at lower neutrino energies. It also becomes evident that for these low-energy neutrinos interactions already play an important role at relatively low densities of a few times

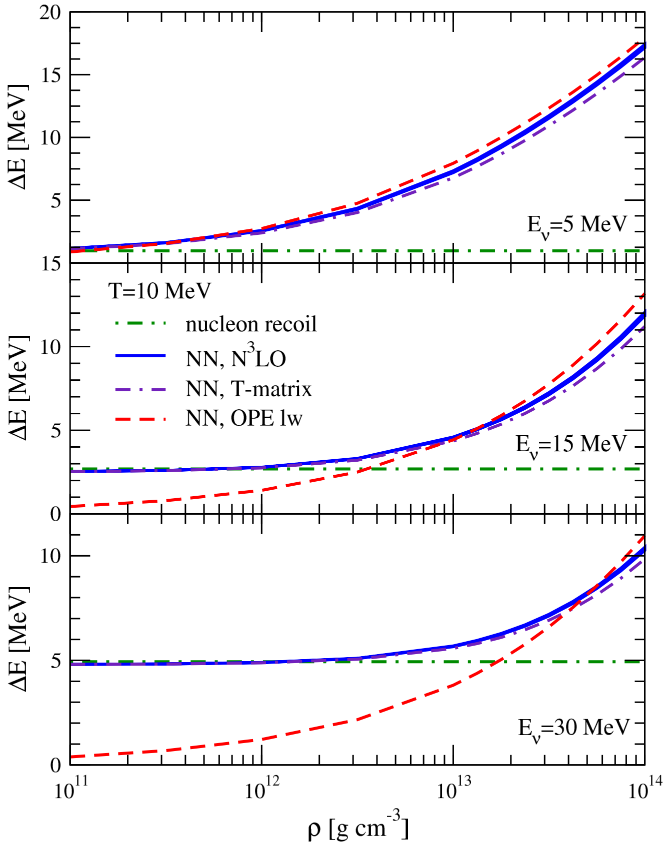

Figure 6.4: Energy transfer as a function of density at fixed temperature $T = 10\,\mathrm{MeV}$ and for $E_\nu = 5, 15, 30\,\mathrm{MeV}$. The lines are the same as in Fig. 6.4.

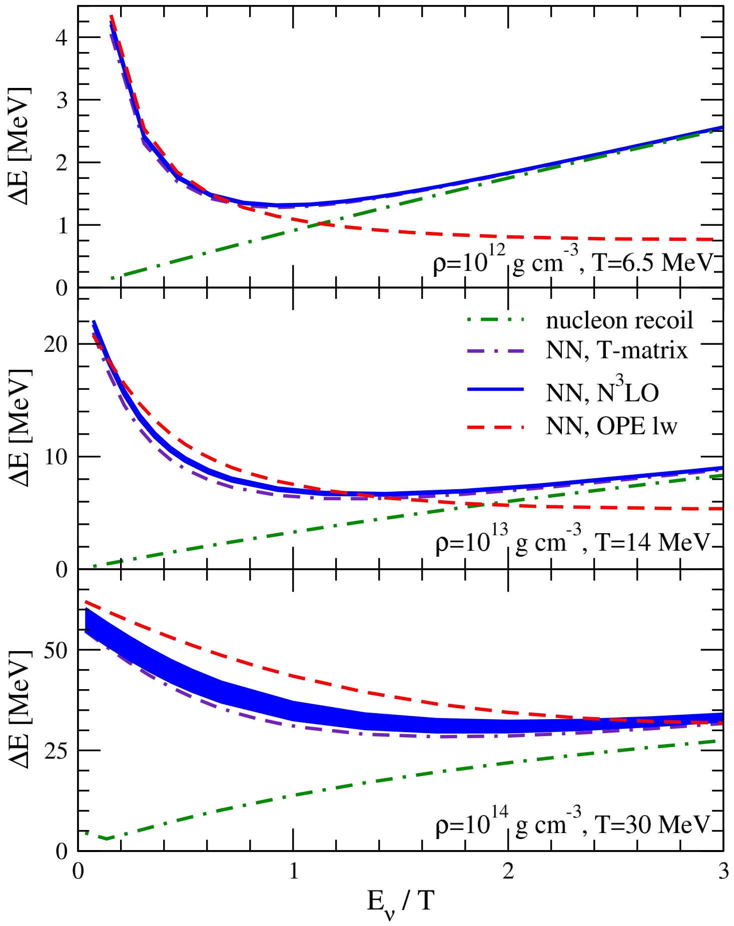

Figure 6.5: Energy transfer as a function of neutrino energy at fixed density and corresponding temperature for different points along Eq. (2.44). The lines are the same as in Fig. 6.4.

10^{12} g cm^{-3}, i. e., at typical neutrinosphere densities. Furthermore, since our NN results include recoil, the energy transfer is always at least as large as the recoil-only value, as one would expect.

Keeping the temperature fixed at $T = 10\,\mathrm{MeV}$ (Figure 6.4) and again varying the density eliminates the density-dependence of the recoil-only results, allowing for a discussion of interaction effects alone. One can clearly identify regions where the full calculation is dominated by recoil while others are dominated by interactions (use the red line as a proxy as the long-wavelength results do not include recoil). At low densities, our full NN results reproduce the recoil-only results up to a small difference caused by the approximations we employ (see Section 6.2 and Figure 6.1). This agreement is expected as interactions do not play a major role at these densities, where internucleon distances are large. Then, as density increases and interactions become important, the full energy transfer grows significantly, with a stronger effect for smaller neutrino energies, in agreement with Fig. 6.5.

At high densities, where interactions are more important than recoil, the long-wavelength approximation gives results comparable to our full calculation, with the OPE long-wavelength energy transfer usually larger than our chiral or T-matrix results. This is in agreement with earlier work in the long-wavelength limit [148], showing a smaller energy transfer with chiral interactions than with a one-pion-exchange potential. As Hannestad and Raffelt neglect recoil, the energy transfer goes to zero rather than the recoil-only value for decreasing density, which is why it was deemed less important at densities around the neutrinosphere. Our full treatment including recoil and nuclear interactions for the first time enables a consistent treatment of recoil and interaction effects that can be employed at all relevant densities.

From our discussion so far, it is evident that the energy of the incoming neutrino plays an important role especially for the ratio between full and recoil-only energy transfer. In Figure 6.5 we vary the energy of the incoming neutrino at three different densities and temperatures close to those defined by Eq. (2.44). While recoil dominates the energy transfer at high E_ν/T, interactions allow low-energy neutrinos scattering to high-energy states, thus allowing for

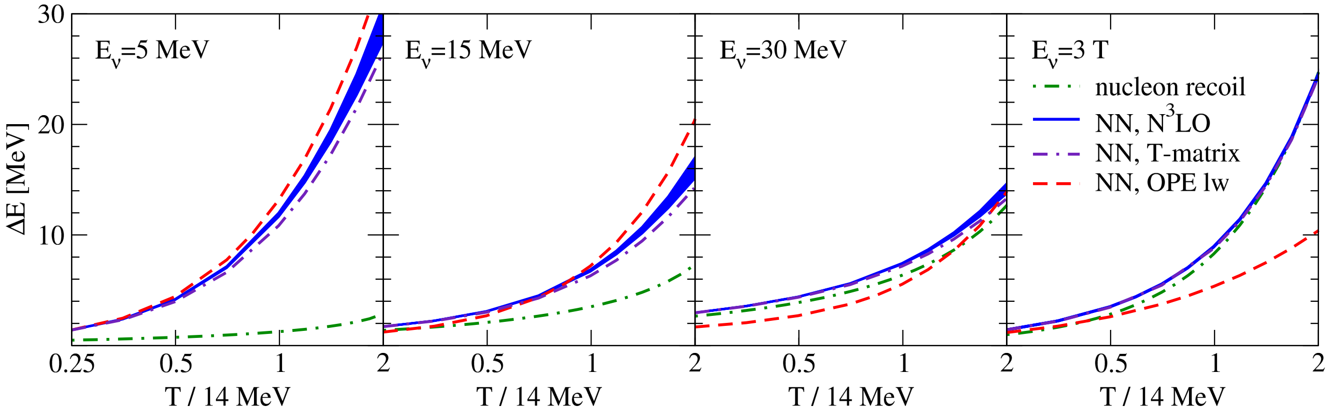

Figure 6.6: Energy transfer as a function of temperature at fixed density $\rho = 10^{13}\,\mathrm{g\,cm^{-3}}$ and for various neutrino energies.

very large energy transfers. This finding is valid for the whole density range, but the interaction-dominated energy range increases with temperature.

Finally, we investigate the temperature dependence of the energy transfer by setting the density to $10^{13}\,\mathrm{g\,cm^{-3}}$ and varying the temperature relative to the 14 MeV roughly corresponding to Eq. (2.44). As can be seen again in Figure 6.6, at high neutrino energies the full NN energy transfer is dominated by recoil, while at lower neutrino energies interactions dominate. There is a strong temperature dependence at low neutrino energies, meaning that the importance of interactions grows significantly if conditions are hotter than suggested by Eq. (2.44). Even for densities as low as $10^{12}\,\mathrm{g\,cm^{-3}}$, the effect of nuclear interactions can be substantial if temperatures are relatively high and neutrino energies sufficiently low, see Figure 6.7.

From the comparison of the energy transfers we see that for conditions relevant in supernovae it is important to account for interacting nucleons. The effect of nuclear interactions becomes larger with increasing density and temperature and is most important at low neutrino energies. The fraction of neutrinos at low energies might be too small to have a significant effect on explosion dynamics, but we do expect an effect of our findings on the low-energy part of the neutrino spectrum. This should be investigated in simulations.

While relaxation rates can be calculated in mixtures of protons and neutrons (see Chapter 4), the structure factor formalism in mixtures is only available in the long-wavelength limit. The approximation employed in Section 6.2 is based on a single species.

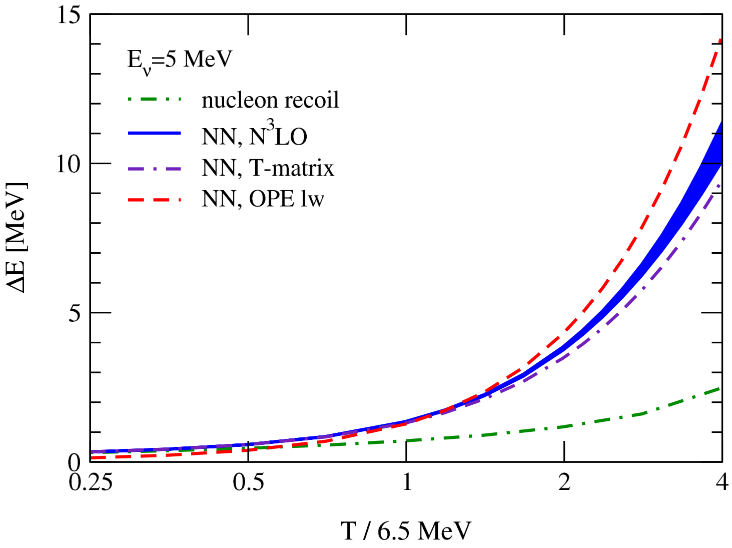

Figure 6.7: Energy transfer as a function of temperature at fixed density $\rho = 10^{12}\,\mathrm{g\,cm^{-3}}$ and for $E_\nu = 5\,\mathrm{MeV}$.

In all plots shown in this chapter, the T-matrix results are at the lower border or slightly below the chiral N^{3}LO band, compatible with previous findings in pure neutron matter [47, 57]. The large deviations between chiral and T-matrix results discussed in Chapter 4 were found to be largest at small densities and temperatures, but in this regime the energy transfers and opacities are dominated by free nucleons anyway. Therefore, we do not expect effects of the same order as in Chapter 4 when generalizing our scattering calculations to mixtures of protons and neutrons. This has been checked in a crude approximation using the τ_A calculated in mixtures (combining Eqs. (4.5) and (4.50)) in the neutron-only finite-$\boldsymbol{q}$ structure factor of Eq. (6.15).

7 Charged-Current Interaction Rates

In this section, we focus on charged-current reactions involving multiple nucleons, namely $N+n \longleftrightarrow N+p+e^-+\overline{\nu}_e$ and $N+p \longleftrightarrow N+n+e^+ + \nu_e$. We build on earlier work by Friman and Maxwell [50] who considered this process in the context of neutron star cooling for degenerate conditions.

7.1 Structure Factor and Kinematics

The axial structure factor in terms of the spin-summed squared matrix elements is given by [50, 51]

$$S_A = \frac{(2\pi)^3}{12n}\frac{1}{s}\int \prod_{i=1}^{4} \frac{\mathrm{d}^3 p_i}{(2\pi)^3}\,\delta^+_\epsilon \delta_{\boldsymbol{p}}\, n_1 n_2 (1-n_3)(1-n_4)\,\frac{\sum |M^2|}{G_\mathrm{F}^2 \omega_1 \omega_2}\ . \tag{7.1}$$

This agrees with expressions in Refs. [47, 57]. Here, again, n is the number density of nucleons, $\delta^+_\epsilon \equiv \delta(\omega+\epsilon_1+\epsilon_2-\epsilon_3-\epsilon_4)$ and $\delta_{\boldsymbol{p}} \equiv \delta^{(3)}(\boldsymbol{p}_1+\boldsymbol{p}_2-\boldsymbol{p}_3-\boldsymbol{p}_4)$ are the energy and momentum conserving delta functions, and s is a symmetry factor compensating initial-/final-state double counting, with $s=2$ for the processes discussed in this chapter.

The kinematics are more complicated in the charged-current case compared to neutral-current reactions as we have to take into account that particle species change in the process. The electron gas is highly degenerate, hence the electron Pauli blocking factor cannot be ignored and neutrino capture on neutrons is suppressed for neutrino energies comparable or smaller than the electron Fermi energy. On the other hand, antineutrino capture on protons is hindered by the proton-neutron energy difference.

The energy of a nucleon of species i in an interacting system is given by [48]

$$E_i(p) = m_i + \frac{p^2}{2m_i} + \Sigma_i(p) \equiv m_i + \epsilon_i(p)\ , \tag{7.2}$$

with momentum p, mass m, and self-energy Σ. The single-particle energy ϵ is typically approximated in terms of an effective mass m^* and an energy shift U:

$$\epsilon_i(p) \simeq \frac{p^2}{2m_i^*} + U_i\ . \tag{7.3}$$

The parameters U and m^* can be fit to Eq. (7.2) with the self-energy calculated from nuclear matrix elements, e. g., at the first-order (Hartree-Fock) level:

$$\begin{aligned}\Sigma_i(p) =& \frac{1}{2\pi}\int \mathrm{d}p' p'^{\,2} \int \mathrm{d}\cos\theta\, n^i_{p'} \sum_{lSJ} (2J+1)\,\langle k|V_{llSJ}|k\rangle\,\left(1-(-1)^{l+S+1}\right)\\ &+\frac{1}{4\pi}\int \mathrm{d}p' p'^{\,2} \int \mathrm{d}\cos\theta\, n^j_{p'} \sum_{lSJ} (2J+1)\,\langle k|V_{llSJ}|k\rangle\,\left(1-(-1)^{l+S+1}\right)\\ &+\frac{1}{4\pi}\int \mathrm{d}p' p'^{\,2} \int \mathrm{d}\cos\theta\, n^j_{p'} \sum_{lSJ} (2J+1)\,\langle k|V_{llSJ}|k\rangle\,\left(1-(-1)^{l+S}\right)\ .\end{aligned} \tag{7.4}$$

Here, $k=|\boldsymbol{p}-\boldsymbol{p}'|/2$ and $j \neq i$. Contributions from interactions with the same species are given in the first line, while the other two describe interactions with the other species in the $T=1$ and $T=0$ channel, respectively. For pure neutron matter, this formula reproduces the equation given in Ref. [140].

These energy shifts enter all single-particle energies in Eq. (7.1), namely in the energy-conserving delta function, the distribution functions, and the nucleon propagator in the matrix element (cf. the $\frac{1}{\omega}$ terms in Section 7.2). In neutral-current interactions, the energy shifts in the initial and final state are identical and thus cancel.

The energy shift and the structure factor (as well as the equation of state) should be calculated consistently. At the Born level, the same matrix elements are used for both calculations. At the phase-shift level (corresponding to our T-matrix formalism for collisions), a pseudo-potential given by

$$\left\langle k \middle| V^{\text{pseudo}}_{llSJ} \middle| k \right\rangle = -\frac{\delta_{lSJ}(k)}{km} \tag{7.5}$$

is used for the self-energies. The bound-state contribution of the deuteron has to be treated explicitly. Possible ansatzes include modifying the $^3\text{S}_1$ phase shift by hand [30] or matching to the virial expansion [171].

At the conditions relevant in supernovae, both proton and neutron energies are shifted downwards ($U_i < 0$). Because of the neutron-rich conditions, the shift is considerably larger for protons, hence $\Delta U = U_n - U_p > 0$.

Kinematics are discussed in detail for the single-nucleon charged-current reactions in Ref. [30]. For conditions relevant in supernovae, and using the pseudo-potential above, the $\overline{\nu}_e + p \to e^+ + n$ rate was found to be strongly suppressed and comparable to neutral-current reactions like pair absorption.

A careful derivation of expressions for astrophysical quantities like opacities as well as their evaluation is left to future projects. In this thesis, we focus on the nuclear physics of the collision rate based on modern nuclear forces and compare the rates to the OPE approximation.

7.2 Calculation of Matrix Elements

The charged-current Lagrangian is very similar to the neutral-current Lagrangian discussed in Section 2.2.1. It is non-relativistically given by (see, e. g., Ref. [48])

$$\mathcal{L}^{\text{non-rel}}_{cc} = \sqrt{2} G_\text{F} C \overline{\psi}_e \gamma_\mu (1-\gamma_5) \psi_\nu \phi^\dagger_p (C_V \delta_{\mu 0} - C_A \delta_{\mu i} \sigma^i) \phi_n \,. \tag{7.6}$$

Here, $C = \cos\theta_c \approx 1$ is the Cabibbo factor.

We start with the process $n+n \to n+p+e^- + \overline{\nu}_e$, following Ref. [50], and use $C^n_A = -g_A/2$ and $C = 1$. The diagrams are shown in Fig. 7.1 and the corresponding matrix elements are given by

$$M^{(A)}_{nn\to np} = \frac{G_\text{F}}{\sqrt{2}} \left(\delta_{\mu 0} - g_A \delta_{\mu i} \sigma^i_2\right) l_\mu \frac{1}{\omega} \left\langle 1_n 2_n \middle| \mathcal{T} \middle| 3_n 4_n \right\rangle , \tag{7.7}$$

$$M^{(B)}_{nn\to np} = -\frac{G_\text{F}}{\sqrt{2}} \frac{1}{\omega} \left\langle 1_n 2_p \middle| \mathcal{T} \middle| 3_n 4_p \right\rangle \left(\delta_{\mu 0} - g_A \delta_{\mu i} \sigma^i_2\right) l_\mu \,, \text{ and} \tag{7.8}$$

$$M^{(C)}_{nn\to np} = -\frac{G_\text{F}}{\sqrt{2}} \frac{1}{\omega} \left\langle 1_p 2_n \middle| \mathcal{T} \middle| 3_n 4_p \right\rangle \left(\delta_{\mu 0} - g_A \delta_{\mu i} \sigma^i_1\right) l_\mu \,, \tag{7.9}$$

where l_μ is again the leptonic weak current.

While it is straightforward for bremsstrahlung processes (see Section 2.2.1) to combine the individual contributions and show that the vector part cancels, this is not the case here as each diagram involves a different nuclear matrix element. If isospin symmetry holds, we can split the matrix elements into one part independent of isospin and another part proportional to $\tau_1 \cdot \tau_2$:

$$\mathcal{T} = \mathcal{T}_{\mathbb{1}} + \mathcal{T}_\tau \, \tau_1 \cdot \tau_2 \tag{7.10}$$

and hence

$$\langle nn | \mathcal{T} | nn \rangle = \mathcal{T}_{T=1} \qquad\qquad = \mathcal{T}_{\mathbb{1}} + \mathcal{T}_\tau \,, \tag{7.11}$$

$$\langle np | \mathcal{T} | np \rangle = \frac{1}{2} (\mathcal{T}_{T=1} + \mathcal{T}_{T=0}) = \mathcal{T}_{\mathbb{1}} - \mathcal{T}_\tau \,, \text{ and} \tag{7.12}$$

$$\langle pn | \mathcal{T} | np \rangle = \frac{1}{2} (\mathcal{T}_{T=1} - \mathcal{T}_{T=0}) = 2\mathcal{T}_\tau \,. \tag{7.13}$$

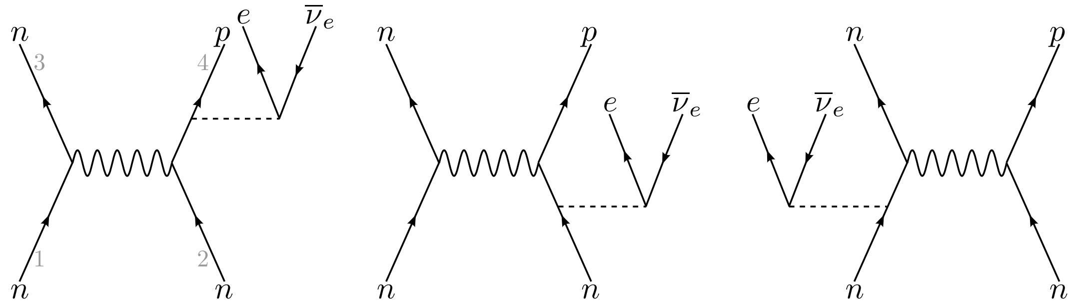

(A) (B) (C)

Figure 7.1: Diagrams for the nn Urca process, following Ref. [50].

Inserting this into Eqs. (7.7) through (7.9), the total $M_{nn\to np}$ can be written as

$$M_{nn\to np} = \frac{G_\mathrm{F}}{\sqrt{2}} g_A \frac{1}{\omega} l_i \left(\left[\mathcal{T}_{\mathbb{1}}, \sigma_2^i\right] - \left\{\mathcal{T}_\tau, \sigma_2^i\right\} + 2\mathcal{T}_\tau \sigma_1^i\right) \tag{7.14}$$

$$= \frac{G_\mathrm{F}}{\sqrt{2}} g_A \frac{1}{\omega} l_i \left[(\mathcal{T}_{\mathbb{1}} - \mathcal{T}_\tau)\sigma_2^i - \sigma_2^i(\mathcal{T}_{\mathbb{1}} + \mathcal{T}_\tau) + 2\mathcal{T}_\tau \sigma_1^i\right] . \tag{7.15}$$

Using the lepton trace in Eq. (2.38) and following the same steps as in Section 2.2.1, we perform the spin sum over the squared matrix element to obtain

$$\sum_{\text{spins}} |M_{nn\to np}|^2 = \mathrm{Tr}_{\sigma_1\sigma_2} |M_{nn\to np}|^2 \tag{7.16}$$

$$= 8\frac{G_\mathrm{F}^2}{2} g_A^2 \frac{\omega_1\omega_2}{\omega^2} \sum_{m_{s_1} m_{s_2}} \left\langle m_{s_1} m_{s_2}\right| \left[\sigma_2^i(\mathcal{T}_{\mathbb{1}}^\dagger - \mathcal{T}_\tau^\dagger) - (\mathcal{T}_{\mathbb{1}}^\dagger + \mathcal{T}_\tau^\dagger)\sigma_2^i + 2\sigma_1^i \mathcal{T}_\tau^\dagger\right] \left(\sum_{m_{s_3} m_{s_4}} \left|m_{s_3} m_{s_4}\right\rangle \left\langle m_{s_3} m_{s_4}\right|\right)$$
$$\times \left[(\mathcal{T}_{\mathbb{1}} - \mathcal{T}_\tau)\sigma_2^i - \sigma_2^i(\mathcal{T}_{\mathbb{1}} + \mathcal{T}_\tau) + 2\mathcal{T}_\tau \sigma_1^i\right] \left|m_{s_1} m_{s_2}\right\rangle \tag{7.17}$$

$$= 8\frac{G_\mathrm{F}^2}{2} g_A^2 \frac{\omega_1\omega_2}{\omega^2}\, 3 \sum_{\{m_{s_i}\}} \left[\mathcal{T}_{\mathbb{1}}^\dagger(2m_{s_2} - 2m_{s_4}) + \mathcal{T}_\tau^\dagger(4m_{s_1} - 2m_{s_2} - 2m_{s_4})\right]$$
$$\times \left[\mathcal{T}_{\mathbb{1}}(2m_{s_2} - 2m_{s_4}) + \mathcal{T}_\tau(4m_{s_1} - 2m_{s_2} - 2m_{s_4})\right] \tag{7.18}$$

$$= 8\cdot 12\frac{G_\mathrm{F}^2}{2} g_A^2 \frac{\omega_1\omega_2}{\omega^2} \sum_{\{m_{s_i}\}} \Big[(m_{s_2} - m_{s_4})^2\, \mathcal{T}_{\mathbb{1}}^\dagger \mathcal{T}_{\mathbb{1}}$$
$$+ (m_{s_2} - m_{s_4})(2m_{s_1} - m_{s_2} - m_{s_4})\,(\mathcal{T}_{\mathbb{1}}^\dagger \mathcal{T}_\tau + \mathcal{T}_\tau^\dagger \mathcal{T}_{\mathbb{1}}) + (2m_{s_1} - m_{s_2} - m_{s_4})^2\, \mathcal{T}_\tau^\dagger \mathcal{T}_\tau\Big] . \tag{7.19}$$

To expand this expression into partial waves, we first couple the spins, leading to

$$\sum_{\text{spins}} |M_{nn\to np}|^2 = 8\cdot 12\frac{G_\mathrm{F}^2}{2} g_A^2 \frac{\omega_1\omega_2}{\omega^2} \sum_{\substack{SS'\tilde{S}\tilde{S}' \\ M_S M_S' \tilde{M}_S \tilde{M}_S'}} \sum_{\{m_{s_i}\}} C^{SM_S}_{s_1 m_{s_1} s_2 m_{s_2}} C^{S'M_S'}_{s_3 m_{s_3} s_4 m_{s_4}} C^{\tilde{S}\tilde{M}_S}_{s_1 m_{s_1} s_2 m_{s_2}} C^{\tilde{S}\tilde{M}_S'}_{s_3 m_{s_3} s_4 m_{s_4}} \Big[(m_{s_2} - m_{s_4})^2\, \mathcal{T}_{\mathbb{1}}^\dagger \mathcal{T}_{\mathbb{1}}$$
$$+ (m_{s_2} - m_{s_4})(2m_{s_1} - m_{s_2} - m_{s_4})\,(\mathcal{T}_{\mathbb{1}}^\dagger \mathcal{T}_\tau + \mathcal{T}_\tau^\dagger \mathcal{T}_{\mathbb{1}}) + (2m_{s_1} - m_{s_2} - m_{s_4})^2\, \mathcal{T}_\tau^\dagger \mathcal{T}_\tau\Big] \tag{7.20}$$

$$= 8\cdot 12\frac{G_\mathrm{F}^2}{2} g_A^2 \frac{\omega_1\omega_2}{\omega^2} \sum_{S\tilde{S}M_S M_S'} \sum_{\{m_{s_i}\}} C^{SM_S}_{s_1 m_{s_1} s_2 m_{s_2}} C^{SM_S'}_{s_3 m_{s_3} s_4 m_{s_4}} C^{\tilde{S}M_S}_{s_1 m_{s_1} s_2 m_{s_2}} C^{\tilde{S}M_S'}_{s_3 m_{s_3} s_4 m_{s_4}} \Big[(m_{s_2} - m_{s_4})^2\, \mathcal{T}_{\mathbb{1}}^\dagger \mathcal{T}_{\mathbb{1}}$$
$$+ (m_{s_2} - m_{s_4})(2m_{s_1} - m_{s_2} - m_{s_4})\,(\mathcal{T}_{\mathbb{1}}^\dagger \mathcal{T}_\tau + \mathcal{T}_\tau^\dagger \mathcal{T}_{\mathbb{1}}) + (2m_{s_1} - m_{s_2} - m_{s_4})^2\, \mathcal{T}_\tau^\dagger \mathcal{T}_\tau\Big] \tag{7.21}$$

$$\begin{aligned}
&= 8\cdot 12\frac{G_{\mathrm{F}}^2}{2}g_A^2\frac{\omega_1\omega_2}{\omega^2}\sum_{S\tilde{S}M_SM_S'}\Bigg[(-1)^{S+\tilde{S}}\frac{1}{2}(1-M_SM_S')\big\langle(34)SM_S'\big|\mathcal{T}_{\mathbb{1}}\big|(12)SM_S\big\rangle\big\langle(12)\tilde{S}M_S\big|\mathcal{T}_{\mathbb{1}}\big|(34)\tilde{S}M_S'\big\rangle \\
&\quad+(-1)^{S+\tilde{S}}\frac{1}{2}(2M_S^2-1)(1-M_SM_S')\Bigg(\big\langle(34)SM_S'\big|\mathcal{T}_{\mathbb{1}}\big|(12)SM_S\big\rangle\big\langle(12)\tilde{S}M_S\big|\mathcal{T}_{\tau}\big|(34)\tilde{S}M_S'\big\rangle \\
&\qquad+\big\langle(34)SM_S'\big|\mathcal{T}_{\tau}\big|(12)SM_S\big\rangle\big\langle(12)\tilde{S}M_S\big|\mathcal{T}_{\mathbb{1}}\big|(34)\tilde{S}M_S'\big\rangle\Bigg) \\
&\quad+\frac{1}{2}\big(5-M_S(4M_S+M_S')+2(\delta_{S\tilde{S}}-1)\big)\big\langle(34)SM_S'\big|\mathcal{T}_{\tau}\big|(12)SM_S\big\rangle\big\langle(12)\tilde{S}M_S\big|\mathcal{T}_{\tau}\big|(34)\tilde{S}M_S'\big\rangle\Bigg], \qquad (7.22)
\end{aligned}$$

where we used $S' = S$ and $\tilde{S}' = \tilde{S}$ (because the potential conserves spin) as well as $\tilde{M}_S = M_S$ and $\tilde{M}_S' = M_S'$ from the Clebsch-Gordan coefficients.

We then follow the derivation in Section 4.1.1 to obtain

$$\begin{aligned}
\sum_{\text{spins}}|M_{nn\to np}|^2 =& 24\,G_{\mathrm{F}}^2g_A^2\frac{\omega_1\omega_2}{\omega^2}\sum_{\substack{LJS\tilde{S}\\M_SM_S'}}\sum_{\substack{ll'mm'\\\tilde{l}\tilde{l}'\tilde{m}\tilde{m}'\\Jm_J\tilde{J}\tilde{m}_J}}(4\pi)^4 i^{l'-l+\tilde{l}-\tilde{l}'}C^{Jm_J}_{l'm'SM_S'}C^{Jm_J}_{lmSM_S}C^{\tilde{J}\tilde{m}_J}_{\tilde{l}'\tilde{m}'\tilde{S}M_S'}C^{\tilde{J}\tilde{m}_J}_{\tilde{l}\tilde{m}\tilde{S}M_S}Y^*_{l'm'}(\hat{p}')Y_{lm}(\hat{p})Y_{\tilde{l}'\tilde{m}'}(\hat{p}')Y^*_{\tilde{l}\tilde{m}}(\hat{p}) \\
&\times\Bigg[(-1)^{S+\tilde{S}}\frac{1}{2}(1-M_SM_S')\big\langle p'\big|(\mathcal{T}^{\mathrm{as}}_{\mathbb{1}})_{ll'JS}\big|p\big\rangle\big\langle p\big|(\mathcal{T}^{\mathrm{as}}_{\mathbb{1}})_{\tilde{l}\tilde{l}'\tilde{J}\tilde{S}}\big|p'\big\rangle \\
&\quad+(-1)^{S+\tilde{S}}\frac{1}{2}(2M_S^2-1)(1-M_SM_S')\Bigg(\big\langle p'\big|(\mathcal{T}^{\mathrm{as}}_{\mathbb{1}})_{ll'JS}\big|p\big\rangle\big\langle p\big|(\mathcal{T}^{\mathrm{as}}_{\tau})_{\tilde{l}\tilde{l}'\tilde{J}\tilde{S}}\big|p'\big\rangle \\
&\qquad+\big\langle p'\big|(\mathcal{T}^{\mathrm{as}}_{\tau})_{ll'JS}\big|p\big\rangle\big\langle p\big|(\mathcal{T}^{\mathrm{as}}_{\mathbb{1}})_{\tilde{l}\tilde{l}'\tilde{J}\tilde{S}}\big|p'\big\rangle\Bigg) \\
&\quad+\frac{1}{2}\big(5-M_S(4M_S+M_S')+2(\delta_{S\tilde{S}}-1)\big)\big\langle p'\big|(\mathcal{T}^{\mathrm{as}}_{\tau})_{ll'JS}\big|p\big\rangle\big\langle p\big|(\mathcal{T}^{\mathrm{as}}_{\tau})_{\tilde{l}\tilde{l}'\tilde{J}\tilde{S}}\big|p'\big\rangle\Bigg] \qquad (7.23) \\
=& 24\,G_{\mathrm{F}}^2g_A^2\frac{\omega_1\omega_2}{\omega^2}\sum_{LJS\tilde{S}M_SM_S'}\sum_{ll'J}\sum_{\tilde{l}\tilde{l}'\tilde{J}}(4\pi)^2 i^{l'-l+\tilde{l}-\tilde{l}'}(-1)^{L+J+\tilde{J}+l+\tilde{l}}(\hat{J}\hat{L}\hat{J}\hat{\tilde{J}})^2\frac{\hat{l}\hat{l}'\hat{\tilde{l}}\hat{\tilde{l}}'}{\hat{S}\hat{\tilde{S}}}C^{SM_S}_{L(M_S-M_S')SM_S'}C^{\tilde{S}M_S}_{L(M_S-M_S')\tilde{S}M_S'} \\
&\times\begin{Bmatrix} l' & l & L \\ \tilde{l} & \tilde{l}' & J \end{Bmatrix}\begin{Bmatrix} l' & l & L \\ S & S & J \end{Bmatrix}\begin{Bmatrix} \tilde{l} & \tilde{l}' & L \\ \tilde{S} & \tilde{S} & \tilde{J} \end{Bmatrix}\begin{pmatrix} l' & \tilde{l}' & J \\ 0 & 0 & 0 \end{pmatrix}\begin{pmatrix} l & \tilde{l} & J \\ 0 & 0 & 0 \end{pmatrix}P_J(\cos\theta) \\
&\times\Bigg[(1-M_SM_S')\big\langle p'\big|(\mathcal{T}^{\mathrm{as}}_{\mathbb{1}})_{ll'JS}\big|p\big\rangle\big\langle p\big|(\mathcal{T}^{\mathrm{as}}_{\mathbb{1}})_{\tilde{l}\tilde{l}'\tilde{J}\tilde{S}}\big|p'\big\rangle \\
&\quad+(2M_S^2-1)(1-M_SM_S')\Bigg(\big\langle p'\big|(\mathcal{T}^{\mathrm{as}}_{\mathbb{1}})_{ll'JS}\big|p\big\rangle\big\langle p\big|(\mathcal{T}^{\mathrm{as}}_{\tau})_{\tilde{l}\tilde{l}'\tilde{J}\tilde{S}}\big|p'\big\rangle \\
&\qquad+\big\langle p'\big|(\mathcal{T}^{\mathrm{as}}_{\tau})_{ll'JS}\big|p\big\rangle\big\langle p\big|(\mathcal{T}^{\mathrm{as}}_{\mathbb{1}})_{\tilde{l}\tilde{l}'\tilde{J}\tilde{S}}\big|p'\big\rangle\Bigg) \\
&\quad+(-1)^{S+\tilde{S}}\big(5-M_S(4M_S+M_S')+2(\delta_{S\tilde{S}}-1)\big)\big\langle p'\big|(\mathcal{T}^{\mathrm{as}}_{\tau})_{ll'JS}\big|p\big\rangle\big\langle p\big|(\mathcal{T}^{\mathrm{as}}_{\tau})_{\tilde{l}\tilde{l}'\tilde{J}\tilde{S}}\big|p'\big\rangle\Bigg]. \qquad (7.24)
\end{aligned}$$

Here,

$$\begin{aligned}
\big\langle p'\big|(\mathcal{T}^{\mathrm{as}}_{\mathbb{1}})_{ll'JS}\big|p\big\rangle &= \frac{1}{4}\Big(\big(1-(-1)^{l+S+0}\big)\big\langle p'\big|\mathcal{T}^{T=0}_{ll'JS}\big|p\big\rangle+3\big(1-(-1)^{l+S+1}\big)\big\langle p'\big|\mathcal{T}^{T=1}_{ll'JS}\big|p\big\rangle\Big) \text{ and} \qquad (7.25) \\
\big\langle p'\big|(\mathcal{T}^{\mathrm{as}}_{\tau})_{ll'JS}\big|p\big\rangle &= \frac{1}{4}\Big(\big(1-(-1)^{l+S+1}\big)\big\langle p'\big|\mathcal{T}^{T=1}_{ll'JS}\big|p\big\rangle-\big(1-(-1)^{l+S+0}\big)\big\langle p'\big|\mathcal{T}^{T=0}_{ll'JS}\big|p\big\rangle\Big)\,. \qquad (7.26)
\end{aligned}$$

For one-pion exchange, Eq. (7.24) has been numerically checked against Eq. (71) of Friman and Maxwell [50] using the partial-wave-expanded matrix elements from Nogga *et al.* [172] (cf. Appendix B).

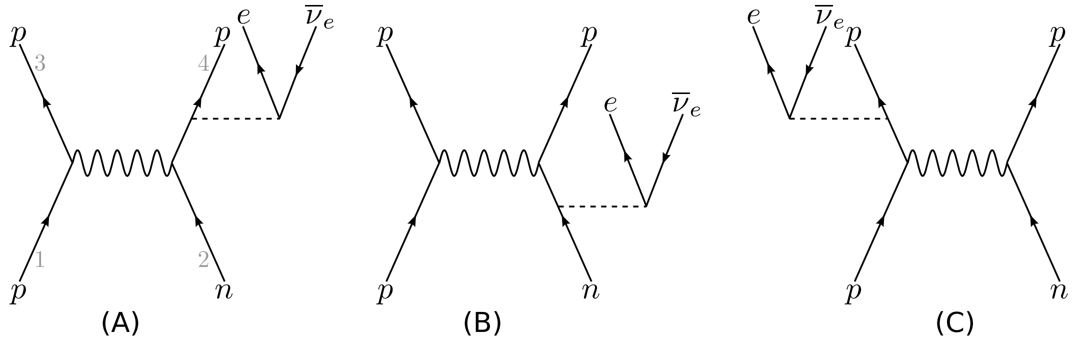

Figure 7.2: Diagrams for the *np* Urca process.

We next look at the *np* Urca process, $p + n \to p + p + e^- + \overline{\nu}_e$. This process is closely related to the one discussed so far. However, the diagrams (Fig. 7.2) are different as the weak current cannot interact with incoming particle 1.

The matrix elements are given by

$$M^{(A)}_{pn\to pp} = \frac{G_\mathrm{F}}{\sqrt{2}} \left(\delta_{\mu 0} - g_A \delta_{\mu i} \sigma_2^i\right) l_\mu \frac{1}{\omega} \left\langle 1_n 2_n \middle| \mathcal{T} \middle| 3_n 4_n \right\rangle \,, \tag{7.27}$$

$$M^{(B)}_{pn\to pp} = -\frac{G_\mathrm{F}}{\sqrt{2}} \frac{1}{\omega} \left\langle 1_n 2_p \middle| \mathcal{T} \middle| 3_n 4_p \right\rangle \left(\delta_{\mu 0} - g_A \delta_{\mu i} \sigma_2^i\right) l_\mu \text{ , and} \tag{7.28}$$

$$M^{(C)}_{pn\to pp} = -\frac{G_\mathrm{F}}{\sqrt{2}} \frac{1}{\omega} \left\langle 1_p 2_n \middle| \mathcal{T} \middle| 3_n 4_p \right\rangle \left(\delta_{\mu 0} - g_A \delta_{\mu i} \sigma_1^i\right) l_\mu \,. \tag{7.29}$$

Assuming isospin symmetry again, these can be combined to

$$M_{pn\to pp} = \frac{G_\mathrm{F}}{\sqrt{2}} g_A \frac{1}{\omega} l_i \left[(\mathcal{T}_{\mathbb{1}} + \mathcal{T}_\tau)\, \sigma_2^i - \sigma_2^i (\mathcal{T}_{\mathbb{1}} - \mathcal{T}_\tau) - 2\sigma_1^i \mathcal{T}_\tau \right] . \tag{7.30}$$

Following the same steps as in the previous section, we obain

$$\begin{aligned} \sum_{\text{spins}} |M_{pn\to pp}|^2 = 8 \cdot 12 \frac{G_\mathrm{F}^2}{2} g_A^2 \frac{\omega_1 \omega_2}{\omega^2} \sum_{\{m_{s_i}\}} \Big[& (m_{s_2} - m_{s_4})^2\, \mathcal{T}_{\mathbb{1}}^\dagger \mathcal{T}_{\mathbb{1}} \\ & + (m_{s_2} - m_{s_4})(m_{s_2} + m_{s_4} - 2m_{s_3}) (\mathcal{T}_{\mathbb{1}}^\dagger \mathcal{T}_\tau + \mathcal{T}_\tau^\dagger \mathcal{T}_{\mathbb{1}}) + (m_{s_2} + m_{s_4} - 2m_{s_3})^2\, \mathcal{T}_\tau^\dagger \mathcal{T}_\tau \Big] . \end{aligned} \tag{7.31}$$

Coupling the spins leads to the same expression as in the previous section except M_S and M_S' are interchanged in the prefactors, hence

$$\begin{aligned} \sum_{\text{spins}} |M_{pn\to pp}|^2 = 8 \cdot 12 \frac{G_\mathrm{F}^2}{2} g_A^2 \frac{\omega_1 \omega_2}{\omega^2} \sum_{S\tilde{S}M_S M_S'} \Bigg[& (-1)^{S+\tilde{S}} \frac{1}{2} (1 - M_S M_S') \left\langle (34) S M_S' \middle| \mathcal{T}_{\mathbb{1}} \middle| (12) S M_S \right\rangle \left\langle (12) \tilde{S} M_S \middle| \mathcal{T}_{\mathbb{1}} \middle| (34) \tilde{S} M_S' \right\rangle \\ & + (-1)^{S+\tilde{S}} \frac{1}{2} (2M_S'^2 - 1)(1 - M_S M_S') \Big(\left\langle (34) S M_S' \middle| \mathcal{T}_{\mathbb{1}} \middle| (12) S M_S \right\rangle \left\langle (12) \tilde{S} M_S \middle| \mathcal{T}_\tau \middle| (34) \tilde{S} M_S' \right\rangle \\ & \qquad + \left\langle (34) S M_S' \middle| \mathcal{T}_\tau \middle| (12) S M_S \right\rangle \left\langle (12) \tilde{S} M_S \middle| \mathcal{T}_{\mathbb{1}} \middle| (34) \tilde{S} M_S' \right\rangle \Big) \\ & + \frac{1}{2} \big(5 - M_S'(M_S + 4M_S') + 2(\delta_{S\tilde{S}} - 1)\big) \left\langle (34) S M_S' \middle| \mathcal{T}_\tau \middle| (12) S M_S \right\rangle \left\langle (12) \tilde{S} M_S \middle| \mathcal{T}_\tau \middle| (34) \tilde{S} M_S' \right\rangle \Bigg] \end{aligned} \tag{7.32}$$

$$\begin{aligned} &= 24\, G_{\mathrm{F}}^2 g_A^2 \frac{\omega_1\omega_2}{\omega^2} \sum_{LJS\tilde{S}M_SM_S'} \sum_{ll'J} \sum_{\tilde{l}\tilde{l}'\tilde{J}} (4\pi)^2 i^{l'-l+\tilde{l}-\tilde{l}'} (-1)^{L+J+\tilde{J}+l+\tilde{l}} (\hat{J}\hat{L}\hat{J}\hat{\tilde{J}})^2 \frac{\hat{l}\hat{l}'\hat{\tilde{l}}\hat{\tilde{l}}'}{\hat{S}\hat{\tilde{S}}} C^{SM_S}_{L(M_S-M_S')SM_S'} C^{\tilde{S}M_S}_{L(M_S-M_S')\tilde{S}M_S'} \\ &\times \begin{Bmatrix} l' & l & L \\ \tilde{l} & \tilde{l}' & J \end{Bmatrix} \begin{Bmatrix} l' & l & L \\ S & S & J \end{Bmatrix} \begin{Bmatrix} \tilde{l} & \tilde{l}' & L \\ \tilde{S} & \tilde{S} & \tilde{J} \end{Bmatrix} \begin{pmatrix} l' & \tilde{l}' & J \\ 0 & 0 & 0 \end{pmatrix} \begin{pmatrix} l & \tilde{l} & J \\ 0 & 0 & 0 \end{pmatrix} P_J(\cos\theta) \\ &\times \Big[(1-M_SM_S') \left\langle p' \left| (\mathcal{T}^{\mathrm{as}}_{\mathbb{1}})_{ll'JS} \right| p \right\rangle \left\langle p \left| (\mathcal{T}^{\mathrm{as}}_{\mathbb{1}})_{\tilde{l}\tilde{l}'\tilde{J}\tilde{S}} \right| p' \right\rangle \\ &\quad + (2M_S'^2-1)(1-M_SM_S') \Big(\left\langle p' \left| (\mathcal{T}^{\mathrm{as}}_{\mathbb{1}})_{ll'JS} \right| p \right\rangle \left\langle p \left| (\mathcal{T}^{\mathrm{as}}_{\tau})_{\tilde{l}\tilde{l}'\tilde{J}\tilde{S}} \right| p' \right\rangle \\ &\qquad + \left\langle p' \left| (\mathcal{T}^{\mathrm{as}}_{\tau})_{ll'JS} \right| p \right\rangle \left\langle p \left| (\mathcal{T}^{\mathrm{as}}_{\mathbb{1}})_{\tilde{l}\tilde{l}'\tilde{J}\tilde{S}} \right| p' \right\rangle \Big) \\ &\quad + (-1)^{S+\tilde{S}} \left(5 - M_S'(M_S+4M_S') + 2(\delta_{S\tilde{S}}-1)\right) \left\langle p' \left| (\mathcal{T}^{\mathrm{as}}_{\tau})_{ll'JS} \right| p \right\rangle \left\langle p \left| (\mathcal{T}^{\mathrm{as}}_{\tau})_{\tilde{l}\tilde{l}'\tilde{J}\tilde{S}} \right| p' \right\rangle \Big] . \end{aligned} \tag{7.33}$$

Using the symmetries of the two Clebsch-Gordan coefficients, we can rewrite them as [156]

$$C^{SM_S}_{L(M_S-M_S')SM_S'} C^{\tilde{S}M_S}_{L(M_S-M_S')\tilde{S}M_S'} = (-1)^{L-(M_S-M_S')} \sqrt{\frac{2S+1}{2S+1}} C^{SM_S'}_{SM_S L(M_S'-M_S)} (-1)^{L-(M_S-M_S')} \sqrt{\frac{2\tilde{S}+1}{2\tilde{S}+1}} C^{\tilde{S}M_S'}_{\tilde{S}M_S L(M_S'-M_S)} \tag{7.34}$$

$$= (-1)^{2L-2(M_S-M_S')} (-1)^{S+L-S} C^{SM_S'}_{L(M_S'-M_S)SM_S} (-1)^{\tilde{S}+L-\tilde{S}} C^{\tilde{S}M_S'}_{L(M_S'-M_S)\tilde{S}M_S} \tag{7.35}$$

$$= C^{SM_S'}_{L(M_S'-M_S)SM_S} C^{\tilde{S}M_S'}_{L(M_S'-M_S)\tilde{S}M_S} . \tag{7.36}$$

Inserting this into Eq. (7.33) and relabelling $M_S \longleftrightarrow M_S'$, this expression becomes identical to the nn result in Eq. (7.24).

Finally, we consider the two processes converting protons to neutrons, $p+p \longrightarrow p+n+e^+ + \nu_e$ and $n+p \longrightarrow n+n+e^+ + \nu_e$. The corresponding diagrams are the same as in Figures 7.1 and 7.2 with the substitutions $n \longleftrightarrow p$, $e \longrightarrow e^+$ and $\overline{\nu}_e \longrightarrow \nu_e$. The only change is then a sign going from $C_A^n = -g_A/2$ to $C_A^p = g_A/2$ in the charge-current Lagrangian, which does not matter when calculating the squared matrix element. Hence these two processes are described by the spin-summed matrix element in Eq. (7.24) as well.

All four processes being described by the same spin-summed matrix element is a consequence of time reversal (e. g., $nn \longrightarrow np$ and $np \longrightarrow nn$) and isospin symmetry (e. g., $nn \longrightarrow np$ and $pp \longrightarrow pn$) – the changes in the leptonic part of the interaction do not impact the matrix elements.

7.3 Spin Relaxation Rate

The spin relaxation rate $1/\tau_\sigma^{cc}$ can be derived in analogy to the steps taken in Section 4.1, but with some additional considerations as one nucleon changes its species between the initial and final state. For the derivation, we will consider the process $N+n \longrightarrow N+p+e^- + \overline{\nu}_e$, where N is either a neutron or a proton.

The energy-conserving delta function can be written as

$$\delta_\epsilon^+ = \delta(\epsilon_1+\epsilon_2-\epsilon_3-\epsilon_4+\omega) = \delta\left(\frac{p_1^2}{2m_N^*} + U_N + \frac{p_2^2}{2m_n^*} + U_n - \frac{p_3^2}{2m_N^*} - U_N - \frac{p_4^2}{2m_p^*} - U_p + \omega\right) \tag{7.37}$$

$$= \delta\left(\frac{p^2}{2m_{Nn}^*} - \frac{p'^2}{2m_{Np}^*} + \Delta U + \omega\right) . \tag{7.38}$$

From there, we can identify

$$p' = \sqrt{p^2 \frac{m_{Np}^*}{m_{Nn}^*} + 2m_{Np}^*(\omega + \Delta U)} . \tag{7.39}$$

The equivalent of Eq. (4.10) is

$$\frac{n_3 n_4 (1-n_1)(1-n_2)}{n_1 n_2 (1-n_3)(1-n_4)} \overset{\delta_\epsilon^+}{=} e^{-\omega/T} e^{(\mu_p-\mu_n)/T} \,. \tag{7.40}$$

Similarly,

$$n_1 n_2 (1-n_3)(1-n_4) = e^{\omega/(2T)}\, e^{(\mu_n-\mu_p)/(2T)} \prod_{\lambda=1}^{4} \frac{1}{2\cosh(x_\lambda/2)} \,, \tag{7.41}$$

and the hyperbolic cosines in the non-degenerate limit (cf. Eq. (4.26)) are given by

$$\begin{aligned}
&\prod_{i=1}^{4} \frac{1}{2\cosh[(\epsilon_i-\mu_i)/(2T)]} \\
&\quad = e^{-[P^2/(2(m_N^*+m_n^*))+P^2/(2(m_N^*+m_p^*))+p^2/(2m_{Nn}^*)+\overbrace{p'^2/(2m_{Np}^*)}^{p^2/(2m_{Nn}^*)+\omega+\Delta U}]/(2T)}\, e^{-(U_N+U_n+U_N+U_p)/(2T)}\, e^{(\mu_N+\mu_n+\mu_N+\mu_p)/(2T)} && (7.42)\\
&\quad \approx e^{-[P^2/(2(m_N^*+m_n^*))+p^2/(2m_{Nn}^*)]/T}\, e^{-(U_N+U_n+U_N+U_n)/(2T)}\, e^{(\mu_N+\mu_n+\mu_N+\mu_n)/(2T)}\, e^{-\omega/(2T)}\, e^{(\mu_p-\mu_n)/(2T)} \,. && (7.43)
\end{aligned}$$

After performing the integrals over P and p, this is proportional to $n_N n_n e^{-(\omega+\mu_n-\mu_p)/(2T)}$. Here, we assume $m_n^* \approx m_p^*$ to allow for the combination of the total momenta and the subsequent identification of the densities.

The appropriate m_{ij}^* indices can be identified from the derivation in Section 4.1. The factor $\frac{1}{\omega}$ originates in the matrix elements and picks up an additional ΔU as a neutron is changed into a proton. Furthermore, we need to add a factor of 2 to account for the change in symmetry factors. Putting it all together, we obtain

$$\frac{1}{\tau_\sigma^{cc}} = \frac{2\, n_N n_n\, m_{Np}^* \sinh\big((\omega+\mu_n-\mu_p)/(2T)\big)}{\chi_0^{cc}\, \pi\, (\omega+\Delta U)\, \sqrt{2\pi (m_{Nn}^* T)^3}}\, e^{-(\omega+\mu_n-\mu_p)/(2T)} \int_{p_{\min}}^{\infty} dp\, p^2\, p'\, e^{-p^2/(2m_{Nn}^* T)} \int_{-1}^{1} d\cos\theta\, W^{cc} \,. \tag{7.44}$$

Here, χ_0^{cc} is again the static susceptibility in the absence of interactions.

The expression for the two processes converting protons into neutrons is equivalent, but with the indices n and p interchanged and, consequently, $\Delta U \to -\Delta U$.

We can identify

$$W^{cc} = \frac{1}{48\, G_F^2 g_A^2} \frac{\omega^2}{\omega_1 \omega_2} \sum_{\text{spins}} |M_{nn\to np}|^2 \,, \tag{7.45}$$

where the spin-summed squared matrix elements were calculated in Section 7.2. The $\cos\theta$ integration can again be performed analytically using Eq. (4.48). Hence, the partial-wave-expanded expression of Eq. (7.44) is given by

$$\begin{aligned}
\frac{1}{\tau_\sigma^{cc}} &= 32\sqrt{\pi} n_N n_n \frac{m_{Np}^* \sinh\big((\omega+\mu_n-\mu_p)/(2T)\big)}{\chi_0^{cc}\, (\omega+\Delta U)\, \sqrt{2(m_{Nn}^* T)^3}} \int_{p_{\min}}^{\infty} dp\, p^2\, p'\, e^{-p^2/(2m_{Nn}^* T)-(\omega+\mu_n-\mu_p)/(2T)} \\
&\quad \times \sum_{LS\tilde{S}M_S M_S'} \sum_{ll'J\tilde{J}} (-1)^{L+J+\tilde{J}} (\hat{L}\hat{J}\hat{\tilde{J}})^2 \frac{\hat{l}\hat{l}'}{\hat{S}\hat{\tilde{S}}} \begin{Bmatrix} l' & l & L \\ l & l' & 0 \end{Bmatrix} \begin{Bmatrix} l' & l & L \\ S & S & J \end{Bmatrix} \begin{Bmatrix} l & l' & L \\ \tilde{S} & \tilde{S} & \tilde{J} \end{Bmatrix} C^{SM_S}_{L(M_S-M_S')SM_S'} C^{\tilde{S}M_S}_{L(M_S-M_S')\tilde{S}M_S'} \\
&\quad \times \Big[(1-M_S M_S') \big\langle p' \big| (\mathcal{T}_{\mathbb{1}}^{\text{as}})_{ll'JS} \big| p \big\rangle \big\langle p \big| (\mathcal{T}_{\mathbb{1}}^{\text{as}})_{ll'\tilde{J}\tilde{S}} \big| p' \big\rangle \\
&\qquad + (2M_S^2-1)(1-M_S M_S') \Big(\big\langle p' \big| (\mathcal{T}_{\mathbb{1}}^{\text{as}})_{ll'JS} \big| p \big\rangle \big\langle p \big| (\mathcal{T}_{\tau}^{\text{as}})_{ll'\tilde{J}\tilde{S}} \big| p' \big\rangle + \big\langle p' \big| (\mathcal{T}_{\tau}^{\text{as}})_{ll'JS} \big| p \big\rangle \big\langle p \big| (\mathcal{T}_{\mathbb{1}}^{\text{as}})_{ll'\tilde{J}\tilde{S}} \big| p' \big\rangle \Big) \\
&\qquad + (-1)^{S+\tilde{S}} \big(5 - M_S(4M_S+M_S') + 2(\delta_{S\tilde{S}}-1)\big) \big\langle p' \big| (\mathcal{T}_{\tau}^{\text{as}})_{ll'JS} \big| p \big\rangle \big\langle p \big| (\mathcal{T}_{\tau}^{\text{as}})_{ll'\tilde{J}\tilde{S}} \big| p' \big\rangle \Big] \,.
\end{aligned} \tag{7.46}$$

For a first calculation based on this formalism, we again neglect effective mass effects, set $m_n^* = m_p^* = m_N$, and take $\Delta U = 0$. In symmetric nuclear matter, we can use $\mu_n = \mu_p$ and simplify Eq. (7.46) to read

$$
\begin{aligned}
\frac{1}{\tau_\sigma^{cc}}\bigg|_{\Delta U=0}^{\mathrm{SNM}} &= 8\sqrt{\pi}\, n^2 \frac{\sinh\big(\omega/(2T)\big)}{\chi_0^{cc}\,\omega\,\sqrt{m_N T^3}} \int_{p_{\min}}^{\infty} dp\, p^2\, p'\, e^{-p^2/(m_N T)-\omega/(2T)} \\
&\times \sum_{L S \tilde{S} M_S M_S'} \sum_{l l' J \tilde{J}} (-1)^{L+J+\tilde{J}} (\hat{L}\hat{J}\hat{\tilde{J}})^2 \frac{\hat{l}\hat{l}'}{\hat{S}\hat{\tilde{S}}} \begin{Bmatrix} l' & l & L \\ l & l' & 0 \end{Bmatrix} \begin{Bmatrix} l' & l & L \\ S & S & J \end{Bmatrix} \begin{Bmatrix} l & l' & L \\ \tilde{S} & \tilde{S} & \tilde{J} \end{Bmatrix} C^{S M_S}_{L(M_S-M_S') S M_S'} C^{\tilde{S} M_S}_{L(M_S-M_S') \tilde{S} M_S'} \\
&\times \Big[(1-M_S M_S') \left\langle p' \middle| (\mathcal{T}^{\mathrm{as}}_{\mathbb{1}})_{l l' J S} \middle| p \right\rangle \left\langle p \middle| (\mathcal{T}^{\mathrm{as}}_{\mathbb{1}})_{l l' \tilde{J} \tilde{S}} \middle| p' \right\rangle \\
&\quad + (2M_S^2-1)(1-M_S M_S') \Big(\left\langle p' \middle| (\mathcal{T}^{\mathrm{as}}_{\mathbb{1}})_{l l' J S} \middle| p \right\rangle \left\langle p \middle| (\mathcal{T}^{\mathrm{as}}_{\tau})_{l l' \tilde{J} \tilde{S}} \middle| p' \right\rangle + \left\langle p' \middle| (\mathcal{T}^{\mathrm{as}}_{\tau})_{l l' J S} \middle| p \right\rangle \left\langle p \middle| (\mathcal{T}^{\mathrm{as}}_{\mathbb{1}})_{l l' \tilde{J} \tilde{S}} \middle| p' \right\rangle \Big) \\
&\quad + (-1)^{S+\tilde{S}} \Big(5 - M_S(4M_S + M_S') + 2(\delta_{S\tilde{S}} - 1)\Big) \left\langle p' \middle| (\mathcal{T}^{\mathrm{as}}_{\tau})_{l l' J S} \middle| p \right\rangle \left\langle p \middle| (\mathcal{T}^{\mathrm{as}}_{\tau})_{l l' \tilde{J} \tilde{S}} \middle| p' \right\rangle \Big] . \qquad (7.47)
\end{aligned}
$$

Furthermore, we employ the on-shell approximation for the nuclear matrix elements (see Section 4.1.1).

Figure 7.3 shows $\chi_0^{cc}/\tau_\sigma^{cc}$ under these conditions and assumptions. We show results based on Friman and Maxwell as well as OPE results based on the partial-wave expansion. The two agree extremely well, thus providing a successful check of the expansion. Similar to our neutron-matter results (see Section 4.2), we find a rather good agreement between OPE and N^{3}LO results at lower densities and a reduction by a factor of 2—3 at 10^{14} g cm^{-3} when taking into account the higher-order chiral interactions. The T-matrix result again shows the strong enhancement at low densities indicating the breakdown of the Born approximation.

We abstain from speculating about the astrophysical impact of our findings as astrophysical quantities will again sample the structure factor at different ω, which might lead to sizable changes as seen in Section 4.3 for the neutral-current case. Therefore, expressions for astrophysically relevant quantities like emissivities or mean-free paths should be derived. In addition, including finite ΔU and chemical potential differences might alter our findings significantly.

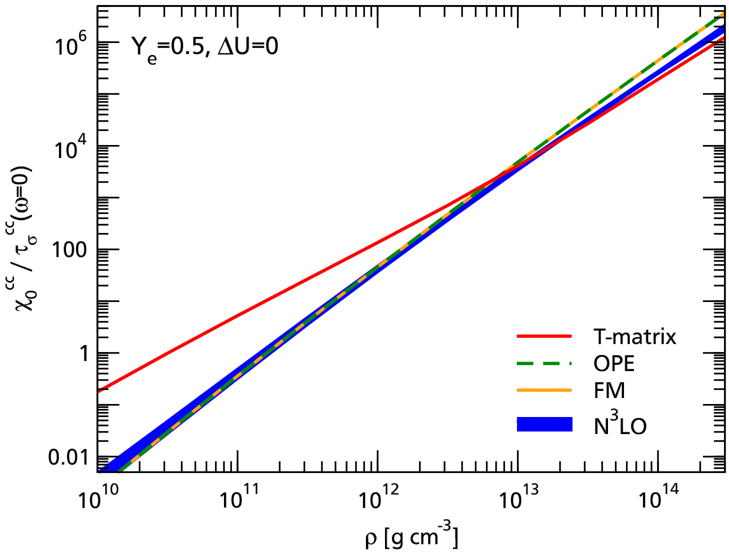

Figure 7.3: Charged-current spin relaxation rate (or rather, $\chi_0^{cc}/\tau_\sigma^{cc}$) at $\omega = 0$ in symmetric nuclear matter as a function of density, setting $\Delta U = 0$. The temperature is again parametrized by Eq. (2.44). The orange solid line shows the results obtained by combining $\sum |M|^2$ from Friman and Maxwell [50] with Eqs. (7.44) and (7.45). The green dashed line corresponds to using the partial-wave-expanded matrix elements in Eq. (7.47), while the red line (blue band) is obtained by using the T-matrix (chiral N^{3}LO) interactions in the same equation.

8 Summary and Outlook

While neutrinos play a key role in the explosion mechanism of core-collapse supernovae, neutrino reaction rates with interacting nucleons included in supernova simulations are based on several simplifications, the one-pion-exchange (OPE) approximation for example. The goal of this thesis was to improve these rates taking into account the effect in mixtures of protons and neutrons and using modern two- and three-nucleon interactions, to include finite momentum transfer, and to apply these rates in supernova simulations.

The neutral-current processes of neutrino pair absorption, bremsstrahlung, and inelastic scattering on nucleons are described by the same structure factor containing the information about the nuclear interactions. Building on former work and working in the limit of non-degenerate conditions relevant for supernova simulations, we derived an expression for the axial structure factor for mixtures of protons and neutrons. We expanded the result into partial waves, allowing us to use any nucleon-nucleon interaction available in partial waves to calculate rates. Furthermore, an analytical expression was derived in the case of one-pion-exchange and leading-order chiral interactions.

From this structure factor, we calculated spin relaxation rates and found only a small dependence of the OPE and higher-density chiral effective field theory (EFT) results on the electron fraction Y_e. In pure neutron matter (PNM), central terms of the interaction do not contribute. This is not the case in mixtures, creating a stronger Y_e dependence of the chiral potentials at lower densities. Going beyond the Born approximation by using a T-matrix based on phase shifts, we found a strong enhancement of the relaxation rate at low densities that we were able to connect to the large scattering lengths in the two-nucleon sector and the fact that supernova matter behaves like a resonant Fermi gas at subnuclear densities.

Using the energy-averaged mean-free path against pair absorption as a representative quantity to estimate the astrophysical impact, we found this enhancement of the T-matrix results reduced compared to the relaxation rates at energy transfer $\omega = 0$, but still sizable. At higher densities, T-matrix and chiral N^{3}LO results agree and show a reduction of a factor of two to three compared to OPE results. While these OPE results were used as a proxy for the rates by Hannestad and Raffelt (HR, [51]) currently used in supernova simulations, they differ significantly. We found some likely unphysical behavior in the HR rates at high densities and relatively small temperatures.

In collaboration with astrophysicists, we then investigated the impact of these improved rates on supernovae. We calculated neutrino opacities along radial profiles taken from supernova simulations by generating and employing a big table of the structure factor (or rather $\mathrm{Im}\chi_A$) from which mean-free paths can be calculated through interpolation and integration. The enhancement in going from HR to T-matrix rates happens at densities too low to really impact the explosion dynamics. Only a small shift in neutrinosphere radii was found.

Such a table could also be used directly in a simulation. As this increases the computational cost, we instead used an analytical correction factor for a first estimate of the impact on supernova dynamics. We found our approach to work considerably well around the neutrinosphere. Using a modified instead of the HR interaction rate had only a small impact on the neutrino emission with a $\sim 5\,\%$ shift of luminosities from heavy-lepton to electron neutrinos, somewhat harder neutrino spectra, and slightly delayed cooling of the proto-neutron star.

Three-body forces were shown to give 10—30 % effects in pure neutron matter at saturation density (and somewhat less at N^{3}LO), but much smaller effects in mixtures. We were able to trace this to an approximate cancellation between two-pion-exchange contributions in mixtures. As the c_4 term only contributes in mixtures, this cancellation does not occur in PNM.

In non-degenerate PNM, we derived a structure factor that includes momentum transfer and can thus be used to calculate the combined effect of nuclear recoil and nucleon-nucleon interactions in neutrino-nucleon scattering. The long-wavelength limit (which does not include these finite-$\boldsymbol{q}$ effects) was found to work well when calculating mean-free paths, but not energy transfers. We find a large impact of interactions compared to nucleon recoil especially at high densities and temperatures and at low incoming neutrino energies.

Finally, we studied charged-current reactions, discussed the kinematics, and provided a structure factor expression including partial-wave-expanded expressions for the spin-summed squared matrix elements and the spin relaxation rate. The trends observed in the relaxation rate results are similar to our findings in the neutral-current case, i. e., a reduction of chiral and T-matrix rates at high densities and a resonant enhancement of the T-matrix rate at low densities compared to OPE. However, so far we neither included the effects of chemical potential differences in asymmetric nuclear matter nor differences in the single-particle energy shifts.

Our neutral-current results are based on several approximations in the nucleon-nucleon interaction, conditions, one-body effects, kinematics, and electroweak effects. In order to improve our calculations, we need to go beyond these approximations.

The two most severe approximations in the nucleon-nucleon interaction are the on-shell and Born approximations. Our T-matrix results indicate the need to go beyond the latter also for chiral EFT calculations by including higher-order particle-particle effects. This is important because the T-matrix based on phase shifts is only defined for the on-shell case. One should also further study particle-hole contributions in the degenerate case, which were explored in Ref. [47].

With respect to conditions, the most relevant approximation is that of non-degenerate conditions. However, the basic formalism in Section 4.1 is valid for arbitrary degeneracy. Without assuming degenerate or non-degenerate conditions, the integrals cannot be simplified and calculations are cumbersome, so it might be more promising to interpolate between degenerate and non-degenerate conditions. For the finite-$\boldsymbol{q}$ formalism, mixtures of protons and neutrons should be taken into account.

One-body effects not included in our results are effective masses and the energy shifts ΔU in the charged-current calculations. While they are included in our formalism and straight-forward to implement, these should be calculated consistently with the nucleon-nucleon part of the neutrino-nucleon interactions and the equation of state. Hence, their inclusion will be more elaborate.

In terms of kinematics, our most severe approximation is only used in the finite-$\boldsymbol{q}$ structure factor, where we used a fixed velocity v_{th} instead of a velocity distribution, introducing significant uncertainties at large T. Other kinematic approximations employed are to neglect neutrino momenta in the momentum-conserving delta functions, assume non-relativistic nucleons and neglect momentum transfer for bremsstrahlung processes. We do expect these approximations to work well for low-energy neutrinos.

Furthermore, we neglect certain electroweak effects, most prominently, strangeness contributions to and in-medium modifications of the weak axial coupling g_A. The latter have been discussed in the context of chiral two-body currents in Ref. [67].

The same structure factor that governs neutral-current neutrino reactions could also be used to calculate emissions of axions, hypothetical particles whose emission would be another source of energy-loss for the supernova. Hence, supernova observations can be used to constrain axion properties [46, 173].

With the partial-wave-expanded charged-current matrix elements and spin relaxation rate we have laid the groundwork to calculate charged-current neutrino interaction rates involving interacting nucleons, including the modified Urca process, based on modern nuclear interactions. The impact of differences in the proton and neutron chemical potentials and energy shifts should be studied in detail. Furthermore, it will be interesting to see the effect of chiral and T-matrix interactions on astrophysical quantities and in supernova simulations.

In a broader scope, supernova simulations will improve. $2D$ and $3D$ simulations will become more common, progenitor models will become more advanced. Methods used by different groups will converge and code comparisons will provide insight into discrepancies currently observed between the groups. Limited resolution will remain a problem while the inclusion of advanced nuclear/neutrino physics in the form of huge structure factor tables is a challenge considered much easier to solve [174].

Eventually, neutrinos, light, and gravitational waves from the next galactic supernova will reach our detectors, providing a bulk of data and hopefully many insights into supernova dynamics and neutrino interactions.

A Implementation Details

All numerical results in this thesis not attributed to somebody other than the author have been obtained using a python implementation of the formalism discussed so far. We use `python2.7` and `scipy0.13`.

Interpolations use the `scipy.interpolate.interp1d` function, integrations are done either by a simple implementation of a trapezoidal integration or using `scipy.integrate.quad`. For the trapezoidal integration, a list of x, y pairs is generated (typically, but not necessarily evenly spaced in x) that is then summed over using the trapezoidal rule. For details on the convergence behavior, see Section A.1.

The trapezoidal integration also allows for a straight-forward parallelization using the `python` package `joblib`, which sends the points in the list to multiple cores of the system so they can be computed simultaneously. Since the calculation at one point does not require input from another, no more advanced parallelization method is necessary. `joblib`'s parallelization is also used when evaluating a lot of data points, e. g., along a profile as shown in Chapter 5.

The partial-wave expansion has to be truncated at a given j_{max}. We found $j_{\text{max}} = 6$ to be sufficiently converged at the $\ll 1\,\%$ level.

Wigner $3j$ and $6j$ symbols are evaluated with code based on work by Ulrich Krohn and David Terr [175] and modified to save calculated Wigner symbols during run-time so they only have to be evaluated once per script run. Clebsch-Gordan coefficients are calculated in terms of Wigner $3j$ symbols according to [156]

$$C^{jm}_{j_1 m_1 j_2 m_2} = (-1)^{j_1 - j_2 + m} \sqrt{2j+1} \begin{pmatrix} j_1 & j_2 & j \\ m_1 & m_2 & -m \end{pmatrix} . \tag{A.1}$$

The partial-wave-expanded matrix elements are stored in tables. For each set of potentials, a routine is available that reads in the appropriate values, interpolates the result, corrects for convention differences if necessary, and provides the result to the rest of the program. The OPE matrix elements from Nogga *et al.* (see Appendix B) require a factor $g_A^2/(2F_\pi)^2$ from the OPE potential (3.13) as well as a -3 for $T = 0$. In addition, the factor $(4\pi)^2 i^{l-l'}$ in Eq. (4.35) is not included in their partial wave expansion but in the partial waves themselves, hence we need to divide their results by this factor [155]. The T-matrix expressions in Eqs. (3.15) and (3.16) need to be divided by 4π, the chiral two-body potentials require a factor $\hbar^2/m = 41.44\,\text{MeV}\,\text{fm}^2$ and the three-body potentials need a symmetry factor of $1/3$.

The chiral EFT matrix elements are based on the available NN codes. The T-matrix elements were calculated using phase shifts downloaded from Ref. [131]. In the case of one-pion exchange, an analytical partial-wave-expanded expression is available (Appendix B). However, this expression requires additional sums and integrals to

constant	value
nucleon mass m_N	$939.565\,\text{MeV}$
pion mass m_π	$134.98\,\text{MeV}$
pion decay constant F_π	$92.4\,\text{MeV}$
weak coupling constant g_A	1.26
neutron axial charge C_A^n	$-g_A/2$
proton axial charge C_A^p	$g_A/2$
Fermi's constant G_F	$1.1664 \times 10^{11}\,\text{MeV}^{-2}$
$\hbar c$	$197.327\,\text{MeV}\,\text{fm}$

Table A.1: Constants used in the python implementation.

be performed. Hence, a table was generated based on the analytical expression that could then be interpolated just like the other matrix elements.

For one-pion exchange and leading-order chiral EFT, the spin traces appearing in the derivation of the spin relaxation rate can be calculated analytically. The code based on this approach is typically used for the OPE results in this thesis as no partial-wave expansion is required and therefore the code is much faster.

When evaluating the partial-wave-expanded expression in Eq. (4.50), all calculations except those with three-body potentials (Section 4.5) used $M_T = 0$ for all matrix elements in order to combine nn, np and pp contributions and hence skip two out of three integrations over p, significantly improving the performance of the calculation. For the EM 500 potential, this introduces an error of less than 6 %, and less at the most relevant conditions (cf. Figure 4.13).

Constants used in the code are summarized in Table A.1. As matter is neutron-rich, we use $m_N = m_n$ as well as the mass of the neutral pion $m_\pi = m_{\pi^0}$. We neglect strangeness contributions and in-medium modifications to the axial charges. Furthermore, when calculating leading-order chiral EFT results, we use the LECs from the EM 500 potential, $C_S = -3.90\,\text{fm}^2$ and $C_T = 0.22\,\text{fm}^2$.

The python code suite is available from the author upon request [1].

Some analytical calculations have been performed using `Wolfram Mathematica`. The main ones are the m_{s_i} sums in the partial-wave expansion (Sections 4.1, 7.2), the analytical approximations to the T-matrix rate (Section 4.2.2) and the recoil and collisionless-limit energy transfer expressions (Sections 6.1, 6.2).

A.1 Mean-Free Path Convergence Checks and Quick Integral

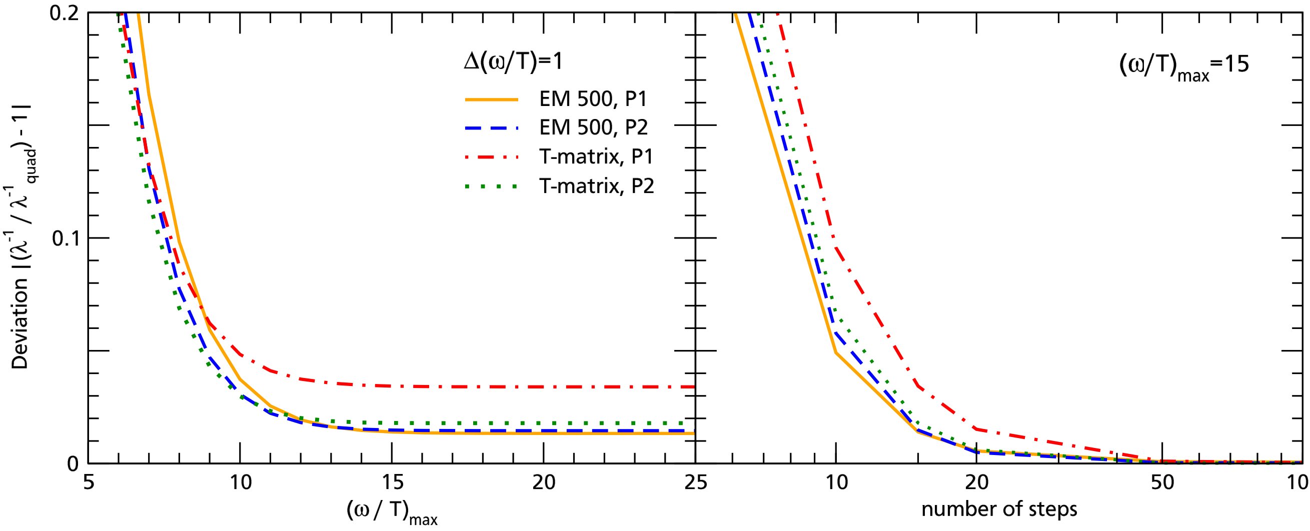

Figure A.1: Convergence of the trapezoidal integral as a function of the upper limit at constant stepsize (left) and as a function of the number of steps at constant upper limit (right). We show the relative deviation from the quadpack results (see text). We use two different potentials and two thermodynamic conditions, $P1 = (\rho = 10^{10}\,\text{g}\,\text{cm}^{-3}, T = 3.16\,\text{MeV}, Y_e = 0.1)$ and $P2 = (\rho = 10^{14}\,\text{g}\,\text{cm}^{-3}, T = 20\,\text{MeV}, Y_e = 0.01)$. Shown are results for the EM 500 potential at $P1$ (orange solid line) and $P2$ (blue dashed line), as well as the T-matrix potential at $P1$ (red dash-dotted line) and $P2$ (green dotted line).

Since mean-free-path calculations add another one or two integrals compared to the calculation of relaxation rates, we use a simple trapezoidal integration method instead of *scipy*'s `integrate.quad()` routine based on Fortran library QUADPACK.

Since we are integrating over ω from 0 to ∞, we need to find the upper limit and maximum step size such that the integral is sufficiently converged. To this end, we plot in Figure A.1 the deviation between the trapezoidal integral

---

[1] `alex@alexanderbartl.de`

and the “exact” quadpack result as a function of the upper limit (left panel) and the number of steps (right panel). With a fixed step size, there is no further improvement beyond $(\frac{\omega}{T})_{\mathrm{max}} = 15$. For this upper limit, the results are already reasonably well converged at a step size $\Delta(\frac{\omega}{T}) = 1$. Deviations are on the sub-percent level for 20 steps except for the T-matrix P1 line, which lies at 1.5 %.

Deviations are at or below the 0.1 % level for 50 steps, but this would mean increasing calculation times by a factor of about 2.5 compared to 20 steps. Since there are several approximations in our formalism which are expected to be of size of a few percent, an upper limit of $(\frac{\omega}{T})_{\mathrm{max}} = 15$ and 20 steps are chosen as a good compromise between calculation time and convergence.

B Simplification of the OPE PWA Matrix Element

An analytical expression of the partial-wave-expanded one-pion-exchange matrix element, or rather the OPE spin-momentum structure, is given in Ref. [172]. This expression involves Wigner $9j$ symbols and other terms that can be analytically simplified as follows:

$$\begin{aligned}
&\left\langle p(lS)Jm_J \left| \frac{\boldsymbol{k}\cdot\boldsymbol{\sigma}_1 \boldsymbol{k}\cdot\boldsymbol{\sigma}_2}{\boldsymbol{k}^2+m_\pi^2} \right| p'(l'S')J'm_J' \right\rangle \\
&\quad = \sum_f \frac{3\hat{f}}{\sqrt{4\pi}} \begin{Bmatrix} 1 & 1 & f \\ 1 & 1 & f \\ 0 & 0 & 0 \end{Bmatrix} C^{f0}_{1010} C^{Jm_J}_{J'm_J'00} \hat{J}' \begin{Bmatrix} J & J' & 0 \\ l & l' & f \\ S & S' & f \end{Bmatrix} \hat{l}\hat{S} \sum_{\lambda_1+\lambda_2=f} \sqrt{\frac{4\pi(2f+1)!}{(2\lambda_1+1)!\,(2\lambda_2+1)!}} \\
&\qquad \times p^{\lambda_1}(-p')^{\lambda_2} \sum_h g_h^f(p,p') \hat{f} \begin{Bmatrix} h & h & 0 \\ \lambda_1 & \lambda_2 & f \\ l & l' & f \end{Bmatrix} \hat{h}^2 \hat{\lambda}_1 \hat{\lambda}_2 C^{l0}_{h0\lambda_1 0} C^{l'0}_{h0\lambda_2 0} (-1)^{l'} \frac{\hat{f}}{\hat{l}} 6 \hat{S}' \hat{f} \begin{Bmatrix} S & S' & f \\ 1/2 & 1/2 & 1 \\ 1/2 & 1/2 & 1 \end{Bmatrix} \qquad \text{(B.1)} \\
&\quad = (-1)^{l'} \hat{S}^2 \hat{J} \delta_{SS'} \delta_{JJ'} \delta_{m_J m_J'}\, 18 \sum_{f=0,2} \hat{f}^4 \begin{Bmatrix} 1 & 1 & f \\ 1 & 1 & f \\ 0 & 0 & 0 \end{Bmatrix} C^{f0}_{1010} \begin{Bmatrix} J & J & 0 \\ l & l' & f \\ S & S & f \end{Bmatrix} \begin{Bmatrix} S & S & f \\ 1/2 & 1/2 & 1 \\ 1/2 & 1/2 & 1 \end{Bmatrix} \\
&\qquad \times \sum_{\lambda_1+\lambda_2=f} \sqrt{\frac{(2f+1)!}{(2\lambda_1+1)!\,(2\lambda_2+1)!}} p^{\lambda_1}(-p')^{\lambda_2} \hat{\lambda}_1 \hat{\lambda}_2 \sum_h g_h^f(p,p') \begin{Bmatrix} h & h & 0 \\ \lambda_1 & \lambda_2 & f \\ l & l' & f \end{Bmatrix} \hat{h}^2 C^{l0}_{h0\lambda_1 0} C^{l'0}_{h0\lambda_2 0} \qquad \text{(B.2)} \\
&\quad = (-1)^{l+J+S} \hat{S}^2 \delta_{SS'} \delta_{JJ'} \delta_{m_J m_J'}\, 6 \sum_{f=0,2} \hat{f} C^{f0}_{1010} \begin{Bmatrix} l' & l & f \\ S & S & J \end{Bmatrix} \sum_{\lambda_1+\lambda_2=f} \hat{\lambda}_1 \hat{\lambda}_2 \sqrt{\frac{(2f+1)!}{(2\lambda_1+1)!\,(2\lambda_2+1)!}} p^{\lambda_1} p'^{\lambda_2} \\
&\qquad \times \sum_h g_h^f(p,p') \hat{h}\, C^{l0}_{h0\lambda_1 0} C^{l'0}_{h0\lambda_2 0} (-1)^h \begin{Bmatrix} \lambda_1 & \lambda_2 & f \\ l' & l & h \end{Bmatrix} \begin{cases} \frac{-1}{18} & \text{if } f=0 \text{ and } S=1\,, \\ \frac{1}{9} & \text{if } f=2 \text{ and } S=1\,, \\ \frac{1}{2\sqrt{3}} & \text{if } f=0 \text{ and } S=0\,, \\ 0 & \text{otherwise}\,. \end{cases} \qquad \text{(B.3)}
\end{aligned}$$

Here we again use the short-hand notation $\hat{a} \equiv \sqrt{2a+1}$ and several properties of the Clebsch-Gordan and Wigner symbols [156]. The function $g_h^f(p,p')$ is given by

$$g_h^f(p,p') = \frac{\hat{h}}{2}(-1)^h 4\pi \int_{-1}^{1} \mathrm{d}\cos\theta\, P_h(\cos\theta) \frac{k^2}{k^2+m_\pi^2} \frac{1}{k^f}\,, \qquad \text{(B.4)}$$

where $k^2 = p^2 + p'^2 - 2pp'\cos\theta$. Equation (B.3) is used in this thesis wherever partial-wave-expanded OPE matrix elements are required.

Bibliography

[1] R. B. Andreo, `http://www.deepskycolors.com/archive/2011/12/08/simeis-147-and-surroundings.html`, retrieved Jun. 22, 2015.

[2] R. Nemiroff and J. Bonnell, APOD 2012/10/09, `http://apod.nasa.gov/apod/ap121009.html`, retrieved Jun. 22, 2015.

[3] D. W. Hamacher, J. Astron. Hist. Herit. **17**, 161 (2014), arXiv:1404.3253.

[4] P. F. Winkler, High. Astron. **14**, 301 (2007).

[5] NASA, ESA and Allison Loll/Jeff Hester (Arizona State University). Acknowledgement: Davide De Martin (ESA/Hubble), `http://www.spacetelescope.org/images/heic0515a/`, retrieved Feb. 16, 2016.

[6] Australian Astronomical Observatory, Photograph by David Malin, `http://203.15.109.22/images/captions/aat050.html`, retrieved Jan. 07, 2016.

[7] ESA/Hubble & NASA, `http://www.spacetelescope.org/images/potw1142a/`, retrieved Feb. 16, 2016.

[8] Kamioka Observatory, ICRR (Institute for Cosmic Ray Research), The University of Tokyo, `http://www-sk.icrr.u-tokyo.ac.jp/sk/gallery/index-e.html`, retrieved Feb. 17, 2016.

[9] R. Davis, Rev. Mod. Phys. **75**, 985 (2003), `www.nobelprize.org/nobel_prizes/physics/laureates/2002/davis-lecture.pdf`.

[10] W. C. Haxton and R. G. H. Robertson, Phys. Rev. C **59**, 515 (1999), arXiv:nucl-th/9806081.

[11] H.-T. Janka, *Supernovae und kosmische Gammablitze: Ursachen und Folgen von Sternexplosionen* (Spektrum Akademischer Verlag, 2011).

[12] A. Burrows, Rev. Mod. Phys. **85**, 245 (2013), arXiv:1210.4921.

[13] K. Sumiyoshi, IAU Symp. **291**, 67 (2013), arXiv:1212.6131.

[14] S. A. Colgate and R. H. White, Astrophys. J. **143**, 626 (1966).

[15] A. B. Balantekin and G. M. Fuller, Prog. Part. Nucl. Phys. **71**, 162 (2013), arXiv:1303.3874.

[16] H. A. Bethe and J. R. Wilson, Astrophys. J. **295**, 14 (1985).

[17] H.-T. Janka, Ann. Rev. Nucl. Part. Sci. **62**, 407 (2012), arXiv:1206.2503.

[18] W. R. Hix *et al.*, Acta Phys. Polon. B **47**, 645 (2016), arXiv:1602.05553.

[19] J. M. Blondin, A. Mezzacappa, and C. DeMarino, Astrophys. J. **584**, 971 (2003), arXiv:astro-ph/0210634.

[20] J. M. Blondin and A. Mezzacappa, Nature **445**, 58 (2007), arXiv:astro-ph/0611680.

[21] M. Liebendörfer, A. Mezzacappa, F.-K. Thielemann, O. E. B. Messer, W. R. Hix, and S. W. Bruenn, Phys. Rev. D **63**, 103004 (2001), arXiv:astro-ph/0006418.

[22] A. Mezzacappa *et al.*, ASP Conf. Ser. **488**, 102 (2014), arXiv:1405.7075.

[23] O. Papish, J. Nordhaus, and N. Soker, Mon. Not. Roy. Astron. Soc. **448**, 2362 (2015), arXiv:1402.4362.

[24] A. Heger, C. L. Fryer, S. E. Woosley, N. Langer, and D. H. Hartmann, Astrophys. J. **591**, 288 (2003), arXiv:astro-ph/0212469.

[25] A. Lohs, G. Martínez-Pinedo, and T. Fischer, PoS NICXIII, 118 (2015).

[26] R. Sharma, S. Bacca, and A. Schwenk, Phys. Rev. C **91**, 042801 (2015), arXiv:1411.3266.

[27] L. Roberts, S. Reddy, and G. Shen, Phys. Rev. C **86**, 065803 (2012), arXiv:1205.4066.

[28] C. J. Horowitz, G. Shen, E. P. O'Connor, and C. D. Ott, Phys. Rev. C **86**, 065806 (2012), arXiv:1209.3173.

[29] G. Martínez-Pinedo, T. Fischer, A. Lohs, and L. Huther, Phys. Rev. Lett. **109**, 251104 (2012), arXiv:1205.2793.

[30] E. Rrapaj, J. W. Holt, A. Bartl, S. Reddy, and A. Schwenk, Phys. Rev. C **91**, 035806 (2015), arXiv:1408.3368.

[31] M. Hempel, Phys. Rev. C **91**, 055807 (2015), arXiv:1410.6337.

[32] G. M. Fuller and B. S. Meyer, Astrophys. J. **376**, 701 (1991).

[33] G. W. Misch, B. A. Brown, and G. M. Fuller, Phys. Rev. C **88**, 015807 (2013), arXiv:1301.7042.

[34] T. Fischer, K. Langanke, and G. Martínez-Pinedo, Phys. Rev. C **88**, 065804 (2013), arXiv:1309.4271.

[35] L. Wolfenstein, Phys. Rev. D **17**, 2369 (1978).

[36] S. P. Mikheev and A. Y. Smirnov, Yad. Fiz **42**, 1441; Sov. J. Nucl. Phys. **42**, 913 (1985).

[37] H. Duan, G. M. Fuller, J. Carlson, and Y.-Z. Qian, Phys. Rev. D **75**, 125005 (2007), arXiv:astro-ph/0703776.

[38] H. Duan, G. M. Fuller, and Y.-Z. Qian, Ann. Rev. Nucl. Part. Sci. **60**, 569 (2010), arXiv:1001.2799.

[39] J. F. Cherry, J. Carlson, A. Friedland, G. M. Fuller, and A. Vlasenko, Phys. Rev. Lett. **108**, 261104 (2012), arXiv:1203.1607.

[40] R. F. Sawyer, Phys. Rev. Lett. **116**, 081101 (2016), arXiv:1509.03323.

[41] C. Volpe, J. Phys. Conf. Ser. **631**, 012048 (2015), arXiv:1503.01355.

[42] E. J. Lentz, A. Mezzacappa, O. E. Bronson Messer, W. R. Hix, and S. W. Bruenn, Astrophys. J. **760**, 94 (2012), arXiv:1206.1086.

[43] B. Müller, H.-T. Janka, and A. Marek, Astrophys. J. **756**, 84 (2012), arXiv:1202.0815.

[44] S. W. Bruenn *et al.*, Astrophys. J. **818**, 123 (2016), arXiv:1409.5779.

[45] T. Melson, H.-T. Janka, R. Bollig, F. Hanke, A. Marek, and B. Müller, Astrophys. J. **808**, L42 (2015), arXiv:1504.07631.

[46] G. G. Raffelt, *Stars as laboratories for fundamental physics: the astrophysics of neutrinos, axions, and other weakly interacting particles* (The University of Chicago Press, 1996), `http://wwwth.mpp.mpg.de/members/raffelt/mypapers/199613.pdf`.

[47] G. I. Lykasov, C. J. Pethick, and A. Schwenk, Phys. Rev. C **78**, 045803 (2008), arXiv:0808.0330.

[48] S. Reddy, M. Prakash, and J. M. Lattimer, Phys. Rev. D **58**, 013009 (1998), arXiv:astro-ph/9710115.

[49] C. J. Horowitz, Phys. Rev. D **65**, 043001 (2002), arXiv:astro-ph/0109209.

[50] B. Friman and O. Maxwell, Astrophys. J. **232**, 541 (1979).

[51] S. Hannestad and G. Raffelt, Astrophys. J. **507**, 339 (1998), arXiv:astro-ph/9711132.

[52] B. Müller and H.-T. Janka, Astrophys. J. **788**, 82 (2014), arXiv:1402.3415.

[53] A. Mirizzi, I. Tamborra, H.-T. Janka, N. Saviano, K. Scholberg, R. Bollig, L. Hüdepohl, and S. Chakraborty, Riv. Nuovo Cim. **39**, 1 (2016), arXiv:1508.00785.

[54] K. G. Balasi, K. Langanke, and G. Martínez-Pinedo, Prog. Part. Nucl. Phys. **85**, 33 (2015), arXiv:1503.08095.

[55] J. M. Lattimer and F. D. Swesty, Nucl. Phys. A **535**, 331 (1991).

[56] H. Shen, H. Toki, K. Oyamatsu, and K. Sumiyoshi, Prog. Theor. Phys. **100**, 1013 (1998), arXiv:nucl-th/9806095.

[57] S. Bacca, K. Hally, M. Liebendörfer, A. Perego, C. J. Pethick, and A. Schwenk, Astrophys. J. **758**, 34 (2012), arXiv:1112.5185.

[58] Y. Z. Qian and S. E. Woosley, Astrophys. J. **471**, 331 (1996), arXiv:astro-ph/9611094.

[59] A. Arcones and F.-K. Thielemann, J. Phys. G **40**, 013201 (2013), arXiv:1207.2527.

[60] C. Fröhlich, J. Phys. G **41**, 044003 (2014).

[61] C. Fröhlich, G. Martínez-Pinedo, M. Liebendörfer, F.-K. Thielemann, E. Bravo, W. R. Hix, K. Langanke, and N. T. Zinner, Phys. Rev. Lett. **96**, 142502 (2006), arXiv:astro-ph/0511376.

[62] T. Melson, H.-T. Janka, and A. Marek, Astrophys. J. **801**, L24 (2015), arXiv:1501.01961.

[63] A. Mezzacappa *et al.*, PoS LATTICE2014, 010 (2015), arXiv:1501.01688.

[64] H.-T. Janka, T. Melson, and A. Summa, arXiv e-prints (2016), arXiv:1602.05576.

[65] E. P. O'Connor and S. M. Couch, arXiv e-prints (2015), arXiv:1511.07443.

[66] M. A. Skinner, A. Burrows, and J. C. Dolence, arXiv e-prints (2015), arXiv:1512.00113.

[67] A. Bartl, Neutrino interactions with dense nuclear matter based on chiral effective field theory, Master's thesis, TU Darmstadt, 2013.

[68] LHCb Collaboration, R. Aaij *et al.*, Phys. Rev. Lett. **115**, 072001 (2015), arXiv:1507.03414.

[69] A. Esposito, A. L. Guerrieri, F. Piccinini, A. Pilloni, and A. D. Polosa, Int. J. Mod. Phys. A **30**, 1530002 (2015), arXiv:1411.5997.

[70] Particle Data Group, K. A. Olive *et al.*, Chin. Phys. C **38**, 090001 (2014), and 2015 update.

[71] S. Bethke, Prog. Part. Nucl. Phys. **58**, 351 (2007), arXiv:hep-ex/0606035.

[72] S. R. Beane, W. Detmold, K. Orginos, and M. J. Savage, Prog. Part. Nucl. Phys. **66**, 1 (2011), arXiv:1004.2935.

[73] NPLQCD Collaboration, S. R. Beane *et al.*, Phys. Rev. D **87**, 034506 (2013), arXiv:1206.5219.

[74] M. J. Savage, Nuclear Physics from Lattice Quantum Chromodynamics, in *12th Conference on the Intersections of Particle and Nuclear Physics (CIPANP 2015) Vail, Colorado, USA, May 19-24, 2015*, arXiv:1510.01787.

[75] R. B. Wiringa, V. G. J. Stoks, and R. Schiavilla, Phys. Rev. C **51**, 38 (1995), arXiv:nucl-th/9408016.

[76] R. Machleidt, Phys. Rev. C **63**, 024001 (2001), arXiv:nucl-th/0006014.

[77] A. Arcones and G. Martínez-Pinedo, Phys. Rev. C **83**, 045809 (2011), arXiv:1008.3890.

[78] D. Martin, A. Arcones, W. Nazarewicz, and E. Olsen, Phys. Rev. Lett. **116**, 121101 (2016), arXiv:1512.03158.

[79] D. B. Kaplan, Five lectures on effective field theory, 2005, arXiv:nucl-th/0510023.

[80] J. Goldstone, A. Salam, and S. Weinberg, Phys. Rev. **127**, 965 (1962).

[81] S. Weinberg, Phys. Lett. B **251**, 288 (1990).

[82] S. Weinberg, Nucl. Phys. B **363**, 3 (1991).

[83] A. H. Guth, K. Huang, and R. L. Jaffe, editors, *Asymptotic Realms Of Physics. Essays In Honor Of Francis E. Low*, MIT Press, Cambridge, MA, 1983.

[84] E. Epelbaum, Prog. Part. Nucl. Phys. **57**, 654 (2006), arXiv:nucl-th/0509032.

[85] E. Epelbaum, Nuclear forces from chiral effective field theory: a primer, lecture notes, 2010, arXiv:1001.3229.

[86] U. van Kolck, Phys. Rev. C **49**, 2932 (1994).

[87] T. Otsuka, T. Suzuki, J. D. Holt, A. Schwenk, and Y. Akaishi, Phys. Rev. Lett. **105**, 032501 (2010), arXiv:0908.2607.

[88] K. Hebeler, S. K. Bogner, R. J. Furnstahl, A. Nogga, and A. Schwenk, Phys. Rev. C **83**, 031301 (2011), arXiv:1012.3381.

[89] J. D. Holt, T. Otsuka, A. Schwenk, and T. Suzuki, J. Phys. G **39**, 085111 (2012), arXiv:1009.5984.

[90] R. Roth, S. Binder, K. Vobig, A. Calci, J. Langhammer, and P. Navrátil, Phys. Rev. Lett. **109**, 052501 (2012), arXiv:1112.0287.

[91] G. Hagen, M. Hjorth-Jensen, G. Jansen, R. Machleidt, and T. Papenbrock, Phys. Rev. Lett. **108**, 242501 (2012), arXiv:1202.2839.

[92] A. Gallant *et al.*, Phys. Rev. Lett. **109**, 032506 (2012), arXiv:1204.1987.

[93] S. Binder, J. Langhammer, A. Calci, P. Navrátil, and R. Roth, Phys. Rev. C **87**, 021303 (2013), arXiv:1211.4748.

[94] H. Hergert, S. K. Bogner, S. Binder, A. Calci, J. Langhammer, R. Roth, and A. Schwenk, Phys. Rev. C **87**, 034307 (2013), arXiv:1212.1190.

[95] K. Hebeler, J. D. Holt, J. Menéndez, and A. Schwenk, Ann. Rev. Nucl. Part. Sci. **65**, 457 (2015), arXiv:1508.06893.

[96] S. Binder, J. Langhammer, A. Calci, and R. Roth, Phys. Lett. B **736**, 119 (2014), arXiv:1312.5685.

[97] K. Hebeler, J. M. Lattimer, C. J. Pethick, and A. Schwenk, Phys. Rev. Lett. **105**, 161102 (2010), arXiv:1007.1746.

[98] M. B. Tsang *et al.*, Phys. Rev. C **86**, 015803 (2012), arXiv:1204.0466.

[99] K. Hebeler, J. M. Lattimer, C. J. Pethick, and A. Schwenk, Astrophys. J. **773**, 11 (2013), arXiv:1303.4662.

[100] T. Krüger, I. Tews, K. Hebeler, and A. Schwenk, Phys. Rev. C **88**, 025802 (2013), arXiv:1304.2212.

[101] A. Carbone, A. Rios, and A. Polls, Phys. Rev. C **90**, 054322 (2014), arXiv:1408.0717.

[102] C. Drischler, K. Hebeler, and A. Schwenk, Phys. Rev. C **93**, 054314 (2016), arXiv:1510.06728.

[103] J. Menéndez, D. Gazit, and A. Schwenk, Phys. Rev. D **86**, 103511 (2012), arXiv:1208.1094.

[104] P. Klos, J. Menéndez, D. Gazit, and A. Schwenk, Phys. Rev. D **88**, 083516 (2013), arXiv:1304.7684, [Erratum: Phys. Rev. D **89**, 029901 (2014)].

[105] L. Vietze, P. Klos, J. Menéndez, W. C. Haxton, and A. Schwenk, Phys. Rev. D **91**, 043520 (2015), arXiv:1412.6091.

[106] G. Hagen *et al.*, Nature Phys. **12**, 186 (2015), arXiv:1509.07169.

[107] P. Klos, J. E. Lynn, I. Tews, S. Gandolfi, A. Gezerlis, H.-W. Hammer, M. Hoferichter, and A. Schwenk, arXiv e-prints (2016), arXiv:1604.01387.

[108] D. R. Entem and R. Machleidt, Phys. Rev. C **68**, 041001 (2003), arXiv:nucl-th/0304018.

[109] I. Tews, T. Krüger, K. Hebeler, and A. Schwenk, Phys. Rev. Lett. **110**, 032504 (2013), arXiv:1206.0025.

[110] K. Hebeler, H. Krebs, E. Epelbaum, J. Golak, and R. Skibinski, Phys. Rev. C **91**, 044001 (2015), arXiv:1502.02977.

[111] H. Krebs, A. Gasparyan, and E. Epelbaum, Phys. Rev. C **85**, 054006 (2012), arXiv:1203.0067.

[112] H. Krebs, A. Gasparyan, and E. Epelbaum, Phys. Rev. C **87**, 054007 (2013), arXiv:1302.2872.

[113] D. R. Entem, N. Kaiser, R. Machleidt, and Y. Nosyk, Phys. Rev. C **91**, 014002 (2015), arXiv:1411.5335.

[114] D. R. Entem, N. Kaiser, R. Machleidt, and Y. Nosyk, Phys. Rev. C **92**, 064001 (2015), arXiv:1505.03562.

[115] E. Epelbaum, H. Krebs, and U.-G. Meißner, Phys. Rev. Lett. **115**, 122301 (2015), arXiv:1412.4623.

[116] E. Epelbaum, H. Krebs, and U.-G. Meißner, Eur. Phys. J. A **51**, 53 (2015), arXiv:1412.0142.

[117] A. Gezerlis, I. Tews, E. Epelbaum, S. Gandolfi, K. Hebeler, A. Nogga, and A. Schwenk, Phys. Rev. Lett. **111**, 032501 (2013), arXiv:1303.6243.

[118] I. Tews, Quantum Monte Carlo calculations with chiral effective field theory interactions, Ph. D. thesis, TU Darmstadt, 2015, `http://tuprints.ulb.tu-darmstadt.de/5011/`.

[119] I. Tews, S. Gandolfi, A. Gezerlis, and A. Schwenk, Phys. Rev. C **93**, 024305 (2016), arXiv:1507.05561.

[120] J. E. Lynn, I. Tews, J. Carlson, S. Gandolfi, A. Gezerlis, K. E. Schmidt, and A. Schwenk, Phys. Rev. Lett. **116**, 062501 (2016), arXiv:1509.03470.

[121] A. Ekström *et al.*, Phys. Rev. Lett. **110**, 192502 (2013), arXiv:1303.4674.

[122] A. Ekström *et al.*, Phys. Rev. C **91**, 051301 (2015), arXiv:1502.04682.

[123] A. Ekström, B. D. Carlsson, K. A. Wendt, C. Forssén, M. Hjorth-Jensen, R. Machleidt, and S. M. Wild, J. Phys. G **42**, 034003 (2015), arXiv:1406.6895.

[124] R. J. Furnstahl, D. R. Phillips, and S. Wesolowski, J. Phys. G **42**, 034028 (2015), arXiv:1407.0657.

[125] R. J. Furnstahl, N. Klco, D. R. Phillips, and S. Wesolowski, Phys. Rev. C **92**, 024005 (2015), arXiv:1506.01343.

[126] B. D. Carlsson *et al.*, Phys. Rev. X **6**, 011019 (2016), arXiv:1506.02466.

[127] E. Epelbaum, H.-W. Hammer, and U.-G. Meissner, Rev. Mod. Phys. **81**, 1773 (2009), arXiv:0811.1338.

[128] R. Machleidt and D. R. Entem, Phys. Rep. **503**, 1 (2011), arXiv:1105.2919.

[129] E. Epelbaum, PoS ConfinementX, 014 (2012), arXiv:1302.3241.

[130] E. Epelbaum, Nuclear Chiral EFT in the Precision Era, in *8th International Workshop on Chiral Dynamics (CD 2015) Pisa, Italy, June 29-July 3, 2015*, arXiv:1510.07036.

[131] V. G. J. Stoks, R. A. M. Klomp, M. C. M. Rentmeester, and J. J. de Swart, Phys. Rev. C **48**, 792 (1993), `www.nn-online.org`.

[132] R. J. Furnstahl, Nucl. Phys. Proc. Suppl. **228**, 139 (2012), arXiv:1203.1779.

[133] S. K. Bogner, R. J. Furnstahl, and A. Schwenk, Prog. Part. Nucl. Phys. **65**, 94 (2010), arXiv:0912.3688.

[134] F. Wegner, Annalen Phys. **506**, 77 (1994).

[135] F. Wegner, Nucl. Phys. Proc. Suppl. **90**, 141 (2000).

[136] F. Wegner, J. Phys. A **39**, 8221 (2006), arXiv:cond-mat/0511660.

[137] S. D. Glazek and K. G. Wilson, Phys. Rev. D **48**, 5863 (1993).

[138] R. Roth, S. Binder, K. Vobig, A. Calci, J. Langhammer, and P. Navrátil, Phys. Rev. Lett. **109**, 052501 (2012), arXiv:1112.0287.

[139] J. W. Holt, N. Kaiser, and W. Weise, Phys. Rev. C **81**, 024002 (2010), arXiv:0910.1249.

[140] K. Hebeler and A. Schwenk, Phys. Rev. C **82**, 014314 (2010), arXiv:0911.0483.

[141] B. Friman and A. Schwenk, Three-body interactions in Fermi systems, in *From Nuclei to Stars: Festschrift in Honor of Gerald E. Brown*, edited by S. Lee, World Scientific, 2011, arXiv:1101.4858.

[142] A. Dyhdalo, R. J. Furnstahl, K. Hebeler, and I. Tews, Phys. Rev. C **94**, 034001 (2016), arXiv:1602.08038.

[143] K. Tsukiyama, S. K. Bogner, and A. Schwenk, Phys. Rev. Lett. **106**, 222502 (2011), arXiv:1006.3639.

[144] H. Hergert, S. K. Bogner, T. D. Morris, A. Schwenk, and K. Tsukiyama, Phys. Rept. **621**, 165 (2016), arXiv:1512.06956.

[145] R. Buras, M. Rampp, H.-T. Janka, and K. Kifonidis, Astron. Astrophys. **447**, 1049 (2006), arXiv:astro-ph/0507135.

[146] C. Hanhart, D. R. Phillips, and S. Reddy, Phys. Lett. B **499**, 9 (2001), arXiv:astro-ph/0003445.

[147] A. Schwenk, P. Jaikumar, and C. Gale, Phys. Lett. B **584**, 241 (2004), arXiv:nucl-th/0309072.

[148] S. Bacca, K. Hally, C. J. Pethick, and A. Schwenk, Phys. Rev. C **80**, 032802 (2009), arXiv:0812.0102.

[149] A. Bartl, C. J. Pethick, and A. Schwenk, Phys. Rev. Lett. **113**, 081101 (2014), arXiv:1403.4114.

[150] G. Sigl, Phys. Rev. D **56**, 3179 (1997), arXiv:astro-ph/9703056.

[151] T. A. Thompson, A. Burrows, and J. E. Horvath, Phys. Rev. C **62**, 035802 (2000), arXiv:astro-ph/0003054.

[152] N. Iwamoto and C. J. Pethick, Phys. Rev. D **25**, 313 (1982).

[153] A. Burrows and R. F. Sawyer, Phys. Rev. C **58**, 554 (1998), arXiv:astro-ph/9801082.

[154] D. Yakovlev, A. Kaminker, O. Y. Gnedin, and P. Haensel, Phys. Rep. **354**, 1 (2001), arXiv:astro-ph/0012122.

[155] K. A. D. Hally, The production of μ and τ neutrinos in core-collapse supernovae, Bachelor's thesis, Acadia University, 2009.

[156] D. A. Varshalovich, A. N. Moskalev, and V. K. Khersonskii, *Quantum Theory of Angular Momentum* (World Scientific Publishing, 1988).

[157] J. Menéndez, D. Gazit, and A. Schwenk, Phys. Rev. Lett. **107**, 062501 (2011), arXiv:1103.3622.

[158] E. Epelbaum, W. Glöckle, and U.-G. Meißner, Nucl. Phys. A **747**, 362 (2005), arXiv:nucl-th/0405048.

[159] C. J. Horowitz and A. Schwenk, Nucl. Phys. A **776**, 55 (2006), arXiv:nucl-th/0507033.

[160] M. C. M. Rentmeester, R. G. E. Timmermans, and J. J. de Swart, Phys. Rev. C **67**, 044001 (2003), arXiv:nucl-th/0302080.

[161] A. Perego, M. Hempel, C. Fröhlich, K. Ebinger, M. Eichler, J. Casanova, M. Liebendörfer, and F.-K. Thielemann, Astrophys. J. **806**, 275 (2015), arXiv:1501.02845.

[162] A. Arcones, H.-T. Janka, and L. Scheck, Astron. Astrophys. **467**, 1227 (2007), arXiv:astro-ph/0612582.

[163] H. Yasin, Impact of bremsstrahlung on the neutrinosphere for muon and tau neutrinos, Master's proposal, TU Darmstadt, 2014.

[164] A. Bartl, R. Bollig, H.-T. Janka, and A. Schwenk, Phys. Rev. D **94**, 083009 (2016), arXiv:1608.05037.

[165] M. Rampp and H.-T. Janka, Astron. Astrophys. **396**, 361 (2002), arXiv:astro-ph/0203101.

[166] S. Woosley, A. Heger, and T. Weaver, Rev. Mod. Phys. **74**, 1015 (2002).

[167] A. W. Steiner, M. Hempel, and T. Fischer, Astrophys. J. **774**, 17 (2013), arXiv:1207.2184.

[168] A. Bartl, M. Voskresenskaya, C. J. Pethick, and A. Schwenk, in preparation, 2016.

[169] D. L. Tubbs, Astrophys. J. **231**, 846 (1979).

[170] D. L. Tubbs and D. N. Schramm, Astrophys. J. **201**, 467 (1975).

[171] A. Schwenk, private communication.

[172] A. Nogga, R. G. E. Timmermans, and U. v. Kolck, Phys. Rev. C **72**, 054006 (2005), arXiv:nucl-th/0506005.

[173] T. Fischer, S. Chakraborty, M. Giannotti, A. Mirizzi, A. Payez, and A. Ringwald, Phys. Rev. D **94**, 085012 (2016), arXiv:1605.08780.

[174] Consensus in the final discussion, Workshop on Microphysics In Computational Relativistic Astrophysics (MICRA) 2015, Stockholm, Sweden.

[175] U. Krohn, `http://massey.dur.ac.uk/umk/files/python/wigner.py`, retrieved Jan. 16, 2012.

Acknowledgment

First of all, I would like to thank my advisor Achim Schwenk for this very interesting research topic, the chance to work in his group, his continued support over the years, and the helpful hints he provided at various stages. I am grateful for the chance to participate in multiple workshops and conferences and attend two TALENT summer schools where I could deepen my knowledge of nuclear physics and astrophysics.

A big thank-you goes to all the current and former members of the STRONGINT group, especially Achim Schwenk, Alexandros Gezerlis, Arianna Carbone, Christian Drischler, Ingo Tews, Jason D. Holt, Javier Menéndez, Joel Lynn, Johannes Simonis, Kai Hebeler, Kyle Wendt, Laura Vietze, Liliana Caballero, Lukas Huth, Maria Voskresenskaya, Martin Hoferichter, Philipp Klos, Svenja Greif, Thomas Krüger, Toño Coello Pérez, Victoria Durant, and Vittorio Somà. Thank you for a great time at the institute, for interesting discussions over lunch and some very enjoyable evening and weekend events. Working at the institute would be much less fun without nice colleagues.

Special thanks goes to Christopher Pethick and Maria Voskresenskaya for our collaboration on neutral-current structure factors and reactions and to Christian Drischler and Kai Hebeler for providing the normal-ordered potentials to evaluate the impact of three-body forces and the helpful discussion of the results.

The main motivation for this thesis stems from its application in supernova simulations. Therefore, I would like to thank Hannah Yasin from TU Darmstadt as well as Robert Bollig and Thomas Janka from the Max Planck Institute for Astrophysics in Garching for the fruitful collaboration. I would also like to acknowledge helpful discussions with Albino Perego, Almudena Arcones, Ermal Rrapaj, and Sanjay Reddy.

I thank Achim Schwenk, Almudena Arcones, Christian Drischler, Hannah Yasin, Ingo Tews, Katja Miller, Marie-Luise Braatz, and Thomas Krüger for (partially) proof-reading the draft of this thesis and providing helpful comments.

I am very glad for the support of family and friends throughout my studies and the doctoral phase, a constant source of joy and motivation, and a welcome distraction from time to time.

Furthermore, I am very grateful to the Studienstiftung des deutschen Volkes (the German Academic Scholarship Foundation) for not only financially supporting this doctoral project but also for a lot of interesting seminars, workshops and excursions. I have learned a lot, travelled a lot, discussed a lot and met some great people that I can now call friends.

Additional financial support came from the Minerva Stiftung through the ARCHES award and in final stages from the Deutsche Forschungsgemeinschaft (DFG) through grant SFB 1245.

Finally, a tip of the hat goes to the developers of all the free and/or open-source tools that helped me do my research and write this thesis. Among many others, I would like to mention Python and the scipy package, Wolfram Alpha, Kubuntu, KDE and the many large and small but very helpful tools it ships with, gnuplot, Inkscape, LaTeX and the tud-design packages, detexify, and various plugins for the Sublime Text editor. A special tip of the hat goes to the communities at Stack Exchange for being a great solution resource on programming, system administration and LaTeX issues.

Curriculum Vitae

Alexander Bartl

July 19th, 1987	Born in Offenbach am Main, Germany
June 16th, 2007	Abitur, Goetheschule Neu-Isenburg, Germany
2008 – 2011	Bachelor studies, TU Darmstadt, Germany
2009 – 2010	Two terms abroad, University of Saskatchewan, Saskatoon SK, Canada
March 23rd, 2011	Bachelor's degree, thesis title: "An Interacting Boson Model including Giant Quadrupole Resonance"
2011 – 2013	Master studies, TU Darmstadt, Germany
January 31st, 2013	Master's degree, thesis title: "Neutrino interactions with dense nuclear matter based on chiral effective field theory"
2013 – 2016	Doctoral studies and member of the scientific staff, TU Darmstadt, Germany

Erklärung zur Dissertation

Hiermit versichere ich, die vorliegende Dissertation ohne Hilfe Dritter nur mit den angegebenen Quellen und Hilfsmitteln angefertigt zu haben. Alle Stellen, die aus Quellen entnommen wurden, sind als solche kenntlich gemacht. Diese Arbeit hat in gleicher oder ähnlicher Form noch keiner Prüfungsbehörde vorgelegen. Eine Promotion wurde bisher noch nicht versucht.

Darmstadt, den 31. Oktober 2016

(Alexander Bartl)